Assembly and Organization of Structurally Novel Amphiphilic Molecules at Air-Water and Air-Solid Interfaces

by

Bharat Kumar

Thesis submitted to the

Jawaharlal Nehru University

for the award of the degree of
Doctor of Philosophy

2009

Raman Research Institute

Bangalore 560 080
India

CERTIFICATE

This is to certify that the thesis entitled **"Assembly and Organization of Structurally Novel Amphiphilic Molecules at Air-Water and Air-Solid Interfaces"** submitted by Bharat Kumar for the award of the degree of DOCTOR OF PHILOSOPHY of Jawaharlal Nehru University is his original work. This has not been published or submitted to any other University for the award of any other degree or diploma.

Prof. Ravi Subrahmanyan
(Center Chairperson)
Director
Raman Research Institute
Bangalore 560 080 INDIA

Prof. Kattera A. Suresh
(Thesis Supervisor)

DECLARATION

I hereby declare that this thesis is composed independently by me at the Raman Research Institute, Bangalore, under the supervision of Prof. Kattera A. Suresh. The subject matter presented in this thesis has not previously formed the basis for the award of any degree, diploma, membership, associateship, fellowship or any other similar title of any University or Institution.

(Prof. Kattera A. Suresh) (Bharat Kumar)

Raman Research Institute
Bangalore 560 080 - INDIA

Acknowledgements

I am deeply indebted to my supervisor Prof. Kattera A. Suresh for his invaluable guidance, support, encouragement and help. I thank him for everything that I learnt from him. It has been a pleasure for me to work with him.

I am extremely thankful to Prof. V. Lakshminarayanan for his constant interest in my work and helpful discussions.

I am grateful to Prof. Sandeep Kumar for providing some very interesting and novel molecules. I would also like to thank him for helpful discussions. I also thank members of his group, Hari Krishna Bisoyi and Satyam Kumar Gupta for synthesizing the materials that I have used and for friendly interactions. I thank Dr. A. K. Prajapati for providing the azobenzene material and for useful discussions with him during his stay in RRI.

I would like to thank Prof. N. Kumar, former Director, for his encouragement and keen interest in my work. I would also like to thank Prof. Ravi Subrahmanyan, the present Director, for his encouragement and help.

I thank Prof. G. S. Ranganath for many useful discussions and enlightening remarks. I also thank Prof. Ruckmongathan, Dr. V. A. Raghunathan, Dr. R. Pratibha, Dr. Arun Roy, Dr. Y. Hatwalne, Dr. N. Andal, Dr. Abhishek Dhar and Dr. P. Pramod for helpful discussions.

I thank Dr. Y. M. Patil for his support and help in library related matters. My thanks are due to the highly efficient and helpful library staff of RRI. The excellent book collections and its proper maintenance deserves a special mention. I acknowledge the staff at the computer section, Mr. Jacob Rajan, Mr. Nandakumar, Mr. Krishnamurthy and Mr. Sridhar for their help related to computers.

It is a pleasure to thank Mr. M. Mani of SCM workshop and Mr. A. Dhason. Their expertise and fine skills were useful in designing and building some of the components required for my experiments. Special thanks to Mr. Ram for gold coating, Mrs. Vasudha for material analysis and Mr. K. Radhakrishna for his help in the office matters. I thank Shashidhara, Gopalakrishna and Somashekar for various help in electronics and interfacing of some

instruments in my experiments.

I would like to thank Ms. I. Kavya Uthaiah who was very helpful in AFM experiments.

I thank Shri K. Krishnamaraju for his many helpful suggestions on administrative matter and timely help at various occasions. I would like to express my sincere thanks to efficient and friendly administrative, accounts and purchase staff of RRI. I am thankful to canteen staff and hostel cooks who cheerfully provided hygienic food.

My thanks to Viswanath, Raj Kumar, Amit and Alpana for providing friendly environment in the laboratory and their cooperation and help in various ways. I enjoyed every moment with my friends Bibhu, Suresh, Hari, Radhakrishnan, Rakesh and Nagu. I also thank Srikanth, Arun, Anija, Brindaban, Sandeep, Tripta, Satyam, Sajal, Jayakumar, Radhika, Santanu, Sanat, Madhu, Kanhaiya, Mamta and Santosh for making my stay in RRI memorable.

My sincere thanks to Hari and Suresh for patiently going through the thesis chapters and for their suggestions.

My heartfelt thanks to Dr. S. M. Khenned who encouraged and motivated me to take research career. I would also like to thank my friend Guru for his help, constant support and many academic and non-academic discussions. I thank all my friends and relatives for their support.

My sincere thanks to my parents, Vinaya moushi, Indu moushi and Ravi mama, who have been encouraging throughout my career.

I dedicate this work to Amma and Vinaya moushi to honor their love, patience and support.

Many thanks to my sisters Aru and Ashu, and my fiancee Sushma for their support.

Finally, I would like to thank Indian taxpayers and Government of India for financial support.

Contents

List of symbols used in the thesis

π	Surface pressure
π_c	Collapse pressure
A_m	Area per molecule
$A_\circ$	Limiting area per molecule
$\gamma_\circ$	Surface tension of pure water
γ	Surface tension of water with monolayer
$\|E\|$	Compressional modulus of monolayer
π_{tr}	Partial surface pressure of *trans* monolayer
π_c	Partial surface pressure of *cis* monolayer
π°_{tr}	Surface pressure of pure *trans* monolayer
π°_c	Surface pressure of pure *cis* monolayer
k_{col}	Rate constant for thermal isomerization of *cis* isomer
k	Rate constant for photoisomerization reaction of *trans* isomer
A_i	Initial molecular area
α_t	Monolayer strain rate
n	Power law index
ε	Activation energy
k_b	Boltzmann's constant
ϕ_b	Contact barrier height
e	Charge of eletron
m_e	Mass of free electron
m^*	Effective mass of electron
h	Planck's constant
$\overline{\phi}$	Mean barrier height for metal-film-metal junction
$\overline{d}$	Mean barrier width
$\phi_\circ$	Barrier height
d	Distance between electrodes

List of abbreviations used in the thesis

12D1H	H-shaped azobenzene dimer
trans-12D1H	12D1H molecule in *trans* state
cis-12D1H	12D1H molecule in *cis* state
tp-dimer	Dimer of triphenylene moiety
AQD6	Hexatriphenylene substituted anthraquinone
Trp	Triphenylene polymer
Aqp	Anthraquinone polymer
HMDS	Hexamethyldisilazane
LB	Langmuir-Blodgett
ESP	Equilibrium surface pressure
BAM	Brewster angle microscope
AFM	Atomic force microscope
CSAFM	current sensing atomic force microscope
STM	Scanning tunneling microscope
$I-V$	Current−Voltage characteristics
HOMO	Highest occupied molecular orbital
LUMO	Lowest unoccupied molecular orbital
V_{trans}^{+}	Transition voltage for positive bias
V_{trans}^{-}	Transition voltage for negative bias
FN	Fowler-Nordheim

Preface

This thesis deals with the studies on assembly and organization of novel amphiphilic molecules at air-water and air-solid interfaces. Molecules consisting of hydrophilic and hydrophobic parts are known as amphiphilic molecules or amphiphiles. These molecules when spread at air-water interface, the hydrophilic part anchors to the water and the hydrophobic part stays away from the water. If there is a proper balance between the hydrophilic and hydrophobic parts, these molecules form insoluble monolayer at air-water interface called Langmuir monolayer.

Langmuir monolayer can be used as a model system to study the properties of two-dimensional systems [1]. In addition, useful information about molecular sizes and intermolecular forces can be obtained from the studies on monolayers at air-water interface. Langmuir monolayers can also be used as model biological membranes and studies on the monolayers of biological molecules will help in understanding the functionality of the biological systems [2].

In analogous to the phases exhibited by the matter in bulk, Langmuir monolayers exhibit two-dimensional phases depending on the thermodynamic conditions [3]. Various phases in the Langmuir monolayers have been reported and the richness in the phase diagram is of scientific interest. Various experimental, theoretical and simulation techniques have been used to study the phases exhibited by the Langmuir monolayer. Usually, the sequence in which the monolayer exhibits the phases is, gas (G), low density liquid (L_1), high density liquid (L_2) and solid (S) phases.

The phase transitions in the Langmuir monolayer can be brought out by changing the thermodynamic parameters like surface density of amphiphilic molecules, temperature and surface pressure (π). The surface pressure of the monolayer is given by,

$$\pi = \gamma_\circ - \gamma \tag{1}$$

Here, $\gamma_\circ$ is the surface tension of pure water and γ is the surface tension of the water with monolayer. As we increase the surface density of the molecules in the monolayer, the area per molecule (A_m) decreases and the surface pressure increases. The variation of π as a function of A_m depends on the phases exhibited by the monolayer. Thus, we can get the valuable information on the phase transition in the monolayers by plotting the $\pi - A_m$ data obtained at a constant temperature. This technique is known as surface manometry and the variation of π as a function of A_m is known as $\pi - A_m$ isotherm. A kink in the isotherm signifies a phase transition and the plateau in the isotherm indicates the coexistence of phases. The phases exhibited by the monolayer can be seen by Brewster angle microscopy (BAM).

Langmuir monolayers can be transferred from the air-water interface onto the solid substrates by Langmuir-Blodgett (LB) technique to obtain LB films. These films can be studied using techniques like atomic force microscope (AFM). Different modes of AFM can be used to study the topography, electrical and mechanical properties of the LB films.

This thesis describes our studies on the formation and characterization of ultra-thin films of some novel amphiphilic molecules at air-water (Langmuir monolayer) and air-solid (LB film) interfaces. The molecules studied were of different structure and shape. They can be broadly classified into two types viz., (a) azobenzene molecules and (b) derivatives of discotic molecules. The molecules were synthesized in our institute. To study the ultra-thin films of these molecules at air-water interface, we have used surface manometry and Brewster angle microscopy techniques. We have used atomic force microscope (AFM) extensively in different modes to extract information on surface topography and nanoscale electrical conductivity of the LB films. In chapter 1 we have described the experimental techniques along with a brief introduction to the Langmuir monolayers and LB films. Since a few of the materials studied were mesogenic, we have also given a brief introduction to liquid crystals.

In chapter 2, we have presented our studies on the assembly and organization of novel H-shaped mesogenic dimer molecule, 12D1H (Bis[5-(4'-n-dodecyloxy benzoyloxy)-2-(4"-methyl phenylazo)phenyl] adipate). Figure 1 shows the chemical structure of the molecule. The material 12D1H exhibited stable monolayer. Surface manometry and BAM studies

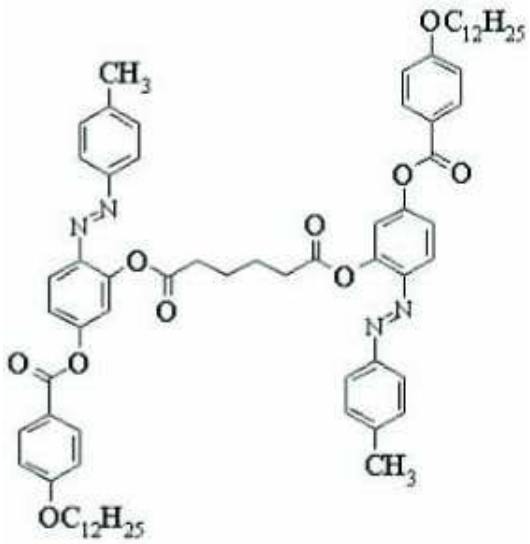

Figure 1: Chemical structure of the H-shaped molecule, 12D1H.

showed that the monolayer exhibited coexistence of gas and low density liquid phase at large A_m. On compression, the monolayer formed uniform low density liquid phase at A_m of 2.10 nm^2 before collapsing at an A_m of 1.84 nm^2 with a collapse pressure of 1.8 mN/m. Figure 2 shows the $\pi - A_m$ isotherm of 12D1H monolayer taken in dark. The wetting behavior of the 12D1H LB film transferred onto hydrophilic and hydrophobic substrates was studied using AFM. LB film transferred onto a mica substrate exhibited monolayer domains (Figure 3). From the AFM image and $\pi - A_m$ isotherm we infer that the ester groups of 12D1H are anchoring the molecules at the surface. Figure 4 shows the schematic diagram of the organization of the molecules at the interface. Figure 5 shows 3D view of the AFM topography image on a hydrophobic silicon substrate. We find that the bilayer transferred onto a hydrophobic silicon substrate, dewetted to form nano-droplets of size of about 100 nm. Our analysis of the AFM images indicated that the dewetting process is through spinodal dewetting. Controlled dewetting of the films of azobenzene compounds can have potential applications in optical devices, biochip technology and in microelectronics.

In azobenzene materials, molecular conformation can be changed from *trans* to *cis* state or *cis* to *trans* state by photoisomerization. This property of reversible molecular isomerization has been utilized in developing photosensitive devices [4, 5] and wetting surfaces [6].

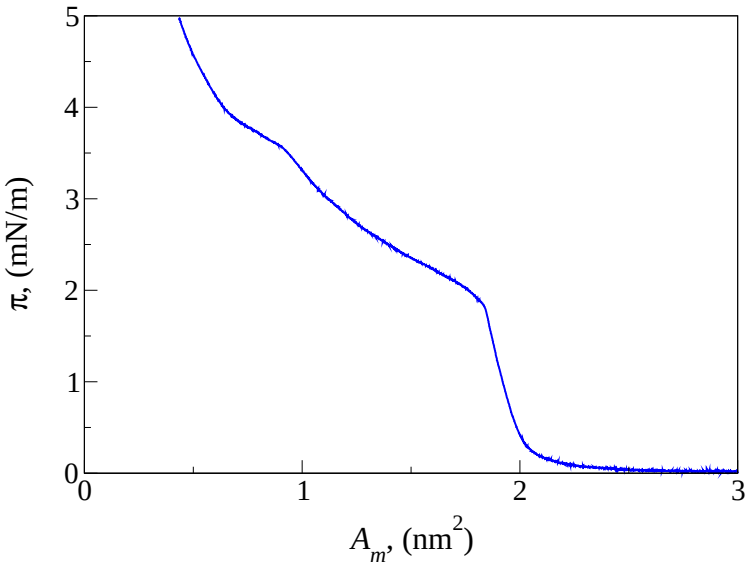

Figure 2: Figure shows the surface pressure (π)−area per molecule (A_m) isotherm for the 12D1H monolayer in dark compressed with constant barrier speed.

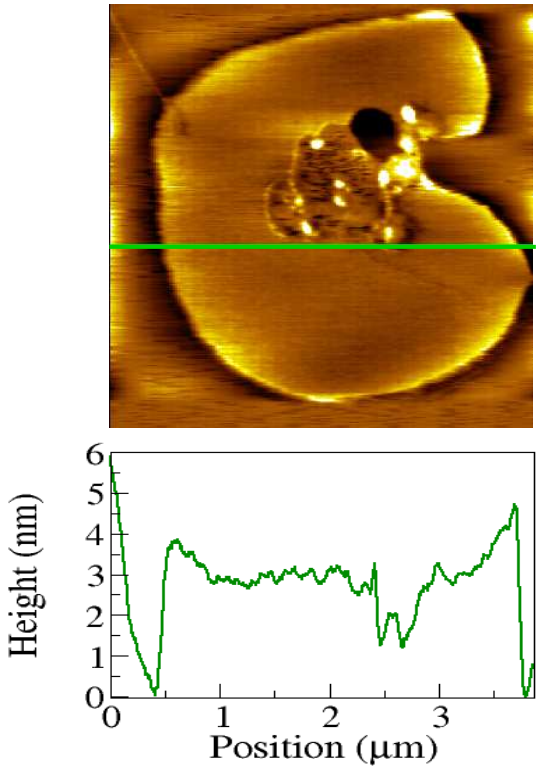

Figure 3: AFM image of 12D1H monolayer on hydrophilic mica substrate.

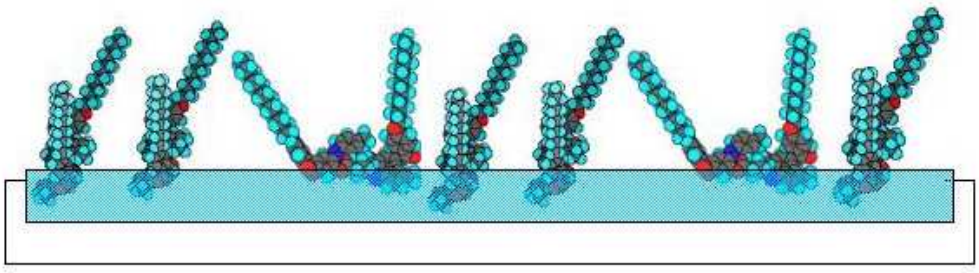

Figure 4: Schematic representation of the arrangement of molecules at air-water interface. This is based on the limiting area of 2.01 nm^2 obtained from $\pi - A_m$ isotherm and the height of 3.8 nm obtained from the AFM image of the monolayer film on a hydrophilic mica substrate. Here the ester groups of the molecule are in contact with water surface and the alkyl chains are protruded into air.

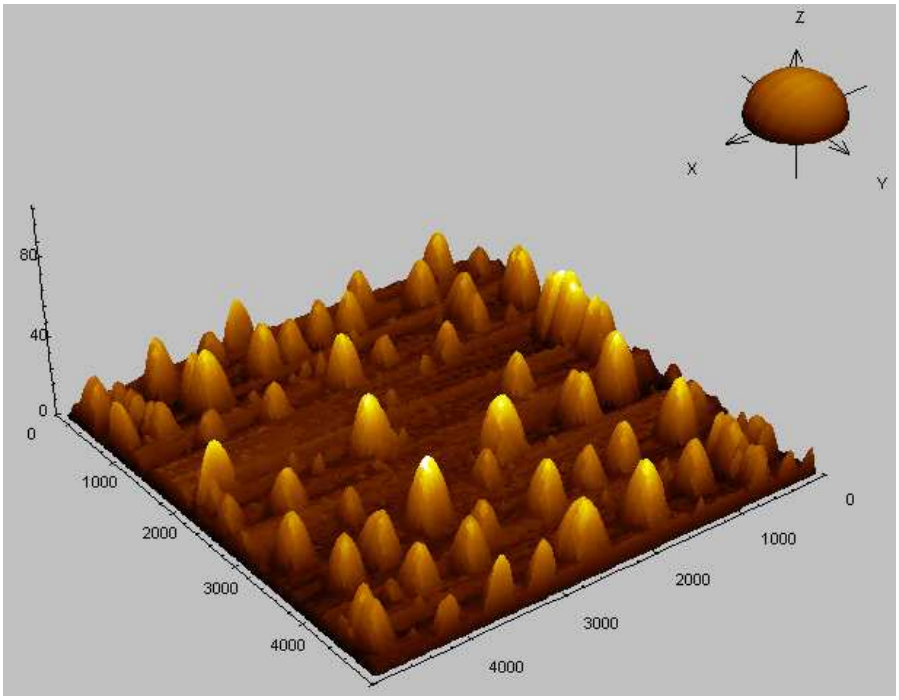

Figure 5: 3D view of AFM image of small droplets on a hydrophobic silicon substrate (X, Y and Z scales are in nm).

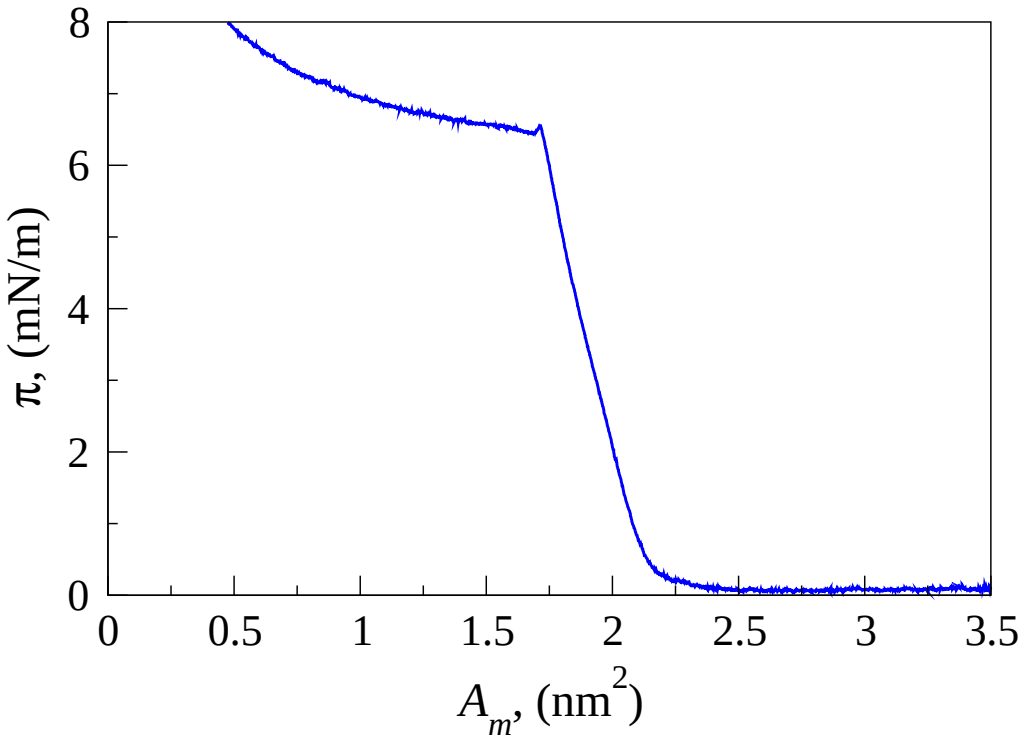

Figure 6: Figure shows the surface pressure (π)−area per molecule (A_m) isotherm for the monolayer in the presence of UV light of wavelength 365 nm.

For many such applications, understanding the kinetics of isomerization reaction on illumination of ultraviolet (UV) or visible light in thin film is important. In chapter 2, we present our studies on the effect of UV/visible light on the Langmuir monolayer of 12D1H. We find that the monolayer in the presence of UV light (*cis*-12D1H monolayer) is even more stable with a collapse pressure about three times higher to that of the monolayer in dark (*trans*-12D1H monolayer). Figure 6 shows the $\pi - A_m$ isotherm of the 12D1H monolayer obtained in the presence of UV light of wavelength 365 nm. We have also described our studies on the kinetics of *trans* to *cis* isomerization of the azobenzene molecules under the illumination of UV light in the low density liquid phase of the Langmuir monolayer. We find that the isomerization of the *trans*-12D1H molecules to form *cis*-12D1H leads to increase in the surface pressure of the monolayer. Figure 7 shows the variation of π as a function of time (t) for three different values of A_t. From our analysis, we find that the *trans* to *cis* isomerization reaction shows deviation from the first order kinetics. We attribute this deviation to the simultaneous photoisomerization of *trans* isomers to form *cis* isomers and the reverse

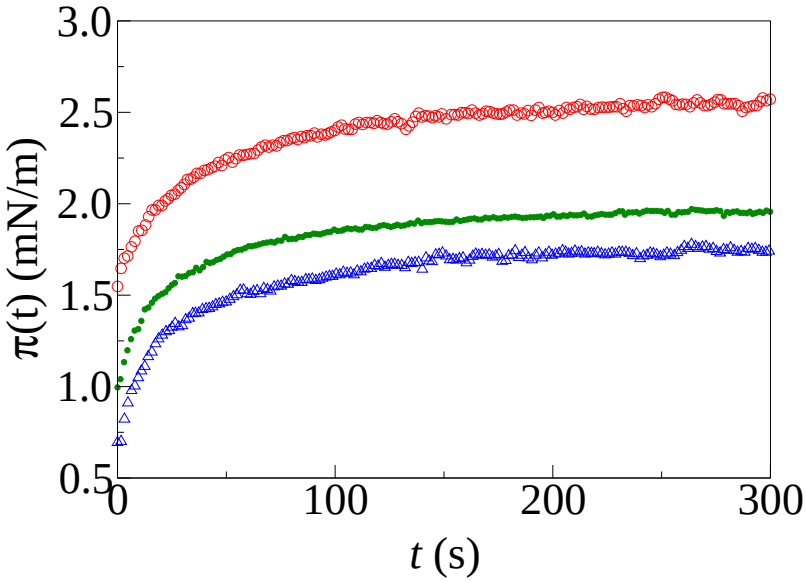

Figure 7: Variation of surface pressure as a function of time for three different target area per molecule (A_t); (*i*) 1.87 nm^2 (open circles), (*ii*) 1.92 nm^2 (filled circles) and (*iii*) 1.96 nm^2 (triangles), under the illumination of UV light. The corresponding π_{sat} values are (*i*) 2.67 mN/m, (*ii*) 2.03 mN/m and (*iii*) 1.83 mN/m, respectively.

thermal isomerization of the metastable *cis* isomers to form *trans* isomers. We find that the rate equation written by considering a first order kinetics for *trans* to *cis* photoisomerization reaction and a second order kinetics for *cis* to *trans* thermal isomerization reaction is in agreement with the rate equation obtained from the experimental data. The second order kinetics mechanism for thermal isomerization reaction of *cis* isomer to form *trans* isomer is similar to the Lindemann-Hinshelwood mechanism for the unimolecular reactions at low concentration of the reactants [7, 8].

In chapter 4, we describe our studies on the monolayer of a novel dimer of disk shaped triphenylene moiety, terephthalic acid bis-[6-(3,6,7,10,11-pentahexyloxy-triphenylen-2-yloxyl)-hexyl] ester (tp-dimer), at air-water interface. Figure 8 shows the chemical structure of the molecule. We find that the material tp-dimer forms metastable monolayer at air-water interface. The $\pi - A_m$ isotherm obtained by compressing the monolayer at a rate of 0.10 nm^{2}molecule^{-1}min^{-1} and at a temperature of 15°C is shown in Figure 9. Figure 10 shows the Brewster angle microscopy (BAM) image of tp-dimer monolayer exhibiting coexistence of gas and low density liquid phase, uniform phase and collapsed state. From the $\pi - A_m$

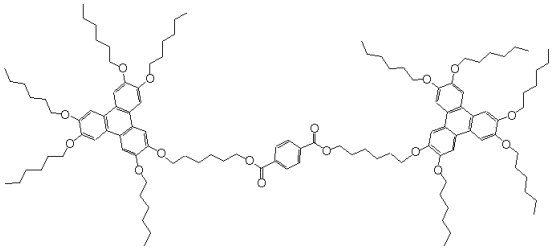

Figure 8: Chemical structure of tp-dimer.

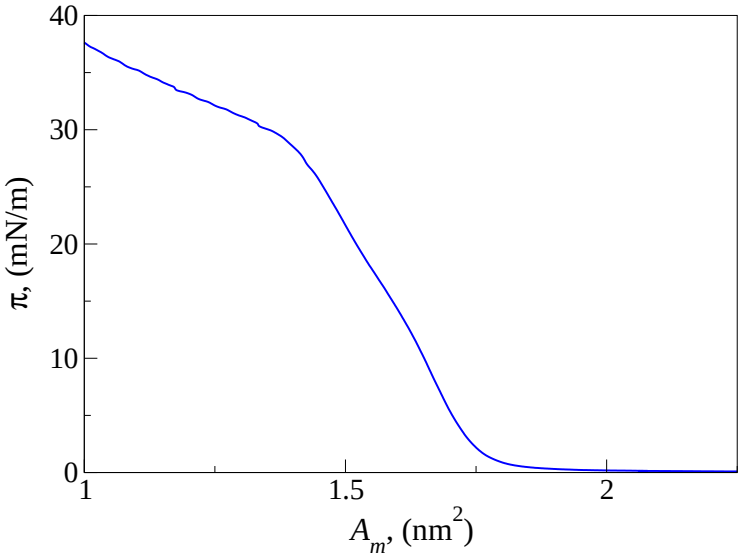

Figure 9: Surface pressure (π) – area per molecule (A_m) isotherm for tp-dimer monolayer at 15°C. The monolayer was compressed with a rate of 0.10 nm^{2}molecule^{-1}min^{-1}.

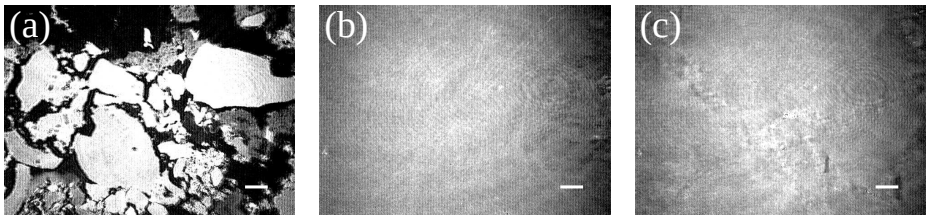

Figure 10: BAM images of the tp-dimer monolayer at different area per molecule. (a) Shows coexistence of gas phase (dark region) and liquid condensed phase (grey region) at A_m of 3.00 nm^2. (b) Shows uniform phase at A_m of 1.70 nm^2. (c) Shows the collapsed state at A_m of 1.61 nm^2. The scale bar in each image represents 500 μm.

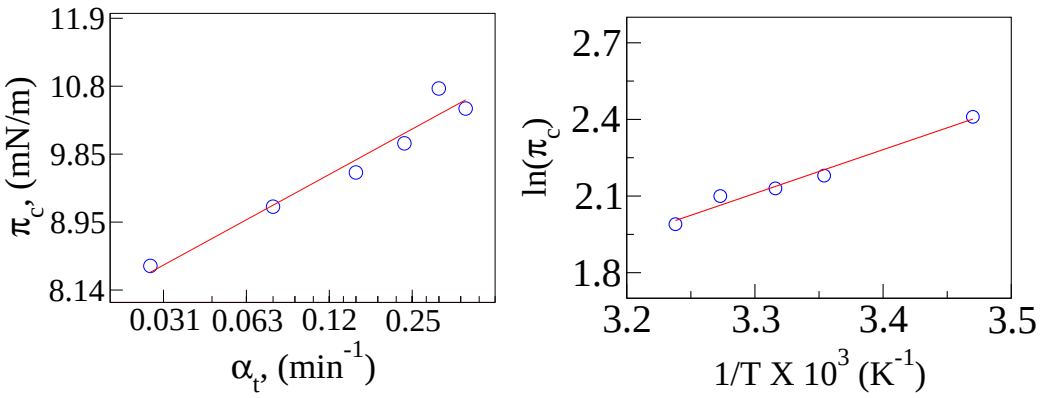

Figure 11: (a) Shows variation of collapse pressure (π_c) as a function of strain rate (α_t) at 25°C. The solid line represents the power law fit ($\pi_c = C_1\alpha_t^{1/n}$) to the data points. (b) Shows the variation of ln(π_c) as a function of $1/T$. The monolayer was compressed at a rate of 0.10 nm^{2}molecule^{-1}min^{-1}. Solid line represents the straight line fit to the data points.

isotherm, BAM and $|E|$ value, we infer that the monolayer when compressed with a rate of 0.10 nm^{2}molecule^{-1}min^{-1}, exhibited coexistence of gas and condensed phase at large value of A_m (above 1.80 nm^2). Below the A_m of 1.80 nm^2 the monolayer exhibited uniform condensed phase and collapsed at an A_m of 1.63 nm^2 with a collapse pressure of 11.7 mN/m.

We have studied the collapse of the tp-dimer Langmuir monolayer at air-water interface as a function of compression rate and temperature. We find that the collapse pressure increases with increase in compression rate. We consider the surface pressure of monolayer as stress and compression of monolayer as strain. The strain rate is calculated from the compression rate. Our analysis indicate that the strain rate is related to the collapse pressure by a power law. Similar power law has been reported in the case of Langmuir monolayers of dendrimers [9] and alkanethiol molecules [10]. Figure 11(a) shows the variation of collapse pressure as a function of strain rate at a temperature of 25°C. Our studies on the effect of temperature on the collapse pressure showed that the collapse pressure decreases with increase in temperature. Assuming the Arrhenius temperature dependence of the strain rate, we have calculated the activation energy for the collapse of monolayer from the variation of ln(π_c) as a function of $1/T$ (Figure 11(b)). The calculation of activation energy yields the value of 158.6 kJ/mol.

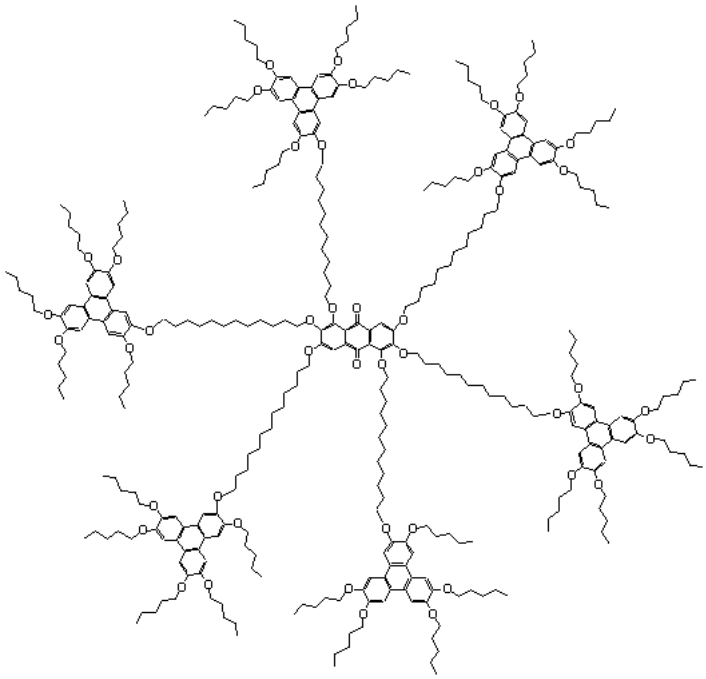

Figure 12: Chemical structure of AQD6 molecule. The anthraquinone core is connected to six triphenylene moieties by dodecyloxy chain through ether linkage. The triphenylene is substituted with five pentyloxy chains.

In chapter 5, we have studied the Langmuir monolayer and LB films of a star shaped liquid crystalline oligomer made up of disk shaped moieties, hexatriphenylene substituted anthraquinone (AQD6). The molecule has a central core of electron deficient anthraquinone which is connected to six disk shaped, electron rich triphenylene moieties by flexible alkyl chains. Figure 12 shows the chemical structure of the AQD6 molecule. We find that the material AQD6 forms stable monolayer. Figure 13 shows the $\pi - A_m$ isotherm. From the $\pi - A_m$ isotherm, $|E|$ value and BAM images, we infer that above an A_m of 7.0 nm^2, the monolayer exhibited coexisting gas and L_1 phase and between 7.0 nm^2 and 6.2 nm^2 it exhibited a uniform L_1 phase. The LB film transferred onto the mica and gold coated silicon substrates were studied using AFM. The limiting area of the molecule in the Langmuir monolayer and height of the LB film obtained from AFM studies suggest that the anthraquinone moiety is in face-on configuration on the substrate and the triphenylene moiety is in edge-on configuration extended away from the substrate. We have studied the electrical conductivity of the AQD6 monolayer transferred onto a gold coated silicon substrate using current sensing AFM

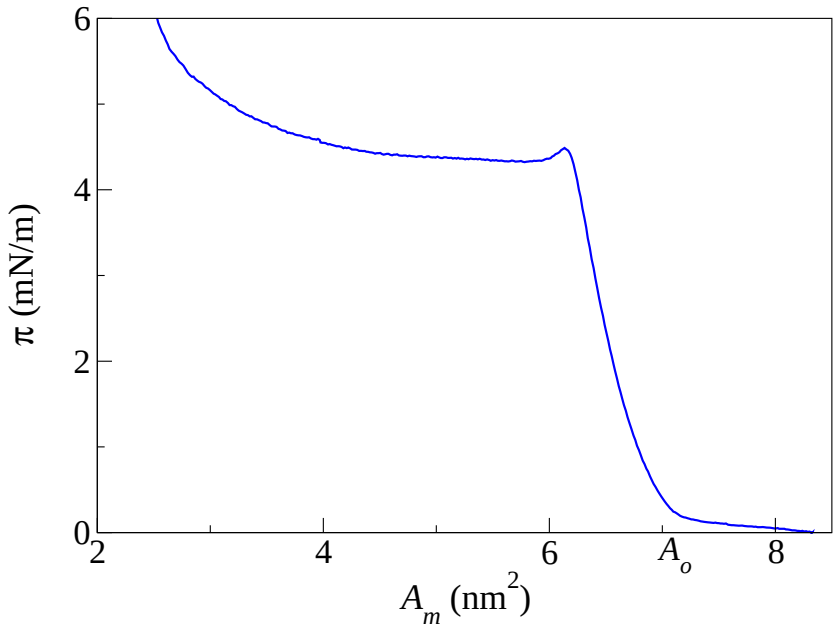

Figure 13: Surface pressure (π)−area per molecule (A_m) isotherm of the AQD6 monolayer at air-water interface at a temperature of 24.0 ± 0.1°C.

(CSAFM). The AQD6 monolayer film between the tip and the substrate forms metal-film-metal junction. The AQD6 monolayer introduces a potential barrier for the electron transfer. Our analysis of the current (I)−voltage (V) characteristics indicated that the electron transfer across the film is through a tunneling process. Further, as the bias voltage is increased gradually, we find a transition in the tunneling mechanism, from direct tunneling to injection tunneling, which is also known as Fowler-Nordheim tunneling (Figure 14).

In chapter 6, we report our studies on the polymers of triphenylene moiety and anthraquinone moiety. Here the polymer of triphenylene (Trp) is electron rich and the polymer of anthraquinone (Aqp) is electron deficient. Figure 15 shows the chemical structure of the polymers, Trp and Aqp. We find that the Trp and Aqp molecules form stable monolayer at air-water interface. Figure 16 shows the $\pi - A_m$ isotherm of Trp and Aqp molecules. The Trp monolayer exhibited gas phase at high area per molecule. On compression, it transformed into uniform low density liquid phase at an A_m of 19 nm^2. At an A_m of 14 nm^2 the monolayer collapsed with a collapse pressure of 6.3 mN/m. The monolayer of Aqp exhibited coexistence of the low density liquid (L_1) phase and gas phase for high values of A_m. On compression the monolayer smoothly transformed to an uniform L_1 phase. The Aqp mono-

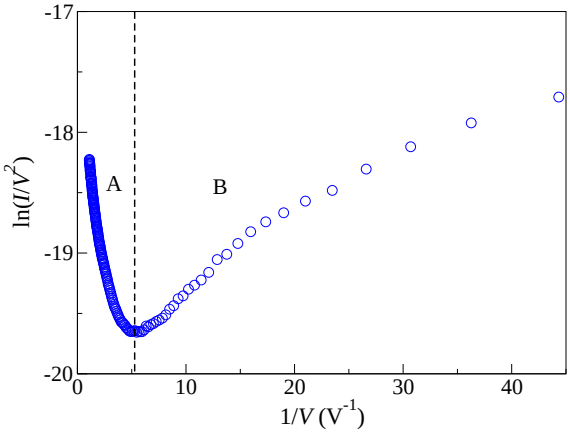

Figure 14: Variation of $\ln(I/V^2)$ as a function of $1/V$ showing injection tunneling regime (A) and direct tunneling regime (B) separated by a dashed line. Logarithmic increase of $\ln(I/V^2)$ can be seen for direct tunneling and the linear decay of $\ln(I/V^2)$ can be seen for injection tunneling. The dashed line shows the transition point.

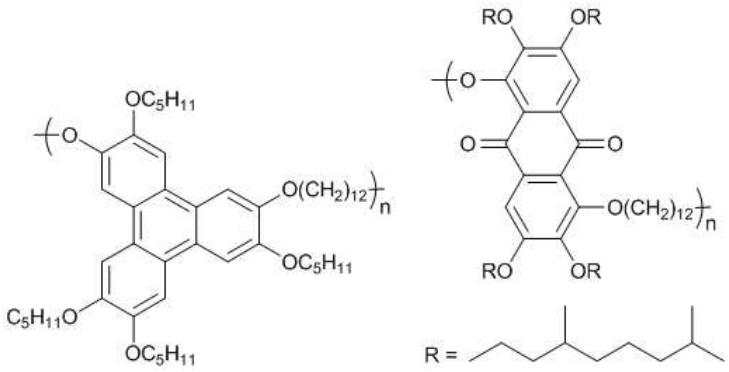

(a) Triphenylene polymer (b) Anthraquinone polymer

Figure 15: Chemical structure of (a) triphenylene polymer (Trp) and (b) anthraquinone polymer (Aqp). The molecular weight of Trp was about 13, 515 and that of Aqp was about 13, 691.

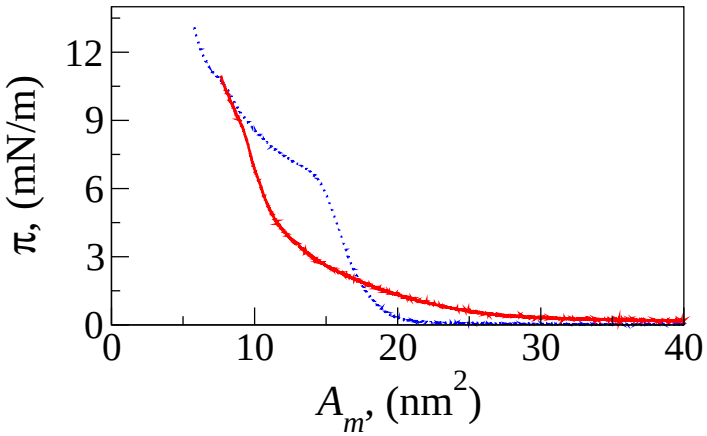

Figure 16: Surface pressure(π)−area per molecule(A_m) isotherm of Trp (blue curve) and Aqp (red curve).

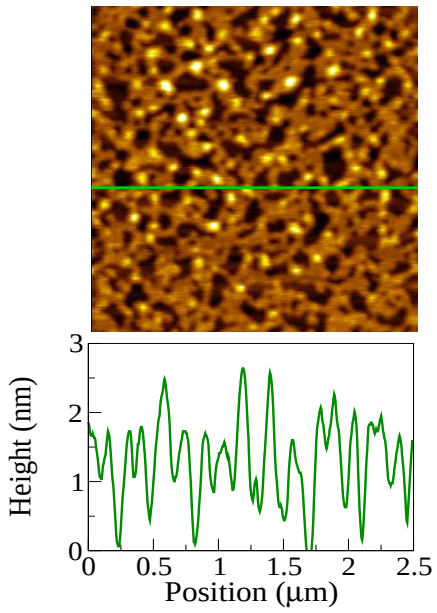

Figure 17: AFM topography image of LB film of the material Trp on a hydrophilic mica substrate.

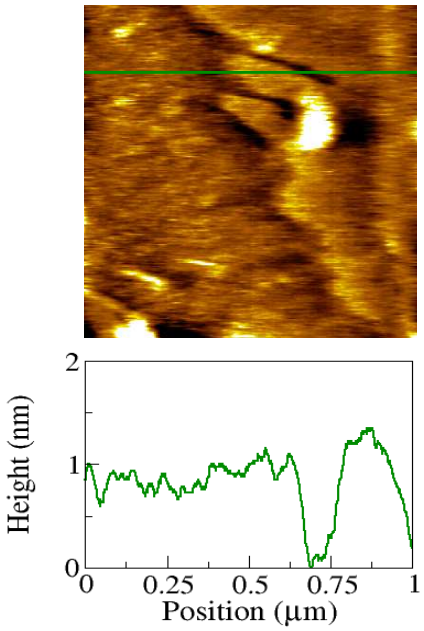

Figure 18: AFM topography image of LB film of the material Aqp on a hydrophilic mica substrate.

layer collapses at an A_m of 9.2 nm^2 with a collapse pressure of about 8.6 mN/m. The LB films of Trp and Aqp transferred onto solid substrates were studied using AFM. Figure 17 shows an AFM image of the Trp monolayer transferred onto a hydrophilic mica substrate at a surface pressure of 5 mN/m. AFM studies of the Trp LB film on the hydrophilic mica substrate and the limiting area value obtained from the $\pi - A_m$ isotherm suggest that the triphenylene moieties in the Trp monolayer are in edge-on configuration. Similarly, from the AFM topography images of the LB film of the material Aqp transferred onto a hydrophilic mica substrate (Figure 18), we infer that the anthraquinone moieties of the Aqp molecules are in edge-on configuration on the substrate.

In chapter 7, we report the nanoscale electrical conductivity studies carried out on the ultrathin films of novel liquid crystalline polymers of triphenylene and anthraquinone. The triphenylene polymer (Trp) is electron rich and the anthraquinone polymer (Aqp) is electron deficient. Monolayers of these materials were transferred by LB technique onto a gold coated silicon substrate. Current sensing atomic force microscope (CSAFM) was employed to study the nanoscale electrical conductivity of the LB films. We find that the electron transfer

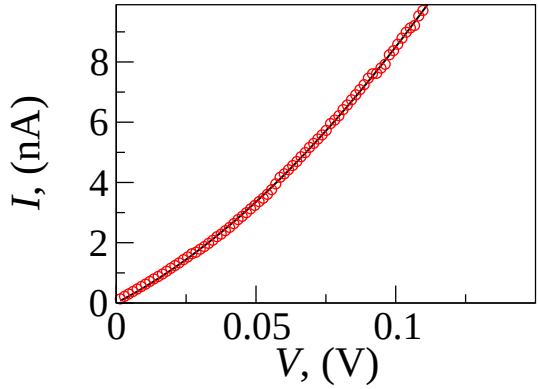

Figure 19: Variation of I as a function of V for the triphenylene polymer monolayer. The data represented by the open circles is fitted to the $I - V$ relation (solid line). The barrier height of the film obtained from the fit parameter was 2.48 eV.

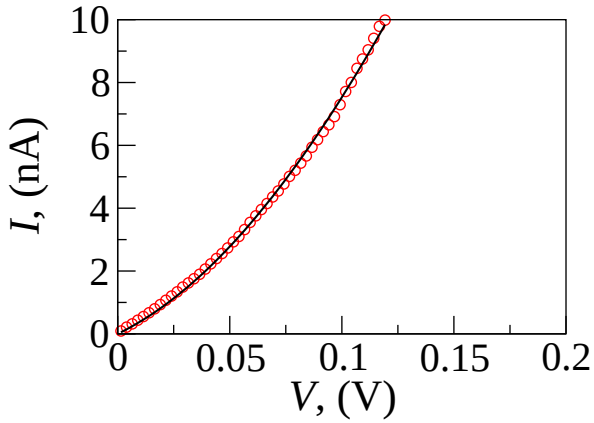

Figure 20: Variation of I as a function of V for the anthraquinone polymer monolayer. The data represented by the open circles is fitted to the $I - V$ relation (solid line). The barrier height of the film obtained from the fit parameter was 1.95 eV.

through metal-Trp-metal and metal-Aqp-metal junctions was through direct tunneling.

We have analyzed the $I-V$ characteristics of the Trp (Figure 19) and Aqp (Figure 20) film by using the $I - V$ relation for metal-insulator-metal junction suggested by Simmons [11]. We find that the barrier height ($\phi_\circ$) for metal-Trp-metal and metal-Aqp-metal junctions was about 2.48 eV and 1.95 eV, respectively.

In summary, this thesis describes our studies on the Langmuir monolayers and Langmuir-Blodgett (LB) films of azobenzene molecule and derivatives of some discotic molecules of novel structures. The monolayer film of H-shaped azobenzene dimer (12D1H) at air-water interface and its wetting properties on the hydrophilic and hydrophobic substrates were stud-

ied. We find that the bilayer film of 12D1H transferred onto a hydrophobic substrate dewetts by spinodal dewetting to form droplets. We have also described the kinetics of *trans* to *cis* isomerization on illumination of ultraviolet light. Our studies on the Langmuir monolayer of tp-dimer showed that the collapse pressure of the monolayer increases with increase in strain rate and they are related by a power law. The nanoscale electrical conductivity studies of AQD6, Trp and Aqp films were studied using CSAFM. The LB film of AQD6 molecule, which has both electron deficient anthraquinone moiety and electron rich triphenylene moiety, showed a transition from direct tunneling to injection tunneling mechanism as the applied bias voltage is increased. Our studies on the Langmuir monolayers and LB films of Trp and Aqp molecules showed that the discotic moieties were in edge-on configuration. Though the Trp molecule is electron rich and Aqp molecule is electron deficient, our CSAFM studies on the metal-Trp-metal and metal-Aqp-metal junctions indicated that the charge transfer was through direct tunneling.

Publication of articles related to this thesis work:

1. Novel Mesogenic Azobenzene Dimer at Air-Water and Air-Solid Interfaces.
   Bharat Kumar, A. K. Prajapati, M. C. Varia, and K. A. Suresh, *Langmuir* **25**, 843 (2009).

2. Kinetics of *trans-cis* isomerization in the azobenzene dimers at air-water interface.
   Bharat Kumar, and K. A. Suresh, *Phys. Rev. E* **80**, 021601 (2009).

3. Stress-strain relation in the collapsed Langmuir monolayer of dimer of disc shaped moiety.
   Bharat Kumar, K. A. Suresh, S. K. Gupta, and Sandeep Kumar (under review).

4. Direct to injection tunneling transition in the Langmuir-Blodgett film of a novel star shaped liquid crystalline oligomer.
   K. A. Suresh, Bharat Kumar, H. K. Bisoyi, and Sandeep Kumar (under review).

Following manuscript is under preparation:

- Current sensing AFM studies on the polymers of electron rich and electron deficient moieties.
  Bharat Kumar, K. A. Suresh, H. K. Bisoyi, and Sandeep Kumar

Bibliography

[1] G. L. Gaines Jr., *Insoluble Monolayers at Liquid Gas Interface*, Interscience: New York, (1966).

[2] M. M. Lipp, K. Y. C. Lee, J. A. Zasadzinski, and A. J. Waring, *Science* **273**, 1196 (1996).

[3] V. M. Kaganer, H. Mohwald, and P. Dutta, *Rev. Mod. Phys.* **71**, 779 (1999).

[4] A. Kocer, M. Walko, W. Meijberg, and B. L. Feringa, *Science* **309**, 755 (2005).

[5] X. Feng, L. Feng, M. Jin, J. Zhai, L. I. Jiang, and D. Zhu, *J. Am. Chem. Soc.* **126**, 62 (2004).

[6] H. S. Lim, J. T. Han, D. Kwak, M. Jin, and K. Cho, *J. Am. Chem. Soc* **128**, 14458 (2006).

[7] C. A. Hollingsworth, P. G. Seybold, L. B. Kier, and C. K. Cheng, *Int. J. Chem. Kinet.* **36**, 230 (2004).

[8] P. Atkins, *Physical Chemistry* (Oxford University Press, 2006).

[9] J. P. Kampf, C. W. Frank, E. E. Malmström, and C. J. Hawker, *Science* **283**, 1730 (1999).

[10] P. Burriel, J. Claret, J. Ignes-Mullol, and F. Sagues, *Eur. Phys. J. Special Topics* **143**, 165 (2007).

[11] J. G. Simmons, *J. Appl. Phys.* **34**, 1793 (1963).

Chapter 1

Introduction

1.1 Amphiphiles

Molecules containing hydrophilic (water loving) part and hydrophobic (water hating) part are known as 'amphiphiles'. Typical examples for amphiphilic molecules are long chain fatty acids like stearic acid ($C_{17}H_{35}COOH$). The carboxyl (-COOH) group of the fatty acids acts like hydrophilic part and the alkyl chain acts like hydrophobic part. Other class of organic molecules containing a hydrophilic group like -CH_2OH, -CN, -COO-, -$CONH_2$, -CH=NOH, -C_6H_4OH, -CH_2COCH_3, -$NHCOCH_3$, etc., along with a balancing hydrophobic group can also be amphiphilic [1]. Amphiphiles are abundantly found in nature. In biological systems, amphiphiles play a very important role in different activities. The lipid molecules (like phospholipids), steroids (like cholesterol) and proteins are a few examples of amphiphiles found in biological systems [2, 3].

When amphiphilic molecules are put on the water surface, the hydrophilic part anchors to the water surface due to its interaction with the water molecules. The hydrophobic part of the molecules stay away from the water. If the molecules possess a proper balance of hydrophilic part and hydrophobic part, they spread over the water surface to form a stable monolayer. Figure 1.1 shows a cartoon of an amphiphilic molecule and the schematic representation of amphiphiles spread at air-water interface.

The stability of monolayers formed by amphiphilic molecules depends on various fac-

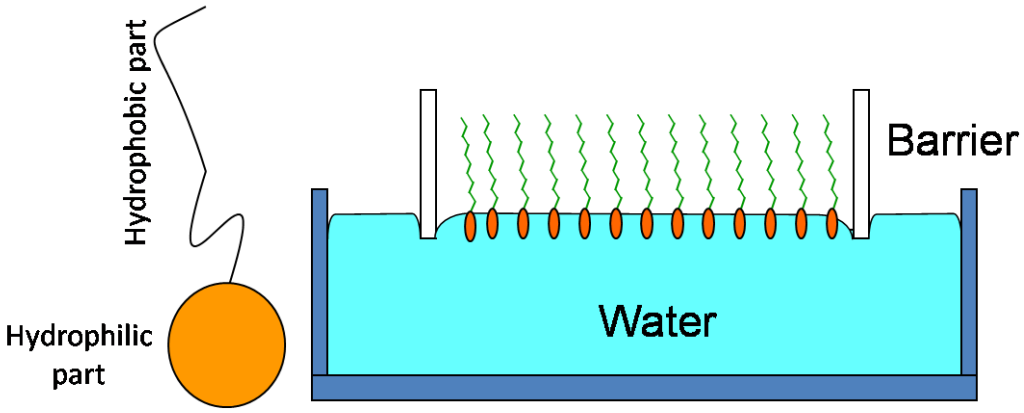

Figure 1.1: Figure shows a cartoon of an amphiphilic molecule and the schematic representation of amphiphiles spread at air-water interface.

tors like interaction between the hydrophilic group and subphase, interaction between the hydrophilic groups and also interaction between the hydrophobic groups. The hydrophilic group of an amphiphile can interact with subphase by forming hydrogen bond with water molecules, or by the charge transfer process.

1.2 Liquid crystals

Liquid crystals are a state of matter which has properties intermediate to that between liquids and crystals [4]. They share the properties of liquids like high mobility of molecules and they also exhibit few of the properties of crystals like orientational and positional ordering in one or two dimensions. Since they have properties intermediate between that of crystals and liquids they are also called as intermediate phases or mesophases. Figure 1.2 shows the schematic of the organization of molecules in crystal phase, liquid crystal phase and isotropic phase. In crystal phase, the molecules have long range positional and orientational order. In the liquid crystal phase, the molecules have orientational order and partial or no positional order. In the isotropic phase, the molecules do not have any ordering. The materials exhibiting liquid crystal phases are known as mesogens. The mesogens in the liquid crystalline phase belong to a class known as soft condensed matter, which comprises of variety of physical states that can be easily deformed by thermal stresses or thermal fluctuations. Liquid

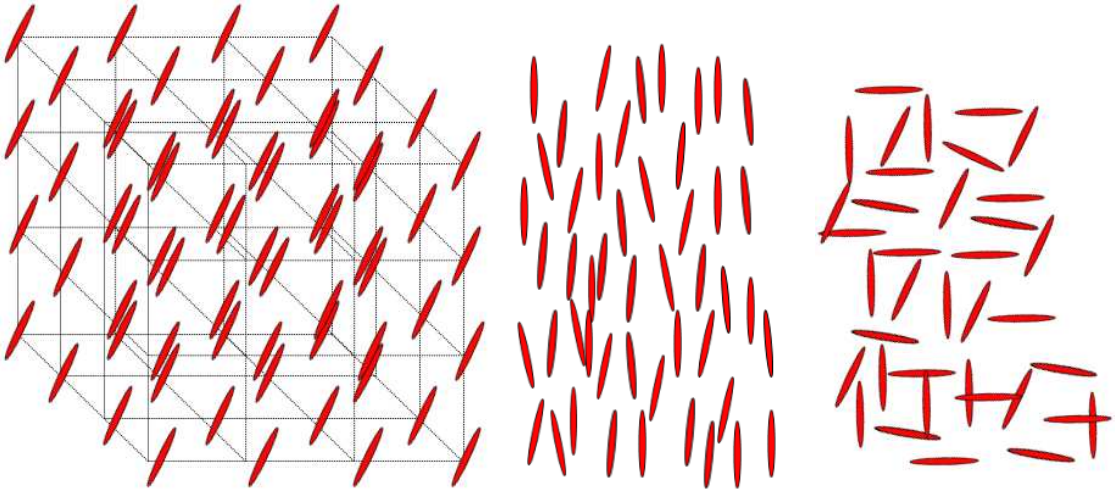

(a) Crystal (b) Liquid crystal (c) Liquid

Figure 1.2: Figure shows the schematic representation of the organization of molecules in (a) crystal phase, (b) liquid crystal phase and (c) isotropic phase.

crystalline molecules have anisotropy in their structure or functionality or both [5]. They can be broadly classified into two categories: (1) thermotropic liquid crystals, where the liquid crystal phase formation is temperature dependent and (2) lyotropic liquid crystals, where the liquid crystal phase formation depends on solvent and concentration. Thermotropic liquid crystals find applications in electro-optic devices (like displays), temperature and pressure sensors. These systems are also of interest from the point of basic research as they exhibit rich phase behavior and phase transitions. Lyotropic liquid crystals are also of great interest since they play an important role in the biological systems [6].

Depending on the molecular ordering, thermotropic and lyotropic liquid crystals are further classified into different phases. Since this thesis contains the studies on the films of thermotropic liquid crystals, a brief description of various thermotropic liquid crystals is given.

1.2.1 Calamitic liquid crystals

Rod like molecules (also known as calamitic molecules) with rigid core and flexible chains can exhibit liquid crystal phases. Such liquid crystals are known as calamitic liquid crystals. Common phases exhibited by these materials are explained below.

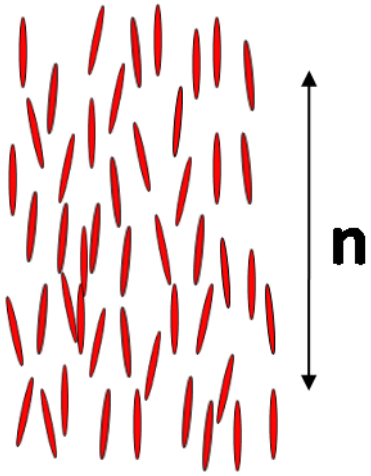

Figure 1.3: Figure shows the schematic representation of molecular organization in the nematic phase exhibited by calamitic molecules.

Nematic phase

In nematic liquid crystal phase, the molecules have only long range orientational order and no positional order. This is the least ordered liquid crystal phase. The word nematic comes from the Greek word *nematos* meaning thread. It refers to certain thread like defect patterns observed in this phase under the polarizing microscope. Calamitic molecules when cooled from isotropic phase can form nematic phase by spontaneous orientation of their long axis approximately parallel to a preferred direction. The preferred direction is called the director and is represented by an apolar unit vector **n**. Figure 1.3 shows the schematic representation of nematic phase exhibited by calamitic molecules.

Cholesteric phase

The cholesteric (or chiral nematic) liquid crystal phase is exhibited by mesogenic molecules which are chiral[1] in nature or by nematic liquid crystals doped with small quantity of chiral molecules. Figure 1.4 shows the schematic diagram of structure of cholesteric phase. In this phase all the molecules on an average arrange parallel to the director **n** just like in the nematic phase. However, the asymmetry in the constituent molecules causes a slight and gradual spontaneous rotation of the director. The director describes a helix with a specific

[1] An object or molecule is said to be chiral if it does not superimpose onto its mirror image.

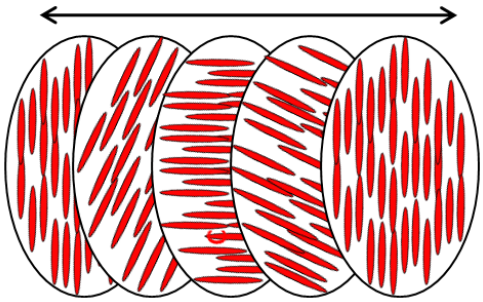

Figure 1.4: Figure shows the schematic representation of cholesteric phase exhibited by calamitic molecules. The arrow in the diagram represents half pitch length.

temperature dependent pitch (Figure 1.4).

Smectic phase

In smectic liquid crystals, the molecular organization has translational order in one dimension and liquid-like positional order in other directions. Smectic liquid crystals are layered structures with specific interlayer spacing. Within a layer the molecules possess liquid like order. The long molecular axis on an average is oriented collectively along one direction (**n**). If **n** is parallel to layer normal then the smectic phase is known as Smectic A phase and if **n** makes an angle (θ) with the layer normal **a** it is known as Smectic C phase. Figures 1.5(a) and 1.5(b) show the schematic representation of smectic A and smectic C phases exhibited by calamitic molecules, respectively. Depending on the molecular orientational ordering in the layers, smectic liquid crystals are further classified into Smectic B, Smectic E and Smectic F phases.

In addition to calamitic molecules, there are molecules of various shapes and high degree of structural anisotropy which also exhibit liquid crystal phases. Most common among them are disc shaped molecules and bent-core molecules. Disc shaped molecules exhibiting liquid crystal phase was first discovered in 1977 [7]. They are of great interest for many technological applications and have attracted many researchers since their discovery. In the following subsections we give a brief introduction to the phases exhibited by disc shaped mesogens (discotic liquid crystals).

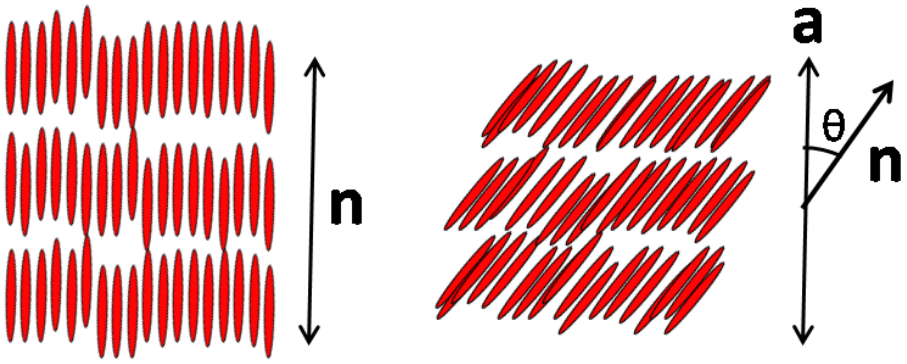

(a) Smectic A phase (b) Smectic C phase

Figure 1.5: Figure shows the schematic representation of molecular organization in (a) smectic A phase and (b) smectic C phase, exhibited by calamitic molecules.

1.2.2 Discotic liquid crystals

Molecules with flat, rigid, disc shaped core and flexible parts at the periphery can exhibit liquid crystal phases called discotic liquid crystals. The self-organization of the molecules due to interaction between the discotic cores, leads to the formation of various liquid crystal phases [8]. The discotic core is usually made of flat aromatic ring to which flexible parts like alkyl chains can be attached. Various aromatic cores with different molecular architectures have been reported to exhibit discotic phase. Examples of cores used to synthesize the discotic liquid crystals are benzene, triphenylene, anthraquinone, hexabenzocoronene, phthalocyanine, decacyclene, tricycloquinazoline, dibenze[g,p]chrysene, phenanathro-phenazine derivatives [8, 9] etc.,.

The discotic molecules can self-organize due to strong $\Pi - \Pi$ interaction between the aromatic cores and form column like structures. The length of the flexible peripheral substituents will determine the intercolumnar distances. Generally, the intercolumnar distance vary between $2 - 4$ nm. The strong $\Pi - \Pi$ interaction between the cores results in the high charge mobility along the column axis as compared to the charge mobility in the direction perpendicular to the column axis. This high anisotropy in the charge mobility results in quasi-one dimensional conductivity behavior [8]. Because of this property, discotic liquid crystals find applications in devices like field effect transistor, light emitting diode and photo

voltaic solar cell [10]. Hence these materials are known as new generation of organic semiconductors. Other applications where these molecules can be of potential use are liquid crystal displays, sensors and memory devices [11].

Like calamitic molecules, the discotic molecules also exhibit various liquid crystal phases depending on the organization of molecules. These liquid crystal phases can be broadly classified into following two categories.

Discotic nematic phase

This phase is similar to the nematic phase exhibited by calamitic liquid crystals. In this phase the molecules have only long range orientational order but no positional order. The molecules more or less stay parallel to each other and have full translational and rotational freedom about their short axis. Their long axes which span the plane of discotic core orient parallel to a general plane. If the discotic molecules are chiral in nature or if chiral dopant is added into discotic liquid crystals, the material may exhibit chiral discotic nematic phase. Here, similar to the cholesteric phase, there is a gradual change in the direction of orientation of the short axis. Also, in some discotic liquid crystals, the molecules may self organize into column like structures. Such a phase is called nematic columnar phase. In this phase, the columns themselves do not have any long range positional order, but have long range orientational order. Figure 1.6 shows the schematic representation of various discotic nematic phases.

Discotic columnar phase

In discotic columnar phase, the molecules stack themselves to form column like structures, which organize in a two dimensional lattice. The molecules in each column do not have long range positional order. Depending on the lattice formed by the columns the columnar phase can be classified into various categories viz., hexagonal, rectangular, oblique and lamellar phases. In columnar hexagonal phase, the columns organize in a two dimensional hexagonal lattice. The columnar rectangular phase is characterized by the rectangular lattice formed by

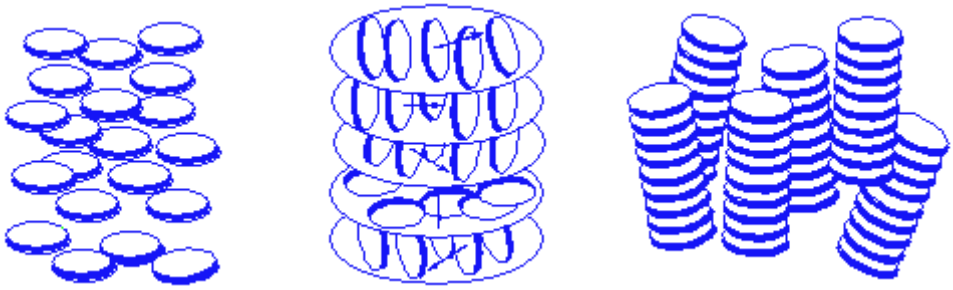

(a) Nematic phase (b) Chiral nematic phase (c) Nematic columnar phase

Figure 1.6: Figure shows the schematic representation of discotic nematic phases exhibited by disc shaped molecules. (a) Shows nematic phase (b) shows chiral discotic nematic phase and (c) shows nematic columnar phase.

the columns. In columnar oblique phase, the columns organize in a lattice with oblique unit cell. The columnar lamellar phase has the columns arranged in the layered structure. In all the cases the peripheral flexible parts like alkyl chains are disordered. Figure 1.7 shows the schematic representation of these phases.

1.3 Langmuir monolayers

Amphiphilic molecules possessing properly balanced hydrophilic group and hydrophobic group can form insoluble monolayers at air-water interface, as explained in section 1.1. Such mono-molecular films are known as Langmuir monolayers. Langmuir monolayers can be prepared by dissolving amphiphilic molecules in a volatile solvent and spreading the dilute solution over the water surface drop by drop. The volatile solvent evaporates and the molecules spread spontaneously over water surface with hydrophilic group in contact with water and hydrophobic group staying away from the water. Langmuir monolayers can be used as a model for the studies on the properties of two-dimensional systems. Also a wealth of useful information about molecular sizes and intermolecular forces can be obtained from the studies of monolayers on the water surface.

In analogous to the phases exhibited by the matter in bulk, Langmuir monolayers exhibit various two-dimensional phases depending on the thermodynamic conditions [12]. The phase transitions in the Langmuir monolayers can be brought out by changing the thermo-

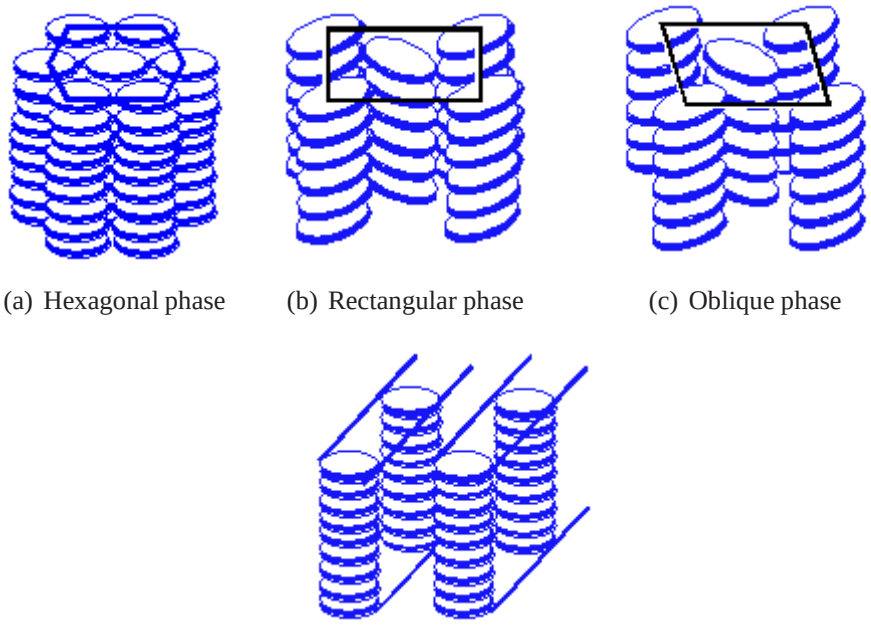

(a) Hexagonal phase (b) Rectangular phase (c) Oblique phase

(d) Lamellar phase

Figure 1.7: Figure shows the schematic representation of various discotic columnar phases exhibited by discotic molecules. (a) Shows hexagonal phase, (b) shows rectangular phase, (c) shows oblique phase and (d) shows lamellar phase.

dynamic parameters like surface density of the amphiphilic molecules, temperature etc. Another parameter used in the study of Langmuir monolayers is the surface pressure (π). It is defined as the difference in the surface tension of water with and without monolayer. When the surface density of the amphiphilic molecules is increased by compressing the monolayer, the area per molecule (A_m) decreases. The phase transitions in the Langmuir monolayers can be studied from the variation of π as a function of A_m at a constant temperature. This technique is called surface manometry and the detailed discussion of it is given in the next section. Apart from the thermodynamic parameters described above, other factors that could affect the phases exhibited by the Langmuir monolayers are polar groups, subphase, pH of the subphase, compression rate, ionic strength and humidity [1].

Langmuir monolayers are of considerable industrial importance. It has been found that on spreading them on the water surface, dramatic reduction in the evaporation rate of water occurs. Langmuir monolayers mimic biological membranes and studies on the monolayers of biological molecules will help in understanding the functionality of biological systems.

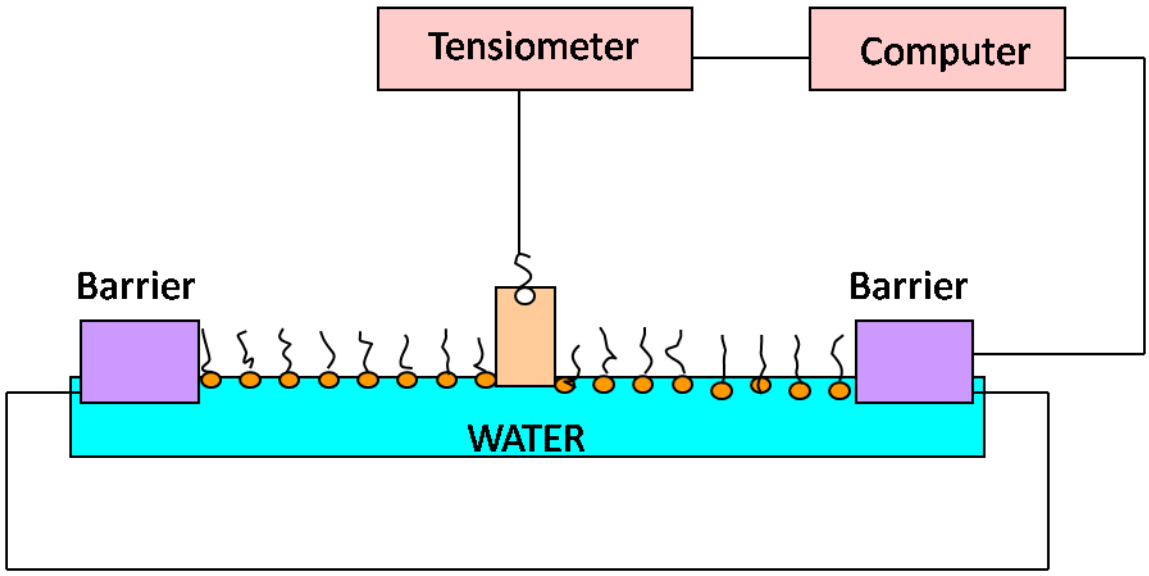

Figure 1.8: Schematic diagram of the experimental set up for the surface manometry.

Polypeptides like salmon calcitron are used in the bone formation and understanding its properties at interfaces will have useful implications in the treatment of osteopathies. The inside of the human lungs are lined by alveolar fluid consisting of amphiphiles like phospholipids. These amphiphiles maintain and regulate appropriate surface tension in the lungs and protect the lungs from collapsing. The deficiency of such amphiphiles may lead to breathing problems. The lining of amphiphiles in the lungs can be simulated in-vitro by Langmuir monolayers and studies have been carried out in this direction [13].

1.3.1 Surface manometry

The phase transitions in Langmuir monolayers can be studied by surface manometry. In this technique, the monolayer is compressed uniformly between the moving barriers and the surface pressure of the monolayer is measured as a function of surface density of molecules at constant temperature. Figure 1.8 shows a schematic diagram of the experimental set up for the surface manometry. We have used a Nima trough (Model: 611M) which is made up of teflon. The barriers are driven by a DC motor. The speed of the barriers can be varied between 1 – 100 $cm^2 min^{-1}$. The surface pressure was measured using Wilhelmy method. In

this method a filter paper was cut to a known dimension (1 cm in width and 2 cm in length) and cleaned by rinsing it in chloroform. The dried filter paper which acts like a Wilhelmy plate was suspended from the sensor head (tensiometer) using a hook and was immersed into the subphase. The water rises into the filter paper and after some time it equilibrates. In the Wilhelmy method, the force due to surface tension of water in the direction parallel to the surface normal is measured. The sensor generates an electric signal proportional to the force acting on the filter paper, which is calibrated using standard weights. The sensitivity of the sensor was 0.1 mN/m. The surface pressure π of the monolayer, which is the difference between the surface tension of water with and without monolayer film is given by,

$$\pi = \gamma_\circ - \gamma \tag{1.1}$$

where, $\gamma_\circ$ is the surface tension of pure water and γ is the surface tension of water with monolayer. Pure water at 20°C has a surface tension value of 72.8 mN/m.

The π value depends on the surface density of molecules. Hence, as the surface density of molecules is increased by compressing the monolayer between the barriers, the π value usually changes. Area per molecule (A_m) which is inverse of the surface density and the π values are simultaneously measured as the barriers are moved to compress the monolayer. The temperature of the system is kept constant. A typical variation of π as a function of A_m, also known as $\pi - A_m$ isotherm is shown in Figure 1.9. Traditionally, Langmuir monolayers can exhibit the following phases: Gas (G) phase, low density liquid phase (L_1) phase, high density liquid (L_2) phase, and solid (S) phase as the surface density of the molecules is increased by compressing the monolayer. These phases are discussed below.

Gas (G) phase

At very high A_m, the monolayer shows zero or negligible π value. In this phase, the molecules in the monolayer are far enough from each other so that they exert relatively little or no force on one another. This phase is called gas (G) phase. The interpretation of the $\pi - A_m$ behavior

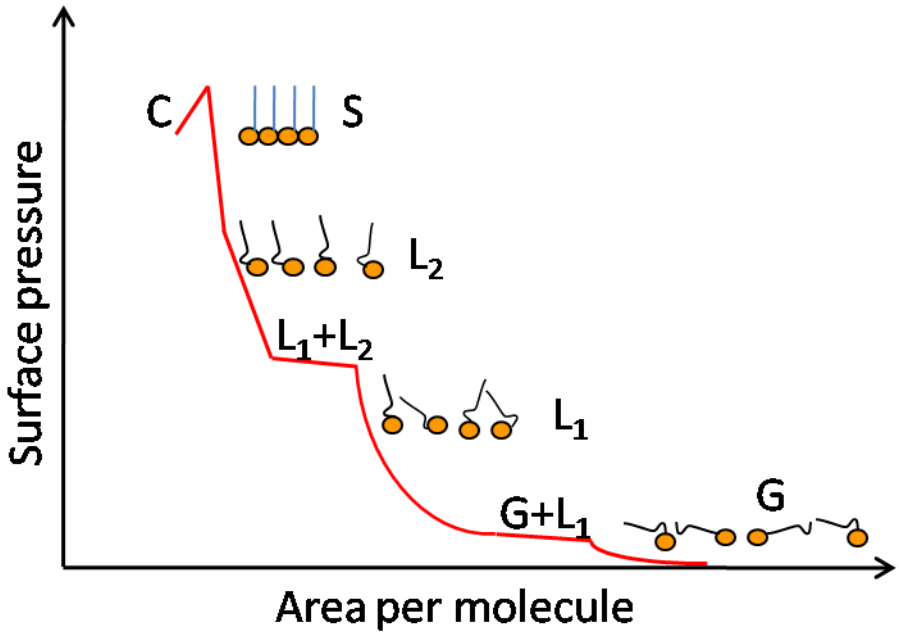

Figure 1.9: A typical $\pi - A_m$ isotherm indicating various phases in a Langmuir monolayer. The symbols G, L_1, L_2, S and C represent gas phase, low density liquid phase, high density liquid phase, solid phase and collapsed state, respectively. The kink in the isotherm is associated with a phase transition and the plateau region is associated with a co-existence region.

of gaseous monolayers can be done in analogy with the kinetic theory of 3D ideal gas [1]. The following equation of state can be written for the 2D gas phase.

$$\pi A_m = k_b T \tag{1.2}$$

where, k_b is the Boltzmann constant and T is the absolute temperature. Deviation from equation 1.2 has been reported for most of the monolayers, because of the assumption that the molecules occupy a little area. It was shown that the molecules in the gas phase lie flat over the surface and occupy significant area. Also it was assumed that there is no interaction between the amphiphilic molecules. However, as the monolayer is compressed, there will be some long range weak interaction between the molecules. This led to the addition of correction terms to the equation of state. Equation 1.2 modified with these van der Waals

correction factors is given below.

$$(\pi + a/A_m^2)(A_m - b) = k_b T \tag{1.3}$$

where, a incorporates interaction between the molecules, b takes into account the excluded area. The monolayer phase is usually characterized by the corresponding compressional modulus ($|E|$) values [14]. The compressional modulus of a monolayer can be calculated using the following expression.

$$|E| = A_m \left(\frac{\mathrm{d}\pi}{\mathrm{d}A_m} \right) \tag{1.4}$$

The $|E|$ value for the gas phase will be negligible.

Low density liquid (L_1) phase

The low density liquid (L_1) phase, also known as liquid expanded phase, is an intermediate phase between gaseous and condensed phases. The $\pi - A_m$ isotherm in this phase show considerable curvature. In this phase the molecules are randomly arranged as in the gas phase, but they are closer and interact with each other. The hydrophobic portions of the molecules are lifted from the water surface and have a random orientation. The $|E|$ value for this phase is in the range of 12.5 – 50 mN/m.

High density liquid (L_2) phase

In high density liquid (L_2) phase, also known as liquid condensed phase, the molecules are closely packed with quasi-long range positional order. The molecules in this phase may be tilted with respect to the monolayer plane. There are many variants of the L_2 phase. These phases can be classified depending on the molecular ordering and orientation. At low surface pressure the phases like L_2 and L_2' may appear. In L_2 phase the molecules have a collective tilt towards a nearest neighbour (NN) [15, 16]. In L_2' phase the molecules are tilted towards next-nearest neighbour (NNN) [17]. The $|E|$ value of this phase is in the range of 100 – 250 mN/m.

Solid (S) phase

At high surface pressure, the monolayer may exhibit two untilted condensed phases, viz., super liquid (LS) phase and solid (S) phase. The X-ray diffraction studies of the LS phase indicates a hexagonal structure [18, 19]. During compression the viscosity of the monolayer suddenly drops as soon as this phase occurs. Hence it is called super liquid phase. This phase has very low compressibility.

Solid (S) phase is a highly incompressible phase with closed pack arrangement of the molecules [20]. Here the hydrophobic part of the molecules is not tilted and they interact with each other strongly as the distance between the molecules is very low. This phase shows positional correlations larger than 50 nm. Hence it is dubbed as $2D$ crystal.

Collapsed state

On compressing the monolayer in the solid phase, the molecules in the monolayer will come out into the third dimension. This is referred as collapse of the monolayer and the surface pressure at which the monolayer collapses is known as collapse pressure (π_c). After collapse, the film either forms three dimensional crystallites or multilayers depending on the nature of molecules and subphase.

The stability of the monolayers at air-water interface can be measured in terms of equilibrium surface pressure. This is the surface pressure at which the monolayer coexists with its bulk phase at the air-water interface. Equilibrium surface pressure of a material can be measured by placing a speck of crystallite on the water surface. The molecules from the bulk crystallites elude out and form a monolayer at the interface spontaneously. After a certain period of time, the system reaches an equilibrium state where the rate of elution of molecules from crystallites is equal to the rate of molecules binding to the crystallites. The variation in surface pressure with time shows an initial increase in surface pressure, due to the formation of the monolayer, before reaching a saturated value. The saturated value of the surface pressure corresponds to an equilibrium state and is called equilibrium surface pressure (ESP). The ESP values of some amphiphilic molecules like stearic acid, octadecanol and dipalmi-

toyl phosphatidylcholine are 5.2, 34.3 and 1 mN/m, respectively [21]. The materials with higher ESP values form more stable monolayer.

1.3.2 Brewster angle microscopy

Brewster angle microscope commonly known as BAM, can be used to visualize the phases exhibited by the monolayer at air-water interface [22, 23, 24, 25]. When a light is incident on an interface at an angle equal to Brewster's angle, the reflected light will have almost zero in-plane polarization (*p*-polarization) component. This phenomenon can be found when the light is reflected by a denser medium.

The Brewster's angle for an interface depends on the refractive indices of the rarer and the denser media and is given by the following expression.

$$\theta_b = tan^{-1}\left(\frac{n_2}{n_1}\right) \tag{1.5}$$

where, n_1 and n_2 are the refractive indices of the rarer and denser media, respectively.

In our experimental setup, the *p*-polarized laser beam of wavelength 600 nm is incident on the water surface at Brewster's angle (53.1°). Hence, the reflection from the pure water surface will be zero. In the presence of the monolayer, the refractive index of the interface changes and the Brewster angle condition is no more satisfied. This results in the non-zero *p*-polarized component in the reflected light. The reflected light falls on a polarizer (which allows only *p*-polarized light to pass through) before getting detected by a CCD camera. The presence of *p* polarized component in the light reflected by the monolayer film gives the contrast. Figure 1.10 shows the schematic diagram of a Brewster angle microscope. The reflectivity at the interface is dependent on the factors like thickness, roughness and anisotropy of the monolayer. Domains with different orientation or tilt of the molecules will give rise to different contrasts, thus helping us to visualize the different phases exhibited by the monolayer.

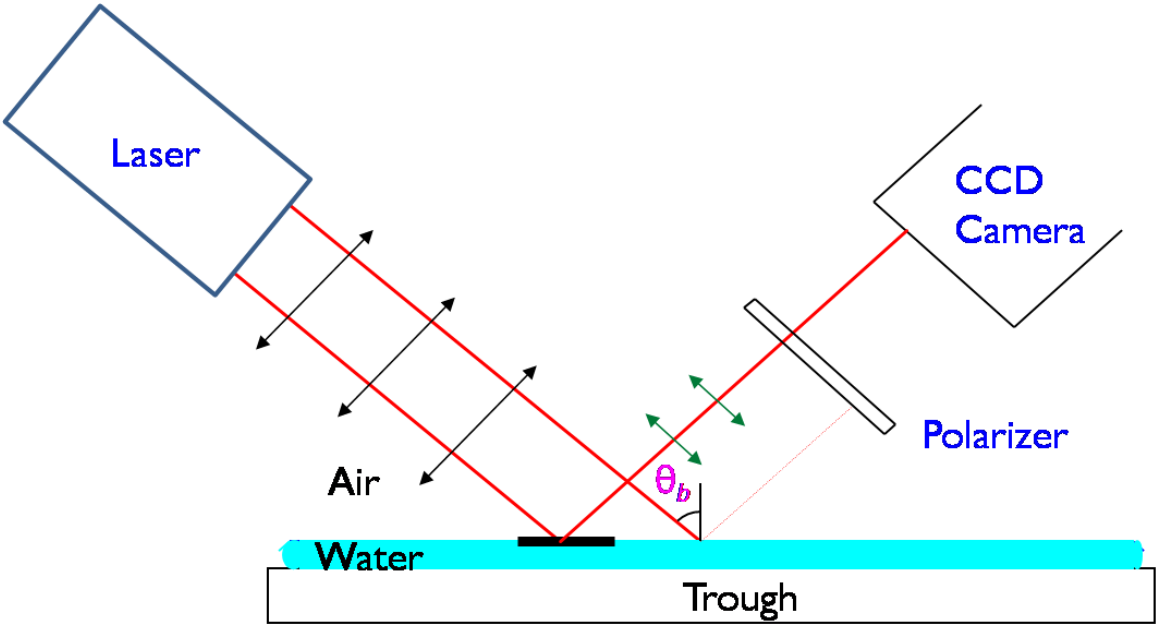

Figure 1.10: A schematic diagram showing the principle of a Brewster angle microscope. θ_b is the Brewster angle of water with respect to air. Black strip represents the monolayer domain and the light reflected from this region will have *p*-polarized component, which will be detected by the CCD camera. No light is reflected from the region having pure water surface, resulting in contrast between the regions with and without film.

1.4 Langmuir-Blodgett films

Langmuir monolayers can be transferred onto a solid substrate using the Langmuir-Blodgett (LB) technique [26]. The possibility of transferring these monolayers onto different solid substrates at the desired monolayer phase was first demonstrated by Katherine Burr Blodgett [27]. This method can be used to get thin films of highly oriented molecules. Here, a substrate is lowered vertically through a monolayer so that it dips into the subphase (water) and then withdrawn. During this process the film gets transferred onto the substrate. In order to maintain constant conditions during the process of transfer, the surface pressure is kept constant by compressing the monolayer between two moving barriers. Multiple layers of the film can be deposited by dipping substrates in many cycles. One dipping cycle consists of lowering of substrate (down stroke) and withdrawing of substrate (upstroke). The deposition of film on a substrate depends on the nature of substrates [28]. If the substrate has hydrophilic surface, one layer of the film is coated in first dipping cycle (during upstroke). In

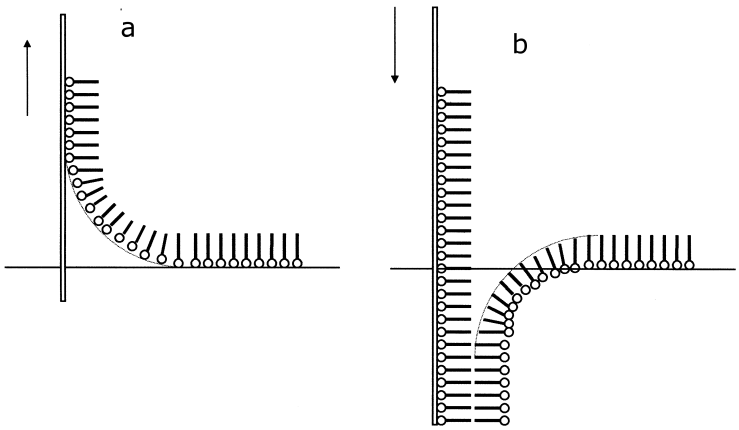

Figure 1.11: Schematic representation of the Langmuir-Blodgett (LB) deposition. (a) The monolayer film gets transferred onto the hydrophilic substrate during upstroke and (b) the second layer of the monolayer film gets transferred onto the substrate during the downstroke.

the subsequent dipping cycles two layers of the film will be transferred. If the substrate has hydrophobic surface, two layers of the film will be coated in one dipping cycle (one during downstroke and another during upstroke). In the downstroke, the molecules deposited will have their hydrophobic groups oriented towards the substrate. In the upstroke, the molecules deposited will have their polar groups oriented towards the substrate. During repeated dipping cycles, the polar groups of the new layer adheres to the polar groups of the previous layer during upstroke and the hydrophobic groups of the new layer stick to the hydrophobic groups of the previous layer during down stroke, in accordance with the expected behavior of amphiphilic molecules. Figure 1.11 shows the process of LB deposition.

There are many consequences of the molecular orientation dependence on the dipping direction [28]. The initial layer can be deposited during the upstroke only if the substrate surface is hydrophilic in nature, since the hydrophobic tails will prefer to attach to the substrate during the down stroke. Similarly, the first layer can be deposited during down stroke only if the substrate surface is hydrophobic in nature. However, the energetics of the amphiphilic interactions limits our ability to engineer required structures. Although monolayer

transfer generally occurs during both upstroke and down stroke (Y-type deposition), in few instances depending on the film-substrate interaction, deposition can also occur only during the down stroke (X-type) or only during upstroke (Z-type).

The efficiency of the LB transfer can be measured in terms of transfer ratio (τ). It is defined as the ratio of the decrease in Langmuir monolayer surface area during transfer to the total surface area of the substrate,

$$\tau = \frac{\text{Decrease in Langmuir monolayer surface area}}{\text{Total surface area of the substrate}} \tag{1.6}$$

According to a convention, a τ of unity is indicative of an ideal deposition. If the deposition process is ideal, then the molecules would have been simply transferred from the air-water interface to the solid substrate without any change in the film features. This may not be the case many times. Often during transfer, the film gets modified due to various reasons. LB transfer is a complicated process in which the amphiphiles generally attempt to reach a new thermodynamic minimum as they experience interactions with the solid substrate. If the density of the molecules change during the process of transfer, then $\tau = 1$ will not be indicator of a defect free film. In few cases like in the monolayers of fatty acid salts, the molecules on the water surface can be compressed into a nearly close packed state. During the LB transfer of such monolayers, the details of molecular packing may change but they still remain densely packed. In such cases, the difference in packing density before and after transfer will be a few percent at most, equivalent to the typical uncertainty of τ measurements.

LB films have been proposed for various commercial applications ranging from anti-reflection coating to soft X-ray monochromator. But they have never found their way to the market in a significant way. Nevertheless, the scientific interest in LB films remains strong even after more than 70 years because this technique offers a simple way to build supramolecular assemblies with well-defined molecular arrangement and orientation along with a good control over thickness. LB films are extremely useful in exploring fundamental interactions of amphiphilic molecules, chemical reactions in confined geometries and can

also be used as model biological systems.

1.4.1 Atomic force microscope

Scanning probe microscopes (SPM) like atomic force microscope, can be used to get the surface morphology and topography information with very high resolution. In SPM, an image is created by scanning the surface of sample with a sharp tip and measuring some highly localized tip-sample interaction as a function of position. In atomic force microscope (AFM), the force between the tip and the sample is measured as a function of position. In scanning tunneling microscope (STM), the tunneling current between the conducting tip and the sample is measured as a function of the position. Binnig *et al.* developed STM in 1981 at IBM Zurich Research Laboratory, Switzerland [29]. It was the first SPM capable of directly obtaining 3D images of solid surfaces with atomic resolution. Although the technique of measuring tunneling current gives topography and conductivity information of the surfaces, STM had a drawback that it can be used only for conducting surfaces. To overcome this, in 1985, Binnig *et al.* developed AFM to measure ultra-small forces ($< 1\ \mu$N) between the AFM tip and sample surface [30]. AFM do not require conducting substrate unlike in STM. This expands the use of SPM for all kinds of surfaces irrespective of their mechanical, optical and electrical properties. This makes AFM a versatile tool to carry out the studies in various fields including soft matter like biology. We have used commercial scanning probe microscope (model: Picoplus, Molecular Imaging) for all our AFM studies.

As mentioned in the previous paragraph, in AFM, the force between the tip and the sample is the source of image. AFM cantilevers and tips are usually made up of silicon or silicon nitride as it is easy to microfabricate these materials using established techniques. The radius of the tip on the cantilever is usually a few tens of nanometers. The force between the tip and the sample is calculated from the deflection of cantilever that occurs due to the tip-sample interaction. The deflection in the cantilever is given by Hooke's law, $F = -k_c z$, where F is the force between tip and sample, k_c is the stiffness of cantilever and z is the cantilever deflection. The deflection in cantilever is detected using an optical beam deflection method,

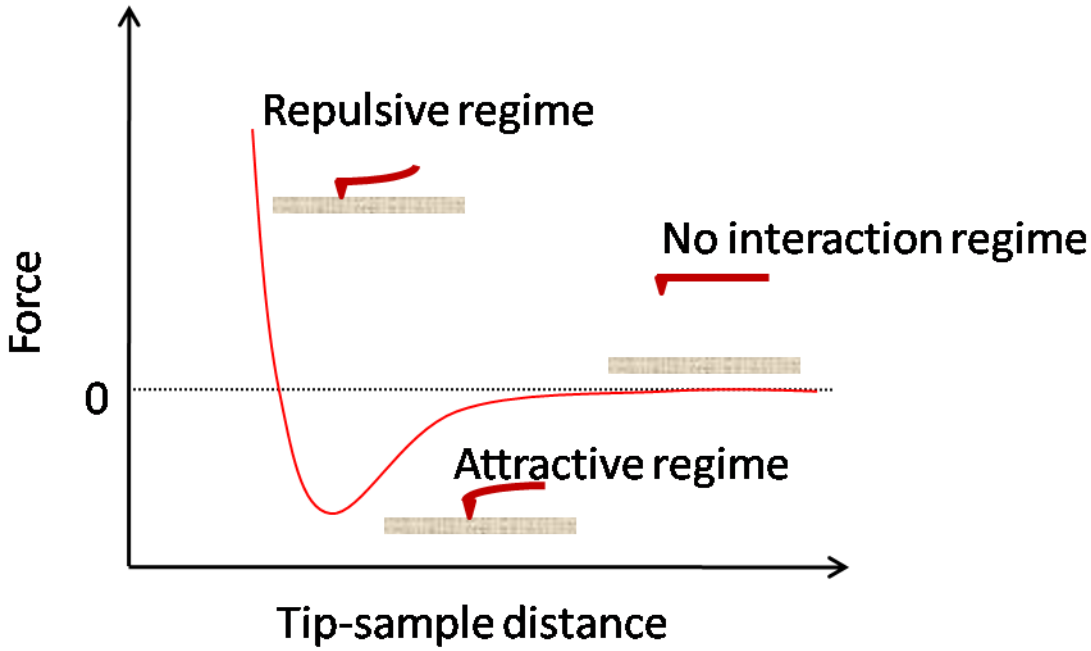

Figure 1.12: Typical variation of force versus tip-sample distance in an atomic force microscope. The different regimes with decreasing tip-sample distance are shown.

where a laser beam is reflected from the back of the cantilever onto a split photodiode detector. The sub-angstrom deflections can be detected and, therefore, forces of picoNewton can be measured. A more recently developed method to measure the cantilever deflection is through a piezoelectric layer on the cantilever, that registers a voltage upon deflection [31].

When the tip approaches the sample surface, it experiences various interaction forces. Figure 1.12 shows typical force versus tip-sample distance curve as tip approaches the sample surface. When the tip is far from the sample (more than 10 μm), the interaction between the tip and the sample is negligible and no cantilever deflection will be detected. The first interaction encountered by the tip as it approaches the sample is due to the damping air film. At this distance, air is squeezed between the tip and the sample surface during each down stroke of the tip. This pumping effect dampens the tip motion to some extent. The air film damping phenomenon is exclusive to the oscillating cantilevers; contact mode AFM and STM tips do not have this phenomenon. When the tip is at a distance of 1 – 0.1 nm from the sample surface, electrostatic forces become dominant. Electrostatic forces are either attractive or repulsive depending on the charge on the tip and sample. For distances 200 – 10 nm the tip

experiences the surface tension effects. This effect results from the presence of condensed water vapor on the sample surface. This is an attractive force, and can pull a tip down towards the sample surface and it is strong enough to indent soft materials. To overcome this problem oscillating cantilevers are employed. In order to image very delicate samples, the cantilever and the sample are entirely immersed in a liquid, so that the damage due to the surface tension effect is prevented. When the tip comes further close to the sample surface at a distance of few angstroms, van der Waals forces cause a weak attraction between the atoms in the tip and sample surface. On further bringing the tip closer to the surface, the tip experiences strong repulsion due to coulombic repulsion force. At this point the tip is in contact with the sample. The coulombic force arise from the overlap of the electron shells from atoms on the tip and sample. These forces are very strong and further intrusion of the tip into the sample is prevented. Forces greater than this will make mechanical distortion of sample or tip or both. Sometimes the tip may be permanently damaged [32].

Depending on the interaction between the tip and the sample like van der Waals attractive forces, electrostatic forces, magnetic forces, adhesion forces and frictional forces, many modes of AFM are developed to characterize various properties of a sample like electrical [33], mechanical [34] and chemical [35] properties, in addition to getting the topography image.

Contact mode AFM

In the contact mode AFM the tip is in contact with the sample. The interaction forces between the tip and sample causes the cantilever to deflect quasi-statically according to Hooke's law and this deflection is directly measured [36]. A feedback loop directly monitors the force between the tip and sample by adjusting the cantilever-sample distance. The Z-position of the cantilever attached to the piezo is changed to keep constant distance (and force) between the tip and sample. Figure 1.13 shows the schematic diagram of the contact mode AFM. Usually in the contact mode, the tip is very close to the sample surface and the interaction between them is due to repulsive forces. The spring constant of the cantilever used in the

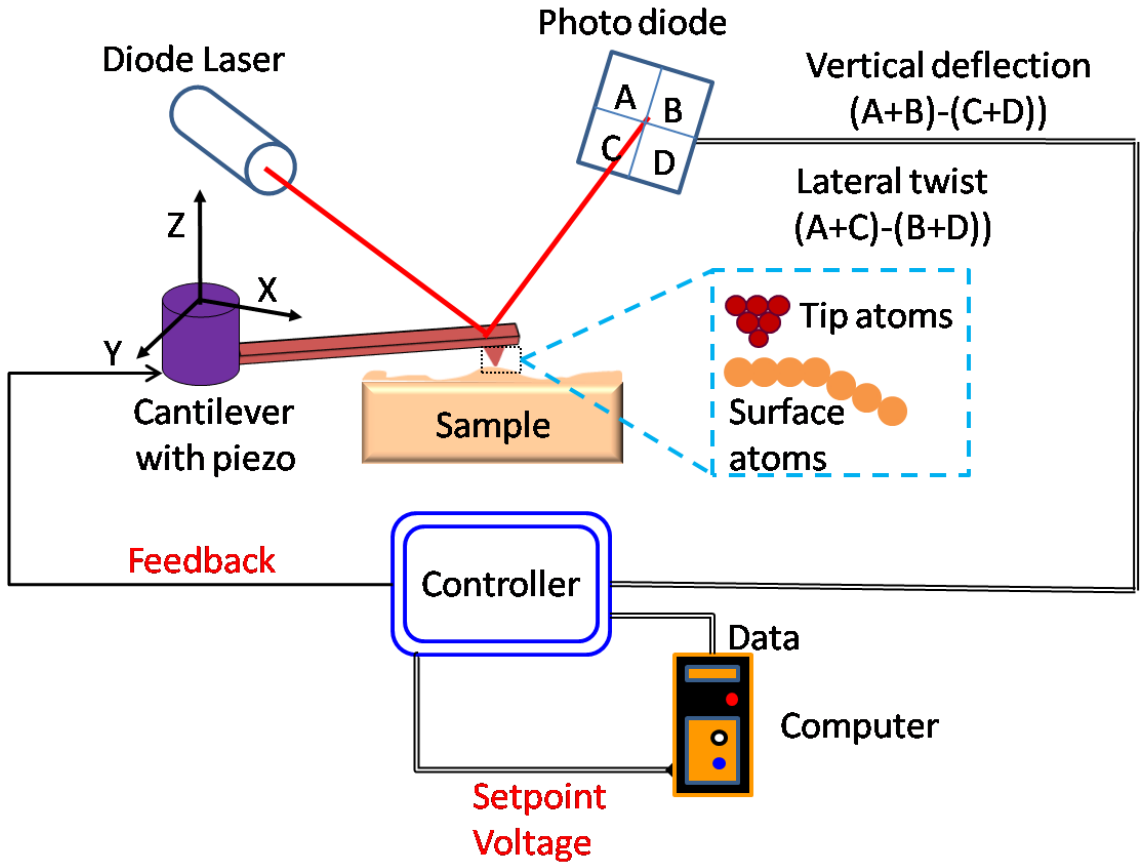

Figure 1.13: Schematic diagram of contact mode AFM.

contact mode AFM is less than < 1 N/m. The force gradient acting between the tip and sample is in the range $1 - 10$ nN/nm. The force has to be chosen appropriately by adjusting tip-sample distance to get good contrast in the image and reduce damage to the sample.

In addition to the topography image, contact mode AFM also gives the lateral forces between the tip and sample. The friction between the tip and sample during scanning results in torsional deflection of the cantilever. This deflection can be measured using laser beam deflection method. The lateral displacement of the laser beam reflected from the back of cantilever leads to the intensity difference of the laser beam received in the left hand and right hand sets of quadrants of photo diode detector. This can be used to measure the relative frictional force acting on the tip.

Capillary forces acting on the tip due to moisture condensation may lead to high noise levels. This can be eliminated by scanning the sample under liquid. Solvents like propanol and butanol are popular although greater understanding of ionic interactions has permitted the use of a wide range of solvents. Contact mode AFM is appropriate for scanning only the hard and flat surfaces because even under very low force conditions, it exerts a significant shear or lateral force on the sample. Hence this mode is not suitable for imaging sample which is dynamic or weakly attached to the substrate, as high lateral forces can damage the sample surface. These problems are overcome by using the AFM in non-contact mode as explained in the next section.

Non-contact mode AFM

In non-contact mode AFM, attractive forces which are of long range are used to monitor the tip-sample interaction. These attractive forces are weaker than the repulsive forces detected in the contact mode and hence different techniques are required to utilize them [36]. In the non-contact mode AFM, the cantilever is deliberately excited by an electrical oscillator (see Figure 1.14). As the cantilever approaches the sample surface, the tip-sample interaction reduces the amplitude of cantilever oscillation. The amplitude of the oscillations can be kept constant at a fixed cantilever-sample distance. The sample surface is scanned at constant

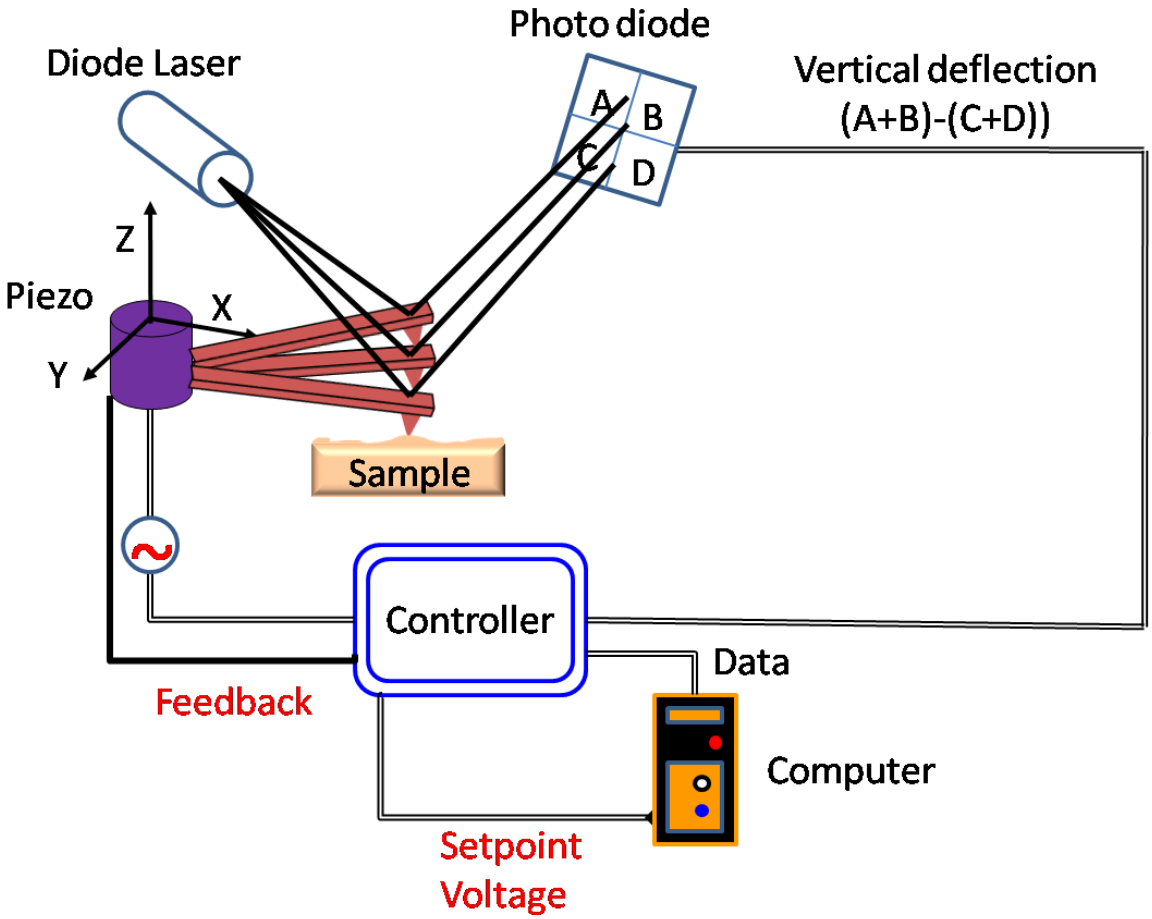

Figure 1.14: Schematic diagram of non-contact mode AFM.

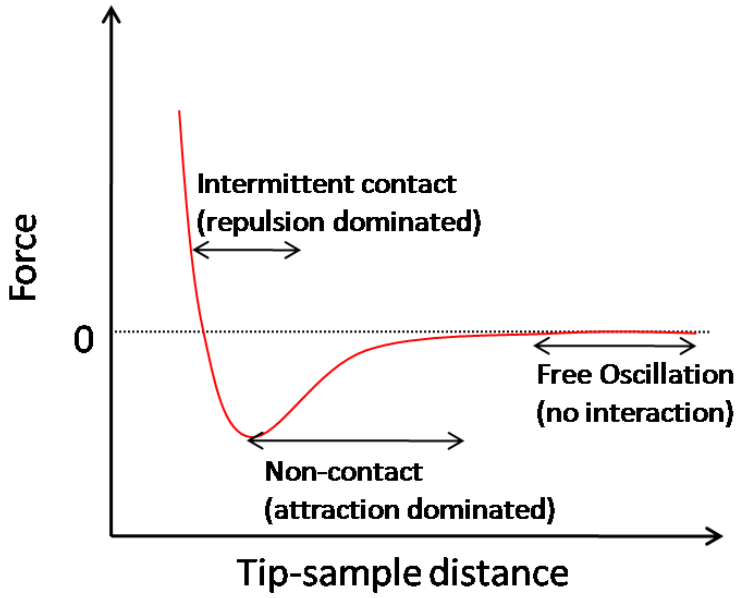

Figure 1.15: Typical force versus tip-sample distance curve in an atomic force microscope.

amplitude using a feedback loop. The change in the Z-position of the cantilever to keep the amplitude at the fixed value gives the topography information. In addition to this, the phase difference between the oscillation of cantilever and external electrical oscillator can be used to differentiate areas on the sample surface with different stiffness, adhesion and viscoelasticity. There are two main types of non-contact mode AFM: First is the intermittent contact mode AFM and second is the true non-contact mode AFM.

In the intermittent contact (or tapping) mode AFM, the tip bounces up and down (taps) as it scans over the sample surface with amplitude of about 100 nm. In this mode, the interaction between the tip and sample is dominated by the repulsive forces (see Figure 1.15), which dampens the cantilever oscillations. Intermittent contact mode reduces the lateral force on the sample because the tip spends less time ($\sim 10^{-7}$ s) on the sample surface. Hence delicate samples such as networks of molecules can be imaged without severe distortion.

In true non-contact mode AFM, the oscillating tip never touches the sample surface. It hovers few nanometers above the surface with an oscillation amplitude of only about 5 nm. The relatively long range van der Waals attractive forces between tip and sample produces a dampening effect on the oscillating cantilever. So when the separation between the AFM

tip and sample is reduced, the amplitude of the cantilever oscillation falls. This effect is used by the instrument software at each image point to detect and construct the topography of the surface. In this mode of AFM there is least or no deformation and shear on the sample surface. Hence it is a suitable mode of scanning LB films to get high contrast images, although other modes are also occasionally used.

1.4.2 Current sensing atomic force microscope

Current sensing AFM (CSAFM) allows detailed analysis of the nanoscale electrical conductivity of sample on a conducting substrate, along with the topography analysis of the sample surface. Here the cantilever and the tip are coated with a conducting material like platinum or gold. The tip is scanned over the sample surface in contact mode [37]. By applying a voltage bias between the substrate and conducting tip, a current flow is generated. This current is used to construct a spatially resolved conductivity image. The simultaneously obtained topography and current images enable us to correlate the surface topographical features with the electrical conductivity properties. In addition to this, one can also get current(I)−voltage(V) characteristics of the sample by holding the tip in contact with the sample surface and applying a voltage ramp between tip and substrate.

In our CSAFM setup (Molecular Imaging), the tip was kept at a virtual ground and bias voltage was applied to the substrate. Figure 1.16 shows the schematic diagram of our experimental setup. By selecting an appropriate value for the force between the tip and sample, the surface is scanned by maintaining constant tip-sample force. This is crucial as the amplitude of the current signal obtained from the CSAFM is strongly dependent on the force applied to the surface. The current signal from the cantilever is collected by a pre-amplifier of sensitivity 1 nA/V. The operational range of the pre-amplifier used was from 1 pA to 10 nA.

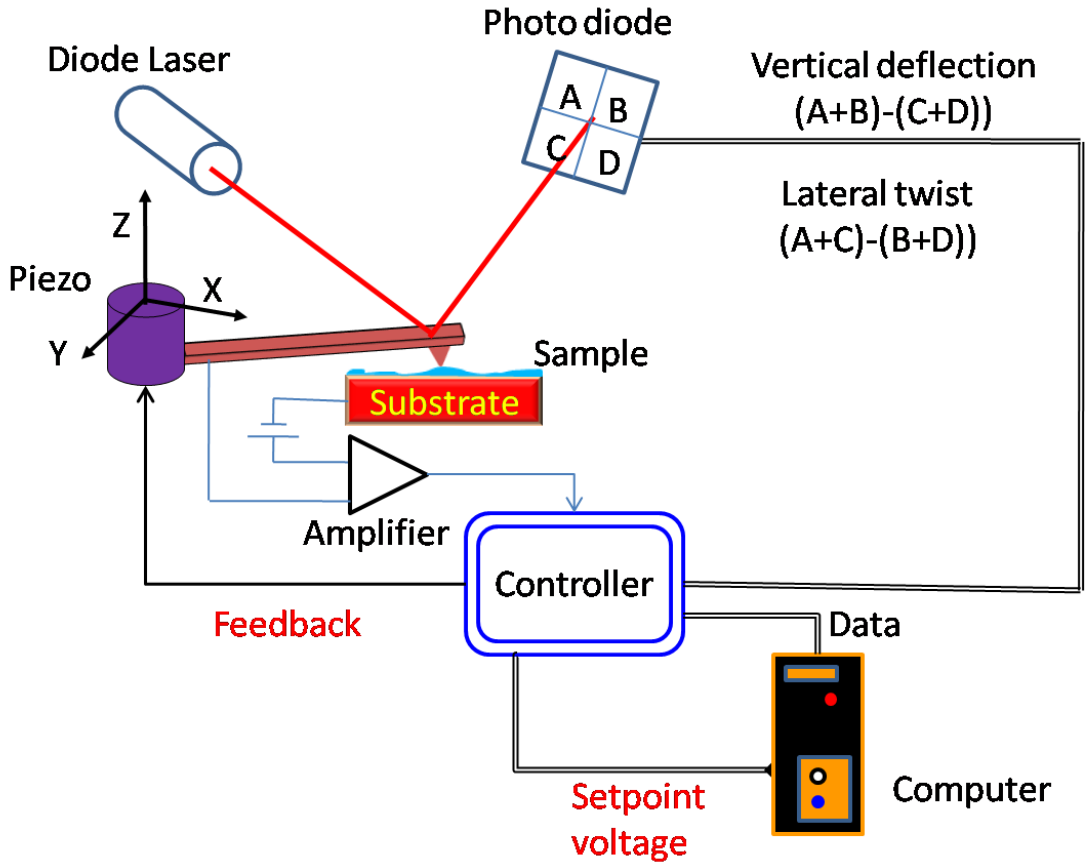

Figure 1.16: Schematic diagram of current sensing AFM setup.

Bibliography

[1] G. L. Gaines Jr., *Insoluble Monolayers at Liquid Gas Interface*, Interscience: New York, (1966).

[2] K. S. Birdi, *Lipid and Biopolymer Monolayers at Liquid Interfaces*, Plenum Press: New York, (1989).

[3] M. L. Longo, A. M. Bisagno, J. A. N. Zasadzinski, R. Bruni, and A. J. Waring, *Science* **261**, 453 (1993).

[4] P. G. de Gennes, and J. Prost, *The Physics of Liquid Crystals*, Oxford University Press: UK, Second edition (2001).

[5] P. J. Collings, and M. Hird, *Introduction to Liquid Crystals: Chemistry and Physics*, Taylor and Francis: London, (1997).

[6] W. M. Gelbart, A. Ben-Shaul, and D. Roux, *Micelles, Membranes, Micro-emulsions, Monolayers*, Springer-Verlag: New York, (1994).

[7] S. Chandrasekhar, B. K. Sadashiva, and K. A. Suresh, *Pramana* **9**, 471 (1977).

[8] Sandeep Kumar, *Chem. Soc. Rev.* **35**, 83 (2006).

[9] Sandeep Kumar, *Liquid Crystals* **36**, 607 (2009).

[10] S. Sergeyev, W. Pisula, and Y. H. Geerts, *Chem. Soc. Rev.* **36**, 1902 (2007).

[11] Sandeep Kumar, and S. K. Varshney, *Angew. Chem. Int. Ed.* **39**, 3140 (2000).

[12] V. M. Kaganer, H. Mohwald, and P. Dutta, *Rev. Mod. Phys.* **71**, 779 (1999).

[13] M. M. Lipp, K. Y. C. Lee, J. A. Zasadzinski, and A. J. Waring, *Science* **273**, 1196 (1996).

[14] J. T. Davies, and E. K. Rideal, *Interfacial Phenomena*, Academic Press: New York, (1961).

[15] B. Lin, M. C. Shih, T. M. Bohanon, G. E. Ice, and P. Dutta, *Phys. Rev. Lett.* **65**, 191 (1990).

[16] D. K. Schwartz, M. L. Schlossman, and P. S. Pershan, *J. Chem. Phys.* **96**, 2356 (1992).

[17] I. R. Peterson, R. M. Kenn, A. Goudot, P. Fontaine, F. Rondelez, W. G. Bouwman, and K. Kjaer, *Phys. Rev. E* **53**, 667 (1996).

[18] M. C. Shih, T. M. Bohanon, J. M. Mikrut, P. Zschack, and P. Dutta, *Phys. Rev. A* **45**, 5734 (1992).

[19] P. Tippmann-Kyayer, and H. Mohwald, *Langmuir* **7**, 2303 (1991).

[20] T. M. Bohanon, B. Lin, M. C. Shih, G. E. Ice, and P. Dutta, *Annu. Rev. Phys. Chem.* **41**, 4846 (1990).

[21] R. D. Smith, and J. C. Berg, *J. Colloid Interface Sci.* **74**, 273 (1980).

[22] G. A. Overbeck, D. Honig, and D. Mobius, *Langmuir* **9**, 555 (1993).

[23] E. Teer, C. M. Knobler, S. Siegel, D. Vollhardt, and G. Brezesinski, *J. Phys. Chem. B* **104**, 10053 (2000).

[24] S. Henon, and J. Meunier, *Rev. Sci. Instrum.* **62**, 936 (1991).

[25] D. Honig, and D. Mobius, *J. Phys. Chem.* **95**, 4590 (1991).

[26] D. K. Schwartz, *Surf. Sci. Rep.* **27**, 241 (1997).

[27] K. B. Blodgett, *J. Am. Chem. Soc.* **57**, 1007 (1935).

[28] G. Roberts, *Langmuir-Blodgett Films*, Plenum Press: New York, (1990).

[29] G. Binnig, H. Rohrer, Ch. Gerber, and E. Weibel, *Phys. Rev. Lett.* **49**, 57 (1982).

[30] G. Binnig, C. F. Quate, and Ch. Gerber, *Phys. Rev. Lett.* **56**, 930 (1986).

[31] R. Linnemann, T. Gotszalk, I. W. Rangelow, P. Dumania, and E. Oesterschulze, *J. Vac. Sci. Technol. B* **14**, 856 (1996).

[32] B. Cappella, and G. Dietler, *Surface Science Reports* **34**, 1 (1999).

[33] C. Ionescu-Zanetti, A. Mechler, S. A. Carter, and R. Lal, *Adv. Mater.* **16**, 385 (2004).

[34] E. W. Wong, P. E. Sheehan, and C. M. Lieber, *Science* **277**, 1971 (1997).

[35] Y. Sugimoto, P. Pou, M. Abe, P. Jelinek, R. Perez, S. Morita, and O. Custance, *Nature* **446**, 64 (2007).

[36] V. J. Morris, A. R. Kirby, and A. P. Gunning, *Atomic Force Microscopy for Biologists*, Imperial College Press: London, (1999).

[37] D. J. Wold, and C. D. Frisbie, *J. Am. Chem. Soc.* **122**, 2970 (2000).

Chapter 2

Langmuir monolayer and Langmuir-Blodgett films of a novel mesogenic H-shaped azobenzene dimer

2.1 Introduction

The study of monolayer films of molecules with different shapes is of interest to understand the packing of molecules based on their structure and intermolecular interactions at air-water interface [1, 2]. These films can be transferred onto solid substrates for studying the physical properties which are important for some device applications. Stable and defect free films are required for many technological applications, while controlled wetting and dewetting processes are important for producing thin film micro-structuring for microelectronics, optical devices and bio-chip technology [3]. Wetting of films on a substrate depends on factors like the surface treatment given to the substrate and the nature of the material in the film. Molecules with different architecture have been used to study such properties. Among them azobenzene molecules are of special interest as photoisomerization reaction can bring in-situ changes in the molecular architecture resulting in interesting behavior [4]. Additionally, the molecules with azobenzene group find application in photomechanical devices [5]. Liquid crystals containing azobenzene group are promising materials for devices involving pho-

tomechanics [6], optical switching and image storing because of their high resolution and sensitivity [7].

In this chapter, we present the studies on the monolayer properties of a novel H-shaped mesogenic azobenzene dimer, Bis[5-(4'-n-dodecyloxy benzoyloxy)-2-(4"-methylphenylazo)phenyl] adipate (12D1H) at air-water and air-solid interfaces. The monolayer at air-water interface was studied using the techniques of surface manometry and Brewster angle microscopy (BAM). The film was transferred onto hydrophilic and hydrophobic solid substrates by Langmuir-Blodgett (LB) technique. The wetting behavior of the LB film on the solid substrates was studied using atomic force microscopy (AFM). The film transferred onto hydrophobic silicon substrate dewetts to yield nano-droplets. Our analysis of AFM images indicated that the dewetting of the film to form nano-droplets was through the mechanism of spinodal dewetting.

2.2 Experiment

The material 12D1H was synthesised by Prajapati and Varia [8]. It was purified by column chromatography over silica gel and recrystallized from ethanol. The material was characterized by infrared, ultraviolet (UV) - visible and NMR spectroscopy. The purity of the sample was found to be better than 99.9%. Figure 2.1 shows the chemical structure of 12D1H molecule. The azobenzene groups in the molecule makes it photosensitive. The UV-visible spectroscopy studies of the material in chloroform showed absorption peaks which causes the transition from *trans* to *cis* state and vice versa. Liquid crystalline properties were investigated using a Leitz Laborlux 12 POL microscope equipped with a Mettler FP82HT hot stage.

Films of 12D1H were studied at air-water and air-solid interfaces using techniques of surface manometry, BAM and AFM. The surface manometry studies were carried out using Nima trough (Model: 611M). The trough was enclosed in an aluminum box to prevent ambient light, air drag and contaminants. Ultra-pure deionized water (millipore water, MilliQ)

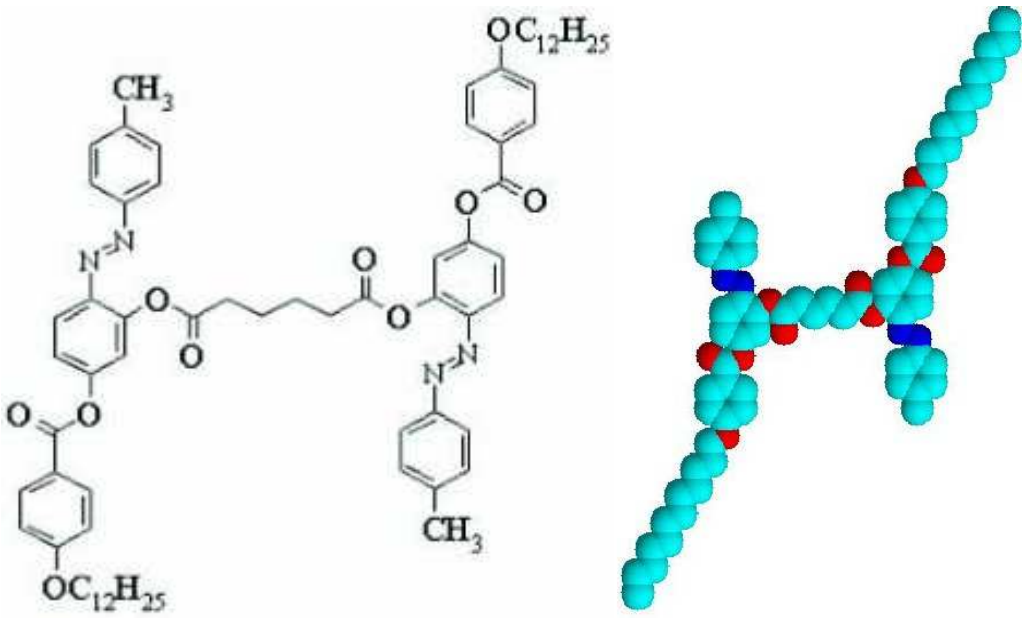

Figure 2.1: Chemical structure of 12D1H molecule (left). Space filling model of the 12D1H molecule (right).

was used as subphase. Dilute solution of 12D1H prepared in HPLC grade chloroform (concentration = 0.125 mg/ml) was spread at air-water interface using a micro syringe (Hamilton) to form a monolayer. The temperature of $24.0 \pm 0.1^{\circ}C$ was maintained by circulating water in the trough using a temperature controller (Model: F25, Julabo). The monolayer was compressed at the rate of about 0.14 $nm^2 molecule^{-1} min^{-1}$. Wilhelmy method was used to measure the surface pressure. BAM studies were carried out using a MiniBAM (NFT, Nanotech).

For studies on the monolayer of 12D1H molecules which are photosensitive, care was taken to minimize the effect of ambient light. Since it is known that UV light induces a *trans* to *cis* transition in the azobenzene group, the solution of 12D1H was stored in dark (absence of ambient light) for more than 12 hours [9], before forming the monolayer. The experiments were carried out by placing the Nima trough in the aluminum box in the dark room to study the *trans*-12D1H monolayer.

The LB films of 12D1H were prepared by transferring the monolayer on two different substrates, (a) freshly cleaved mica and (b) 1,1,1,3,3,3 hexamethyldisilazane (HMDS) coated silicon. HMDS coated silicon substrate was prepared by using the following procedure [10].

Polished silicon wafers were treated with boiling piranha solution (3:1 ratio of H_2SO_4 and H_2O_2) for about five minutes. Then the wafers were thoroughly cleaned by rinsing in ultrapure water. The dried wafers were then rinsed with chloroform before keeping them in the HMDS solution in chloroform for about 12 hours. Self assembled monolayer of HMDS formed on the silicon surface makes the substrate hydrophobic. The surface is then repeatedly rinsed with chloroform to remove the free sticking molecules of HMDS. Finally before using the substrate for transferring the LB film the substrate is cleaned with ultrapure water.

The transfer of the monolayer of 12D1H in the *trans* state was carried out by LB technique at a surface pressure of 1 mN/m with a dipping speed of 2 mm/min. One layer of the film gets transferred onto the hydrophilic mica substrate in one dipping cycle (consisting of one down-stroke and one upstroke). The transfer of the film occurred during the upstroke. For HMDS coated silicon which is hydrophobic substrate, two layers of the film get transferred in one dipping cycle. The transfer occurred both during the down-stroke and upstroke of the substrate. We find that both on freshly cleaved mica and on HMDS coated silicon, the transfer ratio was better than 0.85. The LB films were characterized by AFM (Model: PicoPlus, Molecular Imaging) in the acoustic AC mode (intermittent contact mode). The spring constant of the cantilever used was 31 N/m.

2.3 Results

The material 12D1H was studied under the polarizing microscope. On cooling from the isotropic state, the sample transformed to a mesophase at 51°C. Under the crossed polarizers the mesophase showed schlieren texture which is characteristic of the smectic C (SmC) phase. On further cooling, the material transformed to a crystalline state at 45°C. Differential scanning calorimetry (DSC) studies were also carried out to confirm the isotropic to SmC transition temperature (Figure 2.2). On heating the sample, the crystalline phase melted to the isotropic phase at about 85°C. On cooling the sample from the isotropic phase the DSC trace showed a peak at about 51°C corresponding to the transition from isotropic to SmC

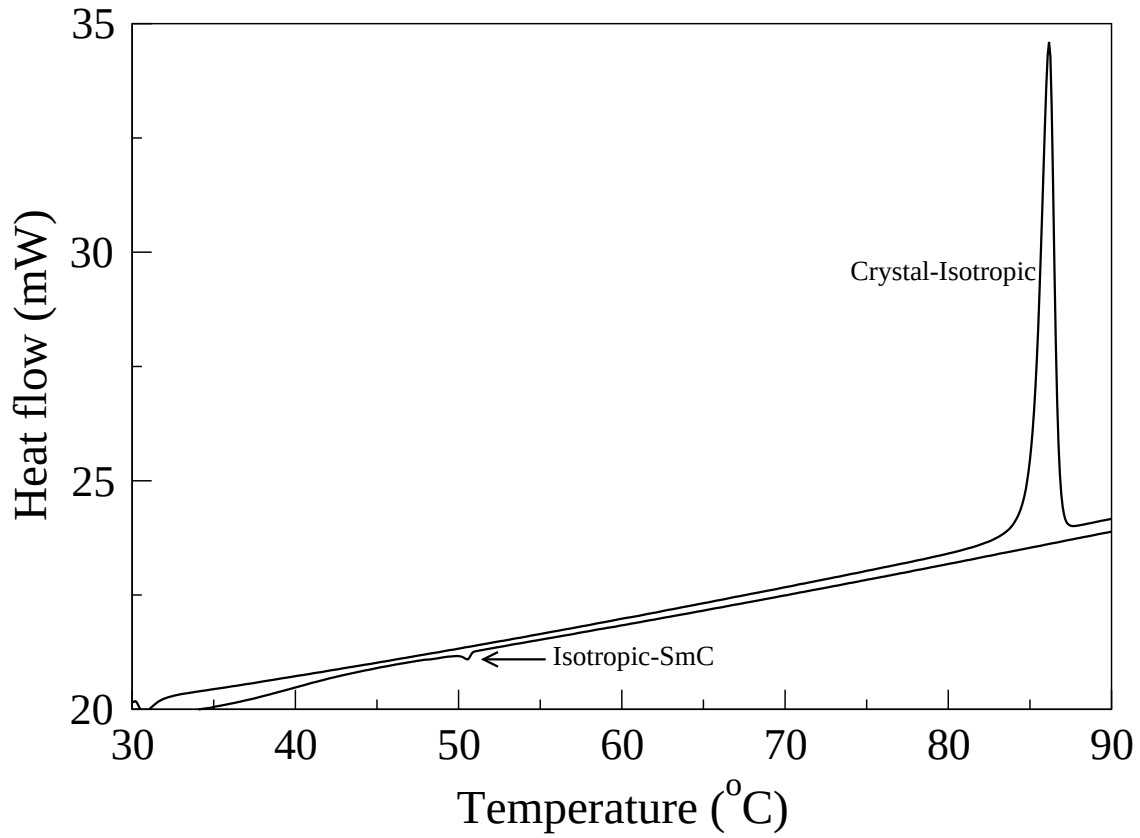

Figure 2.2: Variation of heat flow as function of temperature obtained from the differential scanning calorimetry study of the material 12D1H, showing the phase transitions.

phase.

2.3.1 Surface manometry

Surface pressure (π)−area per molecule (A_m) isotherm of the monolayer in the dark (*trans*-12D1H) is shown in Figure 2.3. At large A_m the isotherm shows zero surface pressure. At A_m of about 2.50 nm^2, the surface pressure starts increasing. There is a steep rise in the surface pressure at A_m of 2.10 nm^2. The monolayer collapsed at an A_m of 1.84 nm^2 with a collapse pressure of 1.8 mN/m. The limiting area measured from the isotherm was found to be about 2.01 nm^2. On further compression after collapse, there was a gradual increase in the surface pressure. The stability of the monolayer was checked by holding the barriers at constant A_m and monitoring the change in the surface pressure as a function of time. It was found that above the A_m of 1.84 nm^2 surface pressure did not vary with time. This indicates that the

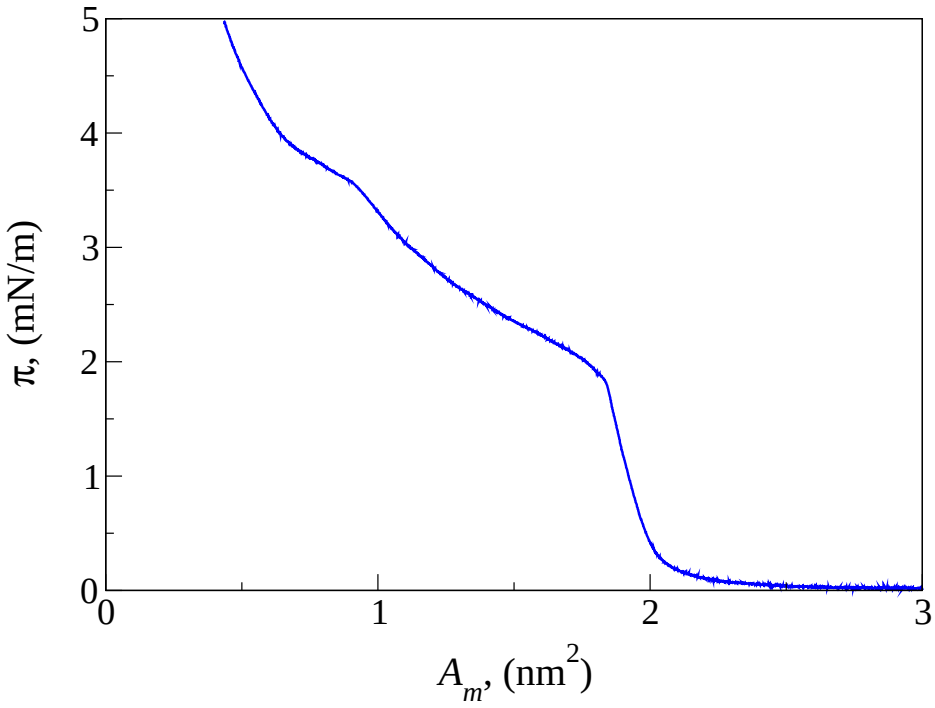

Figure 2.3: Figure shows the surface pressure (π)−area per molecule (A_m) isotherm for the 12D1H monolayer in dark, compressed with constant barrier speed.

monolayer was stable for A_m greater than 1.84 nm^2.

2.3.2 Brewster angle microscopy

The monolayer film at air-water interface was studied using BAM during compression. Figure 2.4 shows the BAM images of the monolayer in dark for different values of A_m. At large A_m, coexistence of dark and bright regions (with smooth phase boundary) was observed (Figure 2.4(a)). On compression, the monolayer forms an uniform bright phase (Figure 2.4(b)). On further compression, in the collapsed region, BAM images showed three dimensional (3*D*) crystallites (Figure 2.4(c)).

2.3.3 Atomic force microscopy

The LB films transferred at a surface pressure of 1 mN/m onto the hydrophilic mica and hydrophobic HMDS coated silicon substrates were studied using AFM in the acoustic AC mode. The bare substrates were also studied by the AFM. Figure 2.5 shows the topography

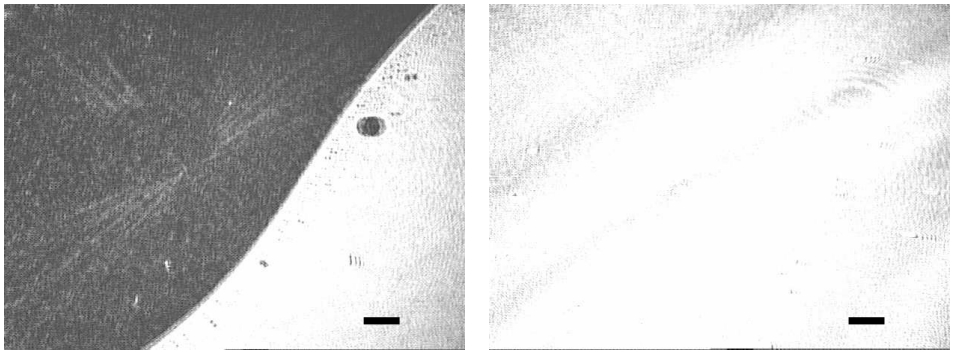

(a) 2.52 nm^2 (b) 1.91 nm^2

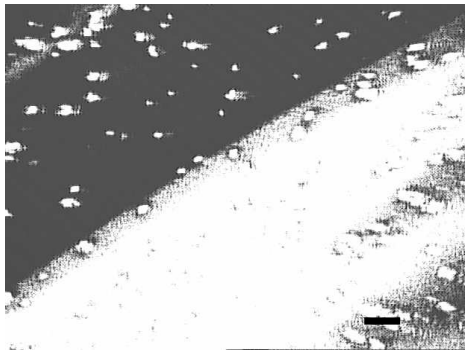

(c) 0.91 nm^2

Figure 2.4: Brewster angle microscope images of the 12D1H monolayer in dark for various area per molecule at air-water interface obtained on compressing the monolayer. (a) Shows coexistence of gas phase (dark region) and low density liquid phase (bright region) at A_m = 2.52 nm^2. (b) Shows the uniform low density liquid phase at A_m= 1.91 nm^2. (c) Shows the collapsed state with 3*D* crystallites (bright spots) at A_m = 0.91 nm^2. The scale bar in each image represents 500 μm.

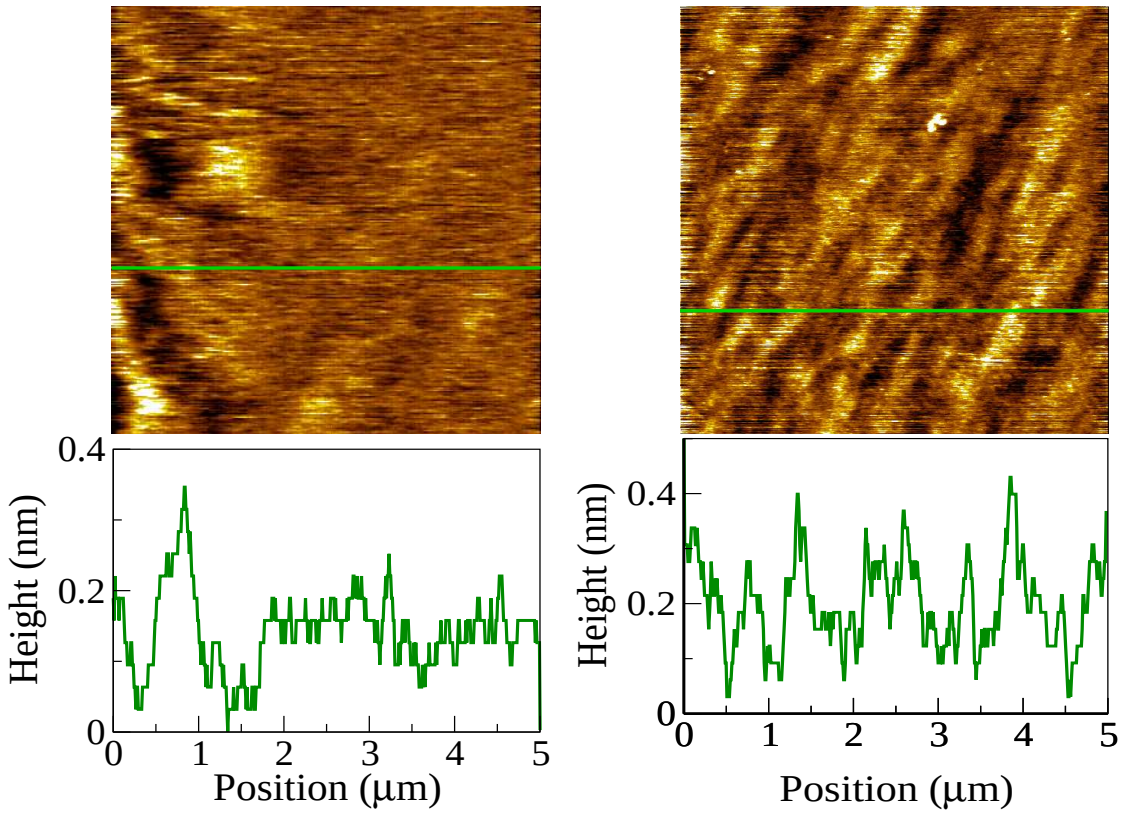

(a) Bare mica

(b) Bare HMDS coated silicon

Figure 2.5: AFM images of the bare substrates. (a) Shows the topography image of bare hydrophilic mica substrate. The line profile yields a RMS roughness of the substrate to be about 0.15 nm over the scan range of 5 μm X 5 μm. (b) Shows the topography image of the bare hydrophobic HMDS coated silicon substrate. The line profile yields the RMS roughness of the substrate to be about 0.18 nm over the scan range of 5 μm X 5 μm.

images of the bare substrates of hydrophilic mica and hydrophobic HMDS coated silicon. The line profile on the topography image of the bare mica substrate yielded a RMS roughness of about 0.15 nm. The AFM topography image of the 12D1H film on hydrophilic mica substrate transferred by the LB technique is shown in Figure 2.6. The line profile across the domains yielded the height of 3.8 nm.

In the case of HMDS coated silicon which behaves as a hydrophobic substrate, two layers of the film get transferred in one dipping cycle, that is when the substrate was dipped and taken out of the subphase. The AFM topography image of the LB film is shown in Figure 2.7. The image shows large domain coexisting with small uniform droplets (Figure 2.7(a)). Figure 2.7(b) shows the small droplets and Figure 2.7(c) shows a large domain

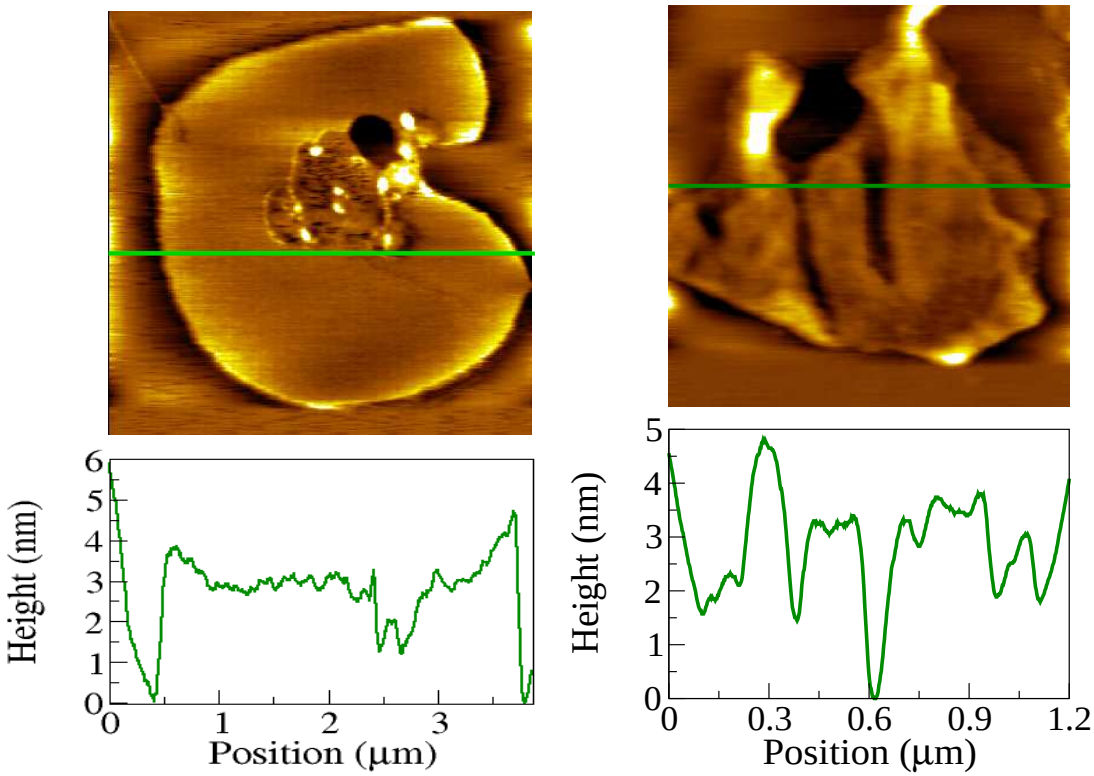

(a) (b)

Figure 2.6: AFM image of 12D1H monolayer on hydrophilic mica substrate. Here the film was transferred at a surface pressure of 1.0 mN/m. (a) Shows the domain size of about 3 μm and (b) shows the domain size of about 1 μm. The line profile on the domains yields an average height of 3.8 nm.

at higher magnification. The height of the large domain obtained from the line profile was 7.6 nm. The height of the small droplets varied between 10 nm to 50 nm with an average size of about 100 nm (Figure 2.7(b)).

2.4 Discussion

Surface manometry studies showed that the material 12D1H forms stable monolayer at an air-water interface for A_m greater than 1.84 nm^2. The uniform phase corresponding to the steep increase in the surface pressure (between 2.10 – 1.84 nm^2) can be characterized by the compressional modulus ($|E|$). The values of $|E|$ can be calculated from the $\pi - A_m$ isotherm using equation,

$$|E| = A_m \left(\frac{\mathrm{d}\pi}{\mathrm{d}A_m} \right) \tag{2.1}$$

Here, $\left(\frac{\mathrm{d}\pi}{\mathrm{d}A_m}\right)$ is the rate of change of surface pressure as a function of area per molecule. Figure 2.8 shows the variation of $|E|$ as a function of A_m for the 12D1H monolayer in dark (absence of ambient light). The maximum value of $|E|$ is about 22 mN/m at 1.87 nm^2. According to the criteria given in the literature [11, 12], the monolayer with maximum $|E|$ value between 12.5 mN/m to 50 mN/m corresponds to the low density liquid (L_1) or liquid expanded phase. From the $\pi - A_m$ isotherm, $|E|$ value and BAM images, we infer that the monolayer exhibited the coexistence of gas and low density liquid phase at high A_m. On compression, the monolayer transformed into uniform L_1 phase at A_m of 2.1 nm^2 before collapsing at 1.84 nm^2 with a collapse pressure of 1.8 mN/m. The small collapse pressure can be attributed to the absence of strong polar group and weak chain-chain interactions. The limiting area of 2.01 nm^2 corresponds to the estimated area per molecule (using Chemdraw 3D) where the two ester groups of the molecule are in contact with water and the alkyl chains and azobenzene group are protruded into air (Figure 2.9). Here, the molecules have the freedom to orient their aliphatic chains in different directions. This is similar to the monolayers of fatty acids with carbon-carbon double bond in the aliphatic chain. The carbon-carbon double bond will disturb the packing of the molecules which leads to a more expanded

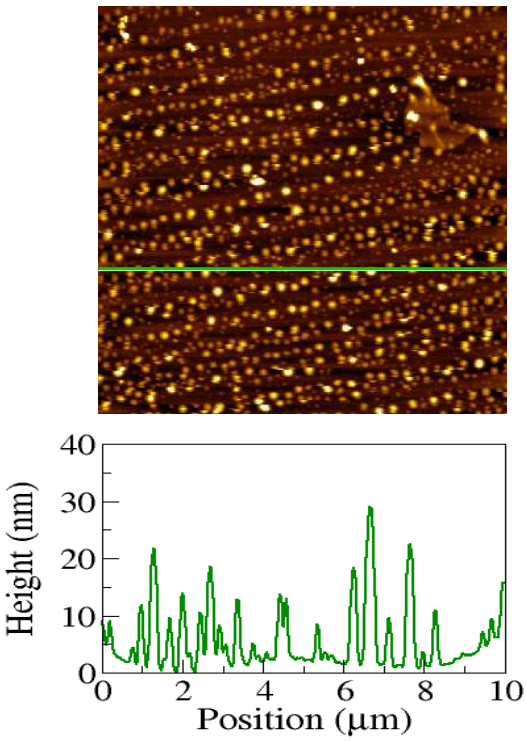

(a) Coexistence of domain and droplets

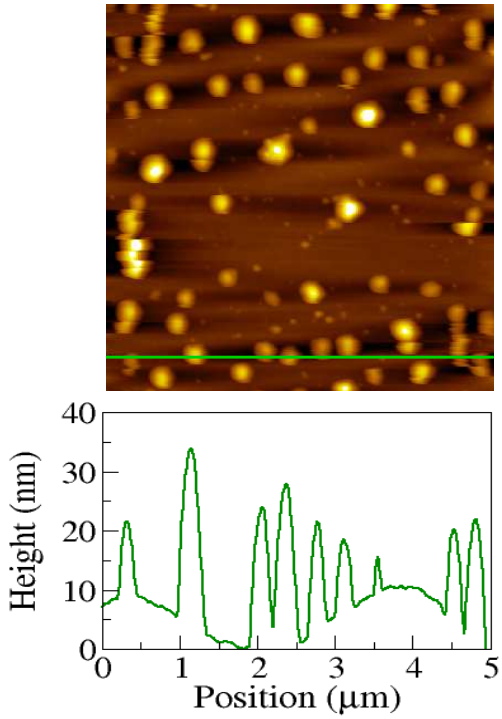

(b) Droplets of various height

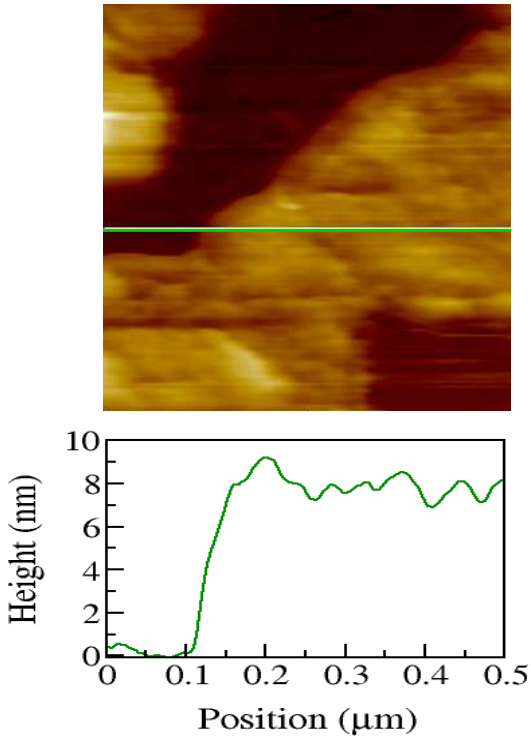

(c) Bilayer domain

Figure 2.7: AFM images of 12D1H transferred at 1.0 mN/m on to hydrophobic silicon substrate. (a) 10 μm scan range image showing the coexistence of droplets of uniform size and a bilayer domain (top right). (b) 5 μm scan range image showing droplets of about 100 nm size with height distribution of 10 nm to 50 nm. (c) 500 nm scan range image showing bilayer film with a height of 7.6 nm.

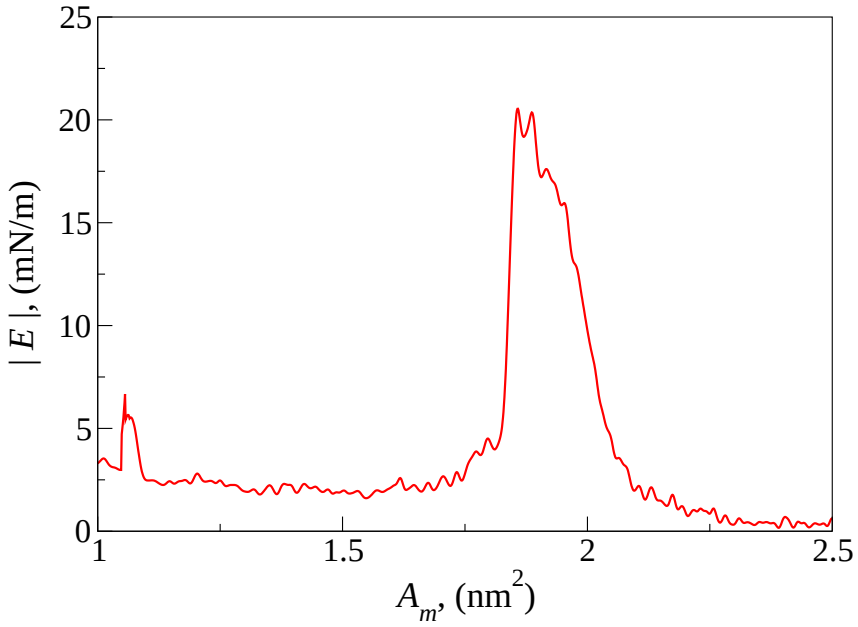

Figure 2.8: Figure shows the variation of compressional modulus ($|E|$) as function of area per molecule (A_m) for the 12D1H monolayer in dark.

phase [2].

The AFM images of the monolayer film transferred onto a hydrophilic mica substrate showed domains of height 3.8 nm (Figure 2.6). The film was transferred at a surface pressure of 1 mN/m. The height obtained from the topography image corresponds to the estimated height of the molecule when the two ester groups are in contact with the hydrophilic mica surface and the alkyl chains and azobenzene group are protruded into air. This indicates that the organization of molecules on the mica substrate is similar to that at the air-water interface. The changes in the orientation of aliphatic chains in the molecules at interfaces as compared to their bulk conformation, have been reported in the monolayers of other odd shaped molecules like bent core molecules [13].

The AFM studies of the film transferred onto the HMDS coated silicon substrate showed large domain coexisting with the small droplets. The height of the large domains was about 7.6 nm which corresponds to the bilayer film. The height of the droplets varied between 10 nm to 50 nm. Figure 2.10 shows the 3D view of the AFM topography image of the small droplets on the hydrophobic silicon substrate and the corresponding Abbot curve. Abbot curve gives the height distribution of the droplets on the surface of the hydrophobic silicon

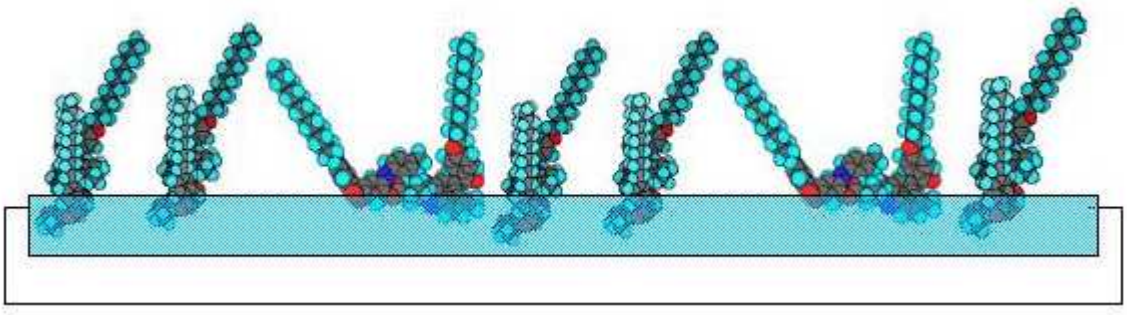

Figure 2.9: Schematic representation of the arrangement of molecules at air-water interface. This is based on the limiting area of 2.01 nm^2 obtained from $\pi - A_m$ isotherm and the height of 3.8 nm obtained from the AFM image of the monolayer film on hydrophilic mica substrate. Here the ester groups of the molecule are in contact with water surface and the alkyl chains are protruded into air.

substrate. It can be seen that some of the droplets have a height upto 50 nm.

From these images we conclude that the bilayer film, transferred on to the hydrophobic silicon substrate, dewetted to form smaller droplets of larger height. The direction in which the droplets are aligned appear to be along the small groove like features which are usually present on the hydrophobic silicon substrates (Figure 2.5(b)). Formation of such small droplets was not observed in the case of film on mica substrates. Recently Hashimoto and Karthaus have reported micrometer size droplets formed by dewetting [14]. They demonstrated that by adjusting the thickness of the film the diameter and height of the droplets can be controlled.

We attribute the formation of nano-droplets to the post transfer reorganization of the film. For a thin liquid film on a non-wettable solid substrate, the film will be unstable [15] and it may rupture. So the formation of droplets is likely due to the dewetting of the bilayer film of 12D1H on hydrophobic silicon. The unstable film on a rough solid substrate can rupture with two possible mechanisms; (i) spinodal dewetting and (ii) dewetting due to substrate roughness. In the case of spinodal dewetting the unstable film on a solid substrate develops surface fluctuations of various wavelengths. Fluctuations with wavelengths greater than the critical wavelength (λ_c) are amplified in the field of repulsive interaction between the film and the non wettable surface at the expense of fluctuations with wavelengths smaller than the critical

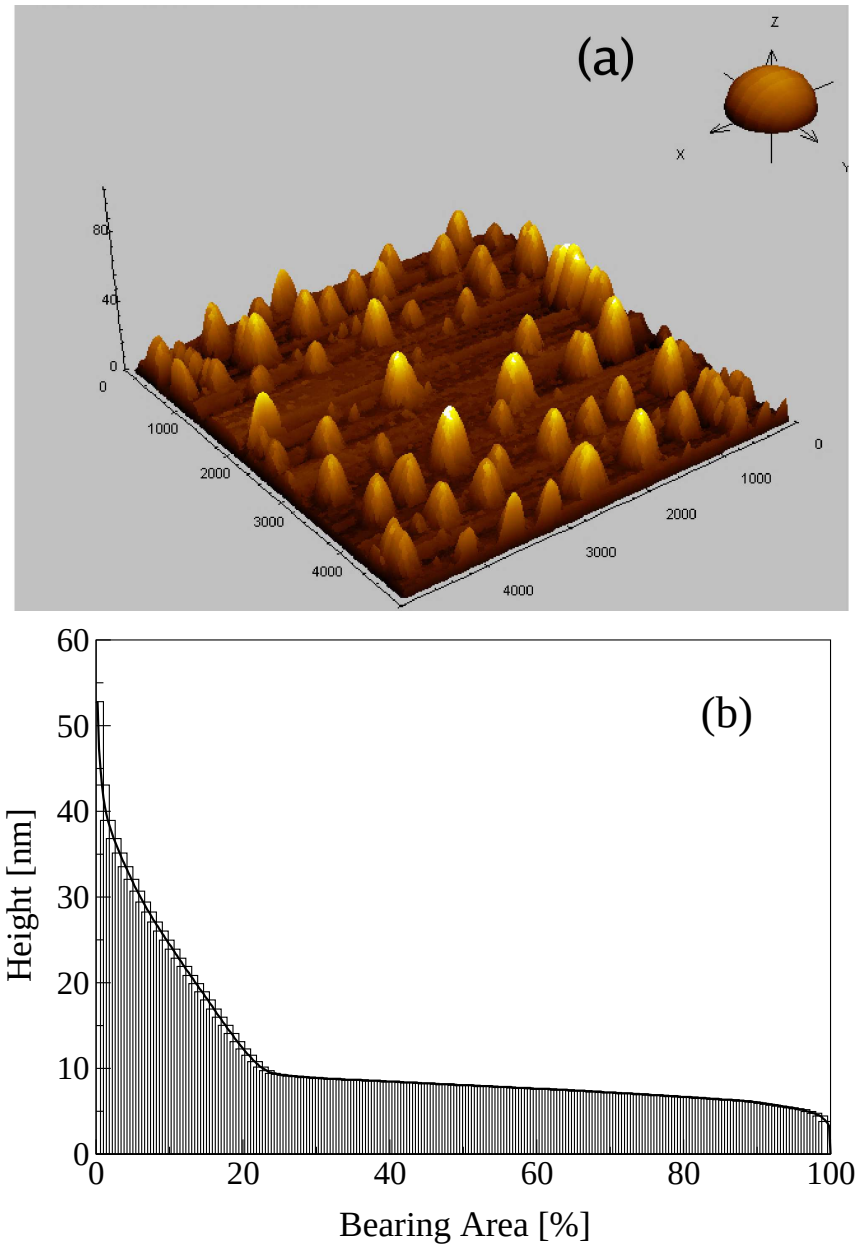

Figure 2.10: (a) 3D view of AFM image of small droplets on hydrophobic silicon substrate (X, Y and Z scales are in nm). (b) Abbot curve showing the surface height as a function of percentage bearing area.

wavelength. This leads to the rupture of the film. The critical wavelength (λ_c) is called critical spinodal wavelength. In the case of non-wettable smooth substrate, the critical spinodal wavelength λ_c is determined by the surface tension of the fluid. The dominant wavelength (λ_m) of the spinodal dewetting is the wavelength of the fastest amplified fluctuation and is related to the critical spinodal wavelength (λ_c) as $\lambda_m = \lambda_c \sqrt{2}$. The developed fluctuations with dominant spinodal wavelength determines the structure of the dewetted films. The dominant spinodal wavelength can be estimated from the direct measurement of the average distance between the patterns of the dewetted film. Volodin *et al.* have studied the criteria for the two possible mechanisms, based on substrate-film interactions [16].

We have analyzed the AFM images of the bare hydrophobic silicon substrate and the film transferred on this substrate using the "WSxM 4.0 Develop 12" software. From the roughness analysis we find that the RMS roughness of the bare substrate is around 0.18 nm (Figure 2.5(b)). The power spectral density (PSD) function of the AFM data can be used for the calculation of the periodicity of the surface structure of the substrate. The variation of PSD as a function of wavenumber for the bare substrate showed a maximum at 0.614 μm^{-1}, which yields a value of 608 nm for the dominant wavelength of the surface roughness. The dominant spinodal wavelength (λ_m) of the film was calculated from the average distance measured between the neighboring droplets and it was found to be about 350 nm. The critical spinodal wavelength ($\lambda_c = \lambda_m / \sqrt{2}$) was about 247 nm. According to the criteria given by Volodin et.al [17], if the wavelength of the substrate roughness is much larger than the critical spinodal wavelength (λ_c) of the film, then spinodal dewetting of the film can be observed. In our case, we find that the wavelength of the substrate surface roughness (608 nm) to be about three times larger than λ_c (247 nm) of the film. Hence, the mechanism of dewetting of 12D1H bilayer film on a hydrophobic silicon substrate can be attributed to the spinodal nature.

The techniques like electrowetting based microactuation for manipulation of droplets ranging from nanolitres to microlitres in volume have been shown by Pollack et. al [18]. Similar nano-dewetting structures were reported in ultra-thin films of polystyrene polymer

on silicon substrates with different oxide thicknesses [19]. They observed nanoscale dimples coexisting with mesoscopic drops. Different structures can be observed during dewetting, depending on the mechanism and kinetics of the rupture of the film [20]. The nanoscale droplets of the material with azobenzene can also be micro-manipulated by *trans-cis* photoisomerization.

2.5 Conclusions

We find that the novel material Bis[5-(4'-n-dodecyloxy benzoyloxy)-2-(4"-methyl phenylazo)phenyl] adipate (12D1H) is amphiphilic and forms stable monolayer at air-water interface. Surface manometry and BAM studies showed that the monolayer exhibited coexistence of gas and low density liquid phase at large A_m. On compression, the monolayer formed uniform low density liquid phase at A_m of 2.10 nm^2. At an A_m of 1.84 nm^2 the monolayer collapsed with a collapse pressure of 1.8 mN/m to form 3D crystallites. AFM studies of the LB film transferred onto the hydrophilic mica substrate showed domains of height 3.8 nm. This corresponds to the height of molecules with their ester groups attached to the substrate and the alkyl chains and azobenzene groups protruded into air. The limiting area obtained from the $\pi - A_m$ isotherm also indicated similar configuration of the molecules at air-water interface. This suggests that the film was transferred onto the mica substrate without much change. AFM studies of the LB film on hydrophobic silicon substrate showed domains coexisting with small droplets. This indicated that the 12D1H bilayer film transferred onto the substrate, dewetted to form nano-droplets of size of about 100 nm. Our analysis of the AFM images indicated that the dewetting process is through spinodal dewetting. Controlled dewetting of the films of azobenzene compounds can have potential applications in optical devices, biochip technology and in microelectronics.

Bibliography

[1] V. M. Kaganer, H. Möhwald, and P. Dutta, *Rev. Mod. Phys.* **71**, 779 (1999).

[2] Gareth Roberts, *Langmuir-Blodgett Films*, Plenum Press: New York and London, (1990).

[3] C. A. Rezende, L. T. Lee, and F. Galembeck, *Microscopy and Microanalysis* **11**, 110 (2005).

[4] Ignes-Mullol Jordi, C. Josep, A. Rosa, C. Joaquim, R. Ramon, R. M. Teresa, and S. Francesc, *Langmuir* **21**, 2948 (2005).

[5] J. B. Christopher, Jun-ichi Mamiya, Kevin G. Yager, and Tomiki Ikeda, *Soft Matter* **3**, 1249 (2007).

[6] Y. Yu, M. Nakano, and T. Ikeda, *Nature* **425**, 145 (2003).

[7] T. Ikeda, and O. Tsutsumi, *Science* **268**, 1873 (1995).

[8] Bharat Kumar, A. K. Prajapati, M. C. Varia and K. A. Suresh, *Langmuir* **25**, 839 (2009).

[9] J. Crusats, R. Albalat, J. Claret, Ignes-Mullol, Jordi, and F. Sagues, *Langmuir* **20**, 8668 (2004).

[10] R. K. Gupta, and K. A. Suresh, *Euro. Phys. J. E* **14**, 35 (2003).

[11] D. J. Dervichian, *J. Chem. Phys* **7**, 932 (1939).

[12] M. Broniatowski, S. I. Macho, J. Jr. Minones, and Dynarowicz-Latka, *J. Phys. Chem. B* **108**, 13403 (2004).

[13] N. Duff, J. Wang, E. K. Mann, and D. J. Lacks, *Langmuir* **22**, 9082 (2006).

[14] Y. Hashimoto, and O. Karthaus, *J. Colloid Interf. Sci*. **311**, 289 (2007).

[15] S. Kumar, and O. K. Matar, *J. Colloid Interf. Sci.* **273**, 581 (2004).

[16] P. Volodin, and A. Kondyurin, *J. Phys. D: Appl. Phys.* **41**, 065306 (2008).

[17] P. Volodin, and A. Kondyurin, *J. Phys. D: Appl. Phys.* **41**, 065307 (2008).

[18] M. G. Pollack, A. D. Shenderov, and R. B. Fair, *Lab Chip* **2**, 96 (2002).

[19] P. Muller-Buschbaum, P. Vanhoorne, V. Scheumann, and M. Stamm, *Europhys. Lett.* **40**, 655 (1997).

[20] Gunter Reiter, *Phys. Rev. Lett.* **68**, 75 (1992).

Chapter 3

Kinetics of *trans-cis* isomerization of azobenzene dimer at air-water interface

3.1 Introduction

In azobenzene materials, molecular conformation can be changed from *trans* to *cis* state or *cis* to *trans* state by isomerization using the techniques like, illumination of ultraviolet (UV) or visible light [1] or by applying an electric field [2]. Illumination of UV or visible light on the Langmuir monolayers and Langmuir-Blodgett (LB) films of azobenzene molecules may result in the *trans-cis* or *cis-trans* molecular isomerization and can be studied by surface pressure [3] or electrochemical measurements [4]. This property of reversible molecular isomerization has been utilized in developing photosensitive devices [5, 6] and wetting surfaces [7]. For many such applications, understanding the kinetics of isomerization reaction in thin film is important. Yim and Fuller have shown that the *trans* to *cis* photoisomerization reaction in Langmuir monolayers of azobenzene molecules is a first order reaction [8]. Liu *et al.* have studied the *cis* to *trans* thermal isomerization of azobenzene molecules in the LB film and found that the isomerization follows the first order kinetics [4]. There are examples of deviation from first order kinetics in the case of *trans* to *cis* photoisomerization reaction of azobenzene molecules in thin films of polymer [9]. However no such reaction kinetics have been reported at air-liquid interface.

In the previous chapter, we have reported our studies on the 12D1H monolayer in dark, where the molecules were in *trans* state. When UV light of wavelength 365 nm is illuminated, the *trans*-12D1H molecules isomerize to *cis* state (*cis*-12D1H). In this chapter, we report our surface manometry studies of the monolayer in the presence of UV light of wavelength 365 nm. We find that the monolayer in the presence of UV light (*cis*-12D1H monolayer) is even more stable with a collapse pressure of about three times higher to that of the monolayer in dark (*trans*-12D1H monolayer). We also report our studies on the kinetics of *trans* to *cis* isomerization of the azobenzene molecules under the illumination of UV light in the low density liquid phase of the Langmuir monolayer at an air-water interface. We find that the *trans* to *cis* isomerization shows deviation from the first order kinetics, unlike those reported for the condensed phase of the azobenzene monolayer [8]. The deviation from the first order kinetics can be shown as a net result of the simultaneous photoisomerization of *trans* isomers to form *cis* isomers and thermal isomerization of *cis* isomers to form *trans* isomers. We find that the rate equation written by considering a first order kinetics for *trans* to *cis* photoisomerization reaction and a second order kinetics for *cis* to *trans* thermal isomerization reaction fits well with the rate equation obtained from the experimental data. The second order kinetics mechanism for thermal isomerization reaction of *cis* isomer to form *trans* isomer is similar to the Lindemann-Hinshelwood mechanism for the unimolecular reactions at low concentration of the reactants [10, 11].

3.2 Experiment

3.2.1 Monolayer studies

The material 12D1H was synthesized by Prajapati and Varia and the purity of the sample was found to be better than 99% [12]. The surface pressure (π)−area per molecule (A_{m}) isotherm was obtained using Nima trough (611M). The trough was enclosed in an aluminum box to prevent air currents and ambient light. Wilhelmy method was used to measure the surface pressure. The stock solution of the 12D1H material prepared in the HPLC-grade chloroform

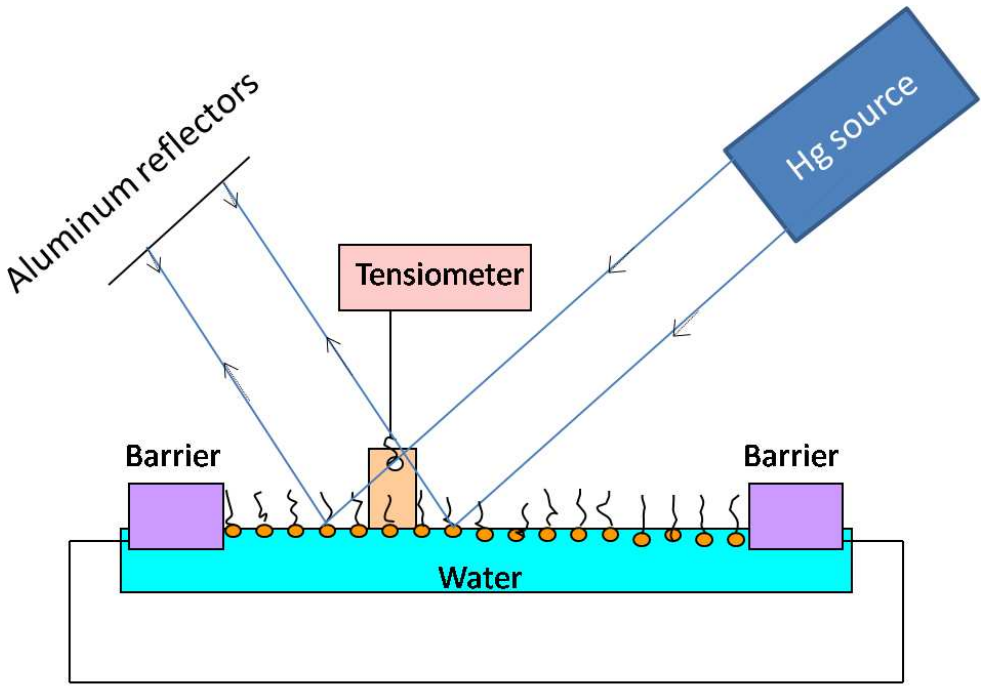

Figure 3.1: Schematic diagram of the Langmuir trough with the high pressure mercury source and aluminum reflectors.

was kept in the dark for more than 12 hours, to ensure that almost all the molecules are in the *trans* state (*trans*-12D1H). Surface manometry was carried out in the dark to get the π-A_m isotherm of the *trans*-12D1H monolayer. To get the π-A_m isotherm of the monolayer with molecules in the *cis* state (*cis*-12D1H), the monolayer was spread and compressed from the gas state under the illumination of the UV light of 365 nm wavelength. The monolayer was compressed at the rate of about 0.14 $nm^2 molecule^{-1} min^{-1}$. All the experiments were carried out at the temperature of $24 \pm 0.1°C$.

3.2.2 Isomerization studies

The schematic diagram of the setup used to study the kinetics of isomerization of the 12D1H monolayer is shown in Figure 3.1. A standalone high pressure mercury lamp of 100 W was used as a source of UV light of wavelength 365 nm and visible light of wavelength 430 nm. Interference filters (Edmund Optics) were used to select the light of required wavelengths. The intensity of the radiations was about 0.5 $mWcm^{-2}$. Aluminum sheets were

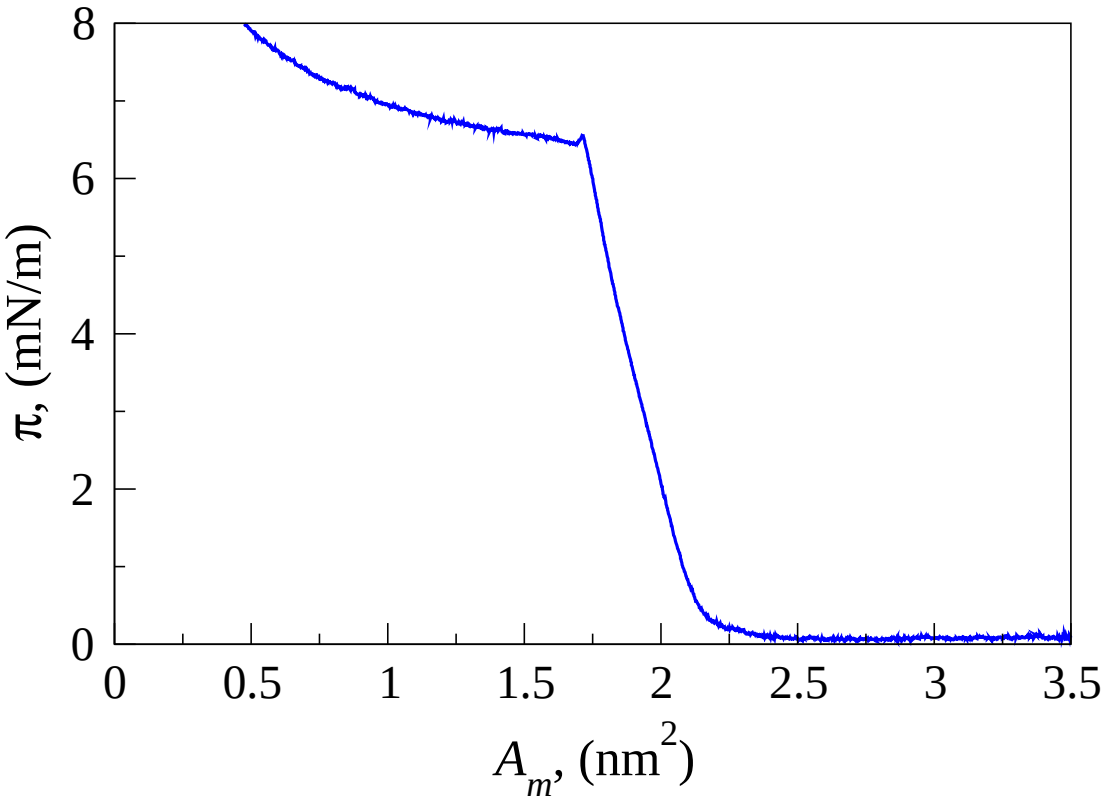

Figure 3.2: Figure shows the surface pressure (π)−area per molecule (A_m) isotherm for the monolayer in the presence of UV light of wavelength 365 nm.

used as reflectors. For the *trans* to *cis* isomerization studies in the low density liquid phase, the monolayer of *trans*-12D1H was compressed to a target area per molecule (A_t) and then illuminated with the UV light of wavelength 365 nm. The process of isomerization changes the surface pressure of the monolayer at this constant A_t. The experiment was repeated for three different values of A_t, in the low density liquid phase of the monolayer. Kinetics of isomerization was studied by measuring π as a function of time (t).

3.3 Results

3.3.1 Surface manometry

In the presence of UV light the 12D1H molecules will be in the *cis* state. The $\pi - A_m$ isotherm of the monolayer of 12D1H containing azobenzene group obtained in the presence of UV light of wavelength 365 nm is shown in Figure 3.2. The isotherm showed zero surface

pressure for an A_m greater than 2.50 nm^2. At an A_m of 2.30 nm^2, the π increased sharply. The monolayer collapsed with a π of 6.6 mN/m at an A_m of 1.71 nm^2. The stability of the monolayer in the presence of UV light was checked by holding the barriers at constant A_m and monitoring the surface pressure as a function of time. We find that the monolayer in the steep region of isotherm is stable. The limiting area of molecules in the monolayer was measured by extrapolating the steep region of the isotherm to zero surface pressure and it yielded a value of 2.10 nm^2.

3.3.2 Brewster angle microscopy

Figure 3.3 shows the BAM images of the *cis*-12D1H monolayer at various A_m. The BAM images showed the coexistence of gas and liquid phase at A_m greater than 2.50 nm^2 (Figure 3.3(a)). In between A_m of 2.30 nm^2 and 1.71 nm^2, the BAM image showed uniform phase (Figure 3.3(b)). Below an A_m of 1.71 nm^2 BAM images showed collapsed state of the monolayer (Figure 3.3(c)).

3.3.3 Kinetics of isomerization

When UV light of wavelength 365 nm was illuminated on the monolayer of *trans* isomer at a target area per molecule A_t, the surface pressure of the monolayer increased with time and then saturated to a value π_{sat}. On illuminating visible light of 430 nm on the monolayer, the surface pressure decreased with time. Repeated cycles of alternative UV and visible light leads to increase and decrease of the surface pressure (Figure 3.4).

3.4 Discussion

Surface manometry studies show that the 12D1H in the *cis* state forms stable monolayer at air-water interface. The phase corresponding to the steep region in the isotherm can be characterized from the compressional modulus ($|E|$) value of the monolayer in the presence

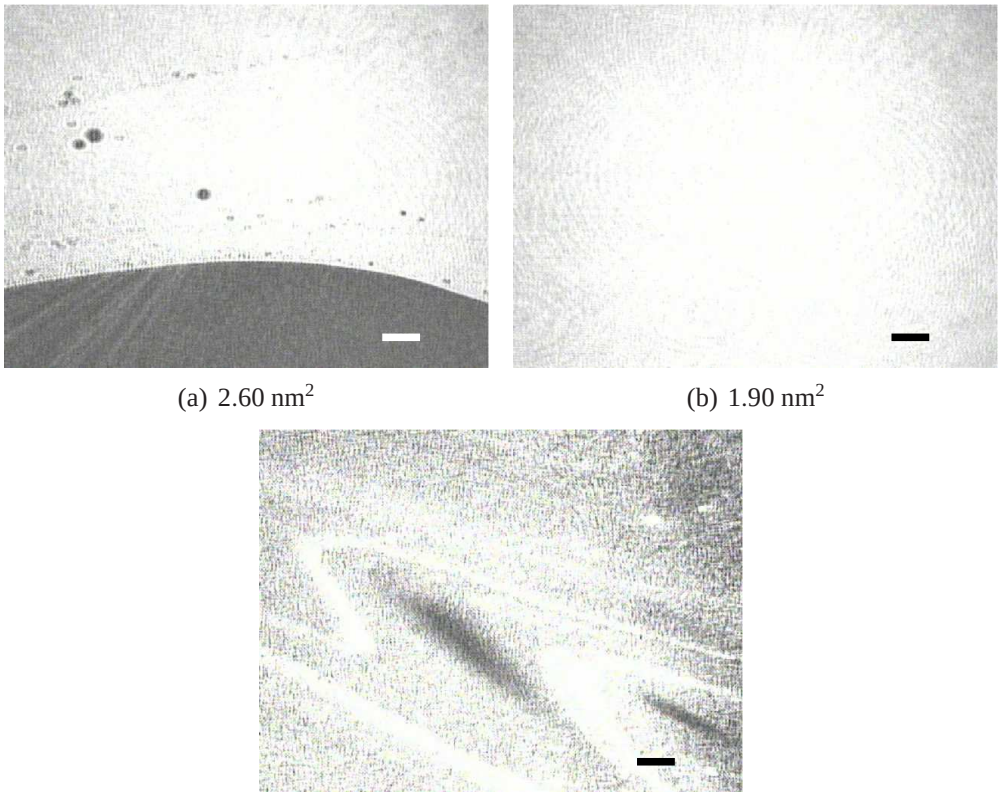

(a) 2.60 nm^2 (b) 1.90 nm^2

(c) 0.70 nm^2

Figure 3.3: Brewster angle microscope images of the 12D1H Langmuir monolayer in the presence of UV light of wavelength 365 nm at various area per molecule. (a) Shows coexistence of gas phase (dark region) and low density liquid phase (bright region) at A_m=2.60 nm^2. (b) Shows the uniform low density liquid phase of the monolayer at A_m=1.90 nm^2. (c) Shows the collapsed state of the monolayer at A_m=0.70 nm^2. The scale bar in each image represents 500 μm.

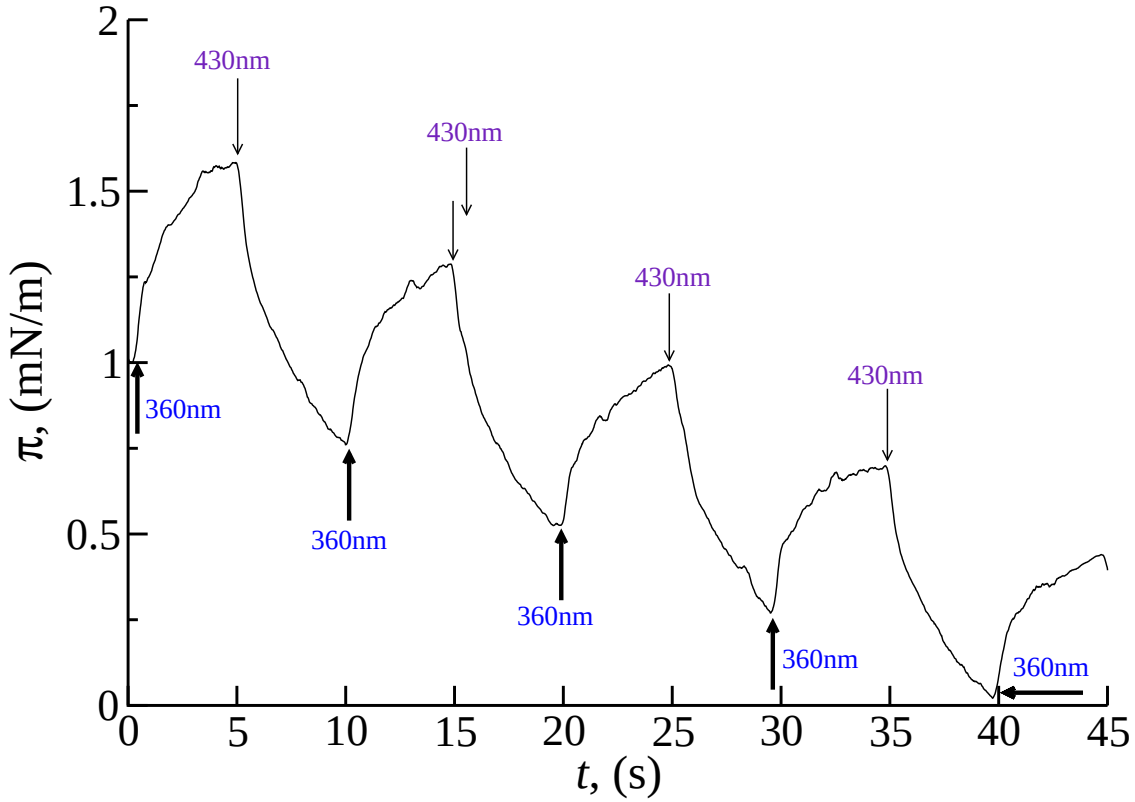

Figure 3.4: Figure shows the variation in the surface pressure (π) as function of time (t) on alternately illuminating with UV and visible radiation on the monolayer. Here the experiment was carried out at an A_m of 1.92 nm^2.

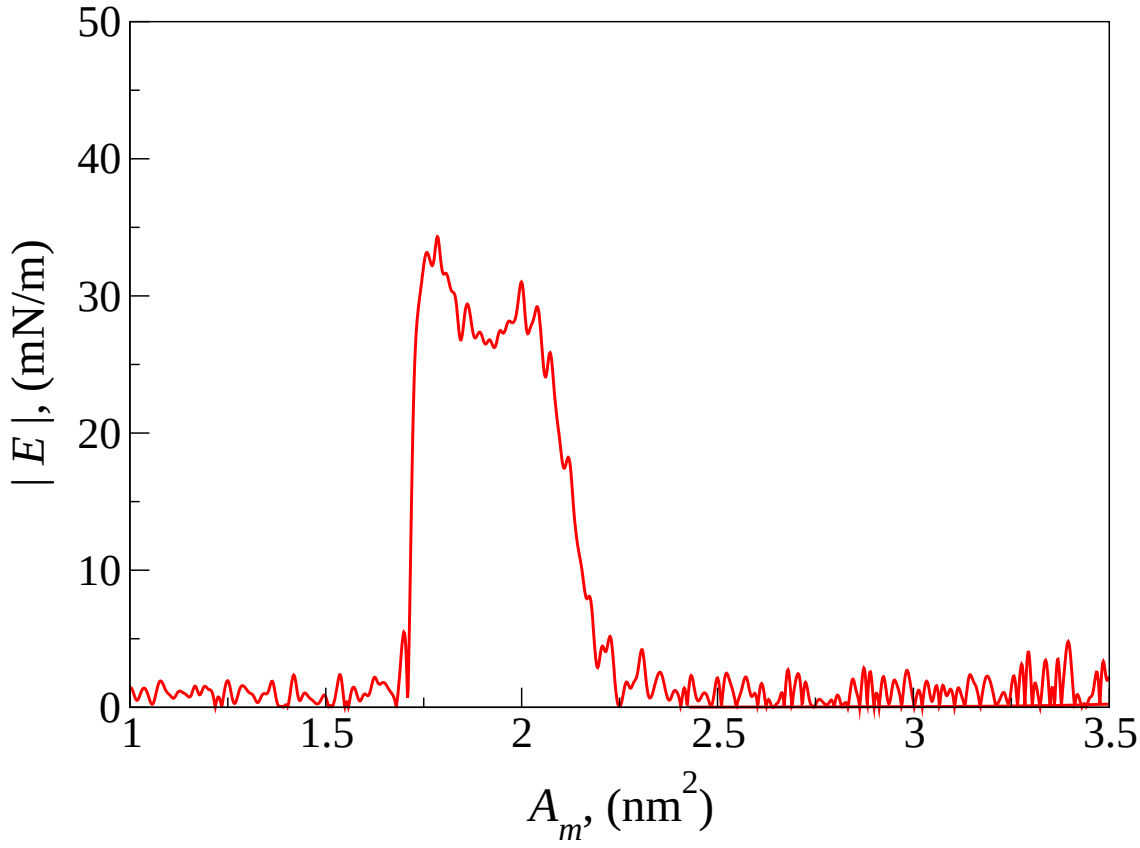

Figure 3.5: Figure shows the variation of compressional modulus ($|E|$) as a function of area per molecule (A_m), for the 12D1H monolayer in the presence of UV light of wavelength 365 nm.

of UV light. The $|E|$ value can be calculated using the relation,

$$|E| = A_m \left(\frac{\mathrm{d}\pi}{\mathrm{d}A_m} \right) \tag{3.1}$$

The maximum value of $|E|$ was equal to 34 mN/m at 1.79 nm^2 (Figure 3.5). This value corresponds to the low density liquid phase of the monolayer. From the $\pi - A_m$ isotherm, BAM and $|E|$ values, we conclude that the *cis*-12D1H monolayer exhibited low density liquid phase between the A_m of 2.15 nm^2 and 1.71 nm^2, before collapsing at a surface pressure of 6.6 mN/m.

The $\pi - A_m$ isotherm of the 12D1H monolayer in the presence of UV light exhibited significant changes as compared to the $\pi - A_m$ isotherm of 12D1H in dark. The collapse pressure increased to a value three times to that of the monolayer in dark. This indicated that the

12D1H molecules have undergone a transition from *trans* to *cis* conformation. The increase in the collapse pressure of monolayer in the presence of UV light to about three times to that of the monolayer in the dark can be attributed to the improved packing of the molecules in the *cis* state. Here, the change in the dipole moment of 12D1H molecule after isomerization [13], results in strong anchoring of the *cis*-12D1H molecules on water surface. This increases the stability of the *cis*-12D1H monolayer.

Repeated illumination of the UV light and visible light resulted in the increase and decrease of the surface pressure respectively, as a function of time. We have studied the kinetics of isomerization of the *trans* isomers to form *cis* isomers.

3.4.1 Kinetics studies

Kinetics of a reaction can be studied by measuring the rate of change of concentration of one or more reactants (or products) [11]. For isomerization reaction studies of the azobenzene dimers in the monolayer at an air-water interface, rate of change of the mole fraction of one of the isomers (*trans*-12D1H or *cis*-12D1H) has to be measured as a function of time. We have obtained the rate of change of mole fraction of *trans*-12D1H molecules in the monolayer from surface pressure measurements. We employed a method similar to the one used to study the kinetics of bulk reactions, where, the partial pressures of the reactants or products in the vapor phase are measured [11].

For *trans* to *cis* isomerization studies, the monolayer of *trans*-12D1H in the low density liquid (L_1) phase was illuminated with the UV light of wavelength 365 nm, at a target area per molecule, A_t (point A in the isotherm in Figure 3.6). Photoisomerization of *trans* to *cis* isomer results in the increase of surface pressure with time and saturates to a value of π_{sat}. Figure 3.7 shows the variation of π as a function of t for three different values of A_t. It can be seen that the π_{sat} depends on the value of A_t. The π_{sat} was less than the surface pressure (π_c°) of the *cis*-12D1H monolayer corresponding to the same A_t (point B in the isotherm in Figure 3.6). This may be due to the difference in packing of the molecules in the *cis*-12D1H monolayer obtained by two procedures; (1) illuminating the gas phase and compressing it to

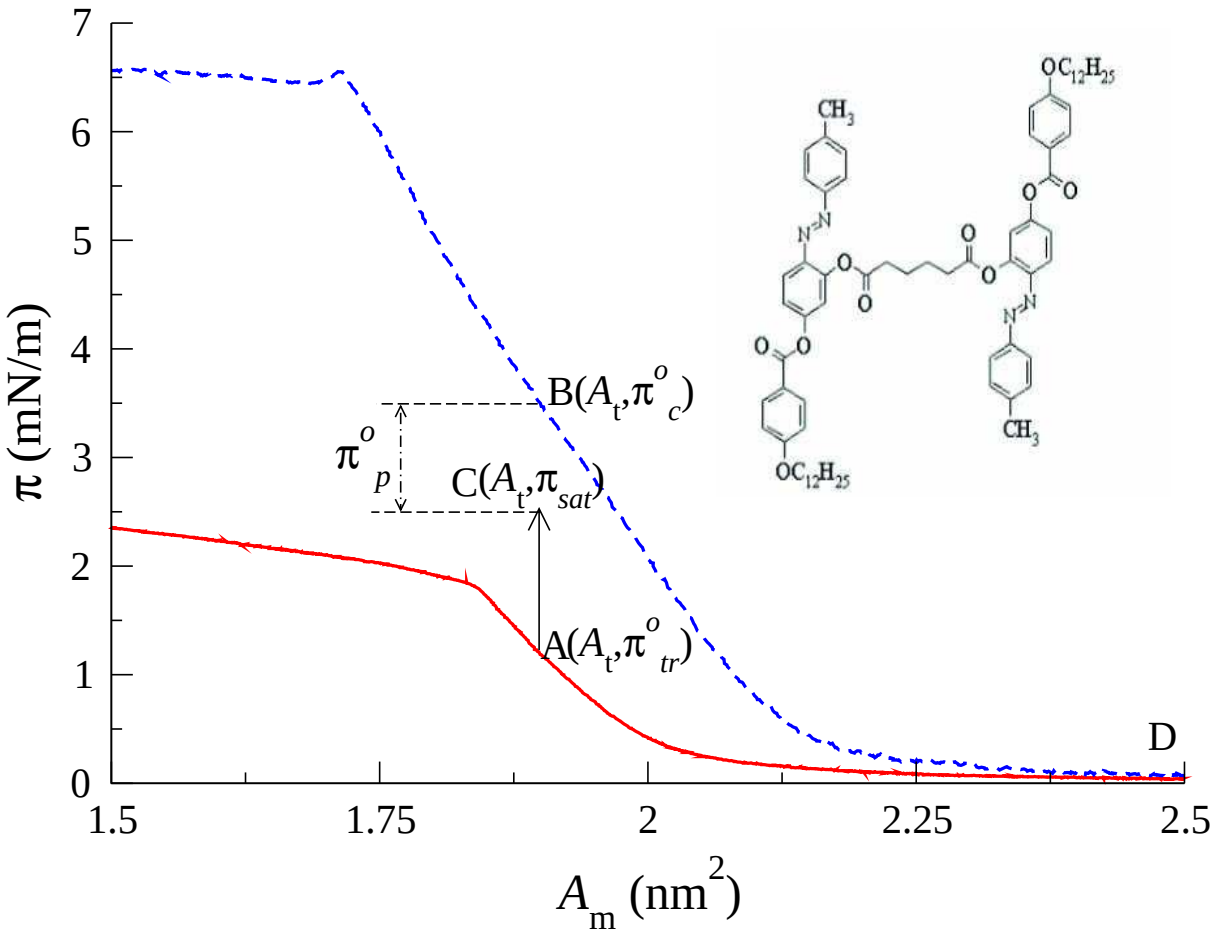

Figure 3.6: Surface pressure (π)−area per molecule (A_m) isotherms of the *trans*-12D1H monolayer (continous line) and *cis*-12D1H monolayer (dashed line). For the kinetics studies of the *trans* to *cis* isomerization, the *trans*-12D1H monolayer was illuminated with UV light (365 nm) at a target area per molecule, A_t (point A(A_t,π°_{tr})). This results in the increase of surface pressure of the monolayer with time and saturates to a value of π_{sat} (point C(A_t,π_{sat})). Molecular structure of 12D1H is shown at top right of the figure.

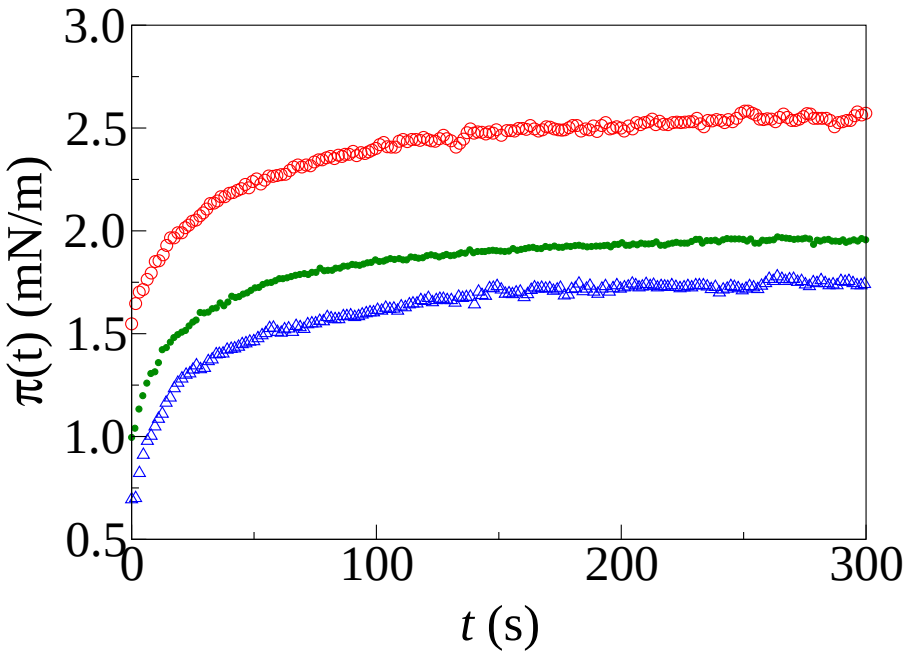

Figure 3.7: Variation of surface pressure as a function of time for three different target area per molecule (A_t); (*i*) 1.87 nm^2 (open circles), (*ii*) 1.92 nm^2 (filled circles) and (*iii*) 1.96 nm^2 (triangles), under the illumination of UV light. The corresponding π_{sat} values are (*i*) 2.67 mN/m, (*ii*) 2.03 mN/m and (*iii*) 1.83 mN/m, respectively.

the L_1 phase, (2) illuminating the *trans*-12D1H monolayer already in the L_1 phase.

The effective surface pressure of the monolayer at time (t) after illumination of UV light, can be written as the sum of surface pressures due to the individual isomers (*trans* and *cis*) and the surface pressure component arising from the packing of the molecules, i.e.,

$$\pi(t) = \pi_{tr}(t) + \pi_c(t) + \pi_p(t) \tag{3.2}$$

Here, $\pi(t)$ is the measured (effective) surface pressure of the monolayer at the target area per molecule A_t after time t of illumination of UV light, $\pi_{tr}(t)$ is the surface pressure component due to the *trans* isomer, $\pi_c(t)$ is the surface pressure component due to the *cis* isomer and $\pi_p(t)$ is the surface pressure component due to the effect of packing of molecules. The term $\pi_p(t)$ is the result of packing differences between the *trans* and *cis* isomers in the monolayer. We assume that this term is proportional to the mole fraction of the *cis* isomers. Considering the surface pressure component due to *trans* isomer to be proportional to the mole fraction

of *trans* isomer and the surface pressure component due to the *cis* isomer to be proportional to the mole fraction of *cis* isomer in the monolayer, we have from equation 3.2,

$$\pi(t) = \Gamma_{tr}(t)\pi^{\circ}_{tr} + \Gamma_{c}(t)\pi^{\circ}_{c} + \pi_{p}(t) \tag{3.3}$$

Here, $\Gamma_{tr}(t)$ is the mole fraction of *trans* isomer at time *t*, $\Gamma_{c}(t)$ is the mole fraction of *cis* isomer at time *t*, π°_{tr} is the surface pressure of the monolayer of pure *trans* isomer at A_t and π°_{c} is the surface pressure of the monolayer of pure *cis* isomer at A_t. $\pi_p(t)$ is assumed to be proportional to the $\Gamma_{c}(t)$ and hence it can be written as $\Gamma_{c}(t)\pi^{\circ}_{p}$, where $\pi^{\circ}_{p} = \pi_{sat} - \pi^{\circ}_{c}$. In the present case π°_{p} is a negative quantity (Figure 3.2). Thus the effective surface pressure of the monolayer turns out to be,

$$\pi(t) = \Gamma_{tr}(t)\pi^{\circ}_{tr} + \Gamma_{c}(t)\pi^{\circ}_{c} + \Gamma_{c}(t)\pi^{\circ}_{p} \tag{3.4}$$

Since $\Gamma_{tr}(t) + \Gamma_{c}(t) = 1$, equation 3.4 yields the following expression,

$$\Gamma_{tr}(t) = \left[\frac{\pi(t) - \pi^{\circ}_{c} - \pi^{\circ}_{p}}{\pi^{\circ}_{tr} - \pi^{\circ}_{c} - \pi^{\circ}_{p}}\right] \tag{3.5}$$

We define the term $\pi_i(t) = \Gamma_i(t)\pi^{\circ}_{i}$ as "partial surface pressure" of the isomer *i* ($i = tr$ or c). The partial surface pressure of *trans* isomer at time *t* is given by $\pi_{tr}(t) = \Gamma_{tr}(t)\pi^{\circ}_{tr}$. Substituting $\Gamma_{tr}(t)$ from equation 3.5, we get the following expression for the partial surface pressure of *trans* isomer.

$$\pi_{tr}(t) = \pi^{\circ}_{tr}\left[\frac{\pi(t) - \pi^{\circ}_{c} - \pi^{\circ}_{p}}{\pi^{\circ}_{tr} - \pi^{\circ}_{c} - \pi^{\circ}_{p}}\right] \tag{3.6}$$

The values of π°_{tr} and π°_{c} can be obtained from the isotherms of pure *trans*-12D1H and pure *cis*-12D1H monolayers, respectively. Experimentally we have measured $\pi(t)$ as a function of *t* for three different values of A_t (Figure 3.7). The value of π°_{p} can be obtained by the relation $\pi^{\circ}_{p} = \pi_{sat} - \pi^{\circ}_{c}$, where π_{sat} for a given value of A_t, is obtained from Figure 3.7. Using these values, we can calculate $\pi_{tr}(t)$ from equation 3.6. The calculated values of $\pi_{tr}(t)$ are plotted as a function of *t* (Figure 3.8).

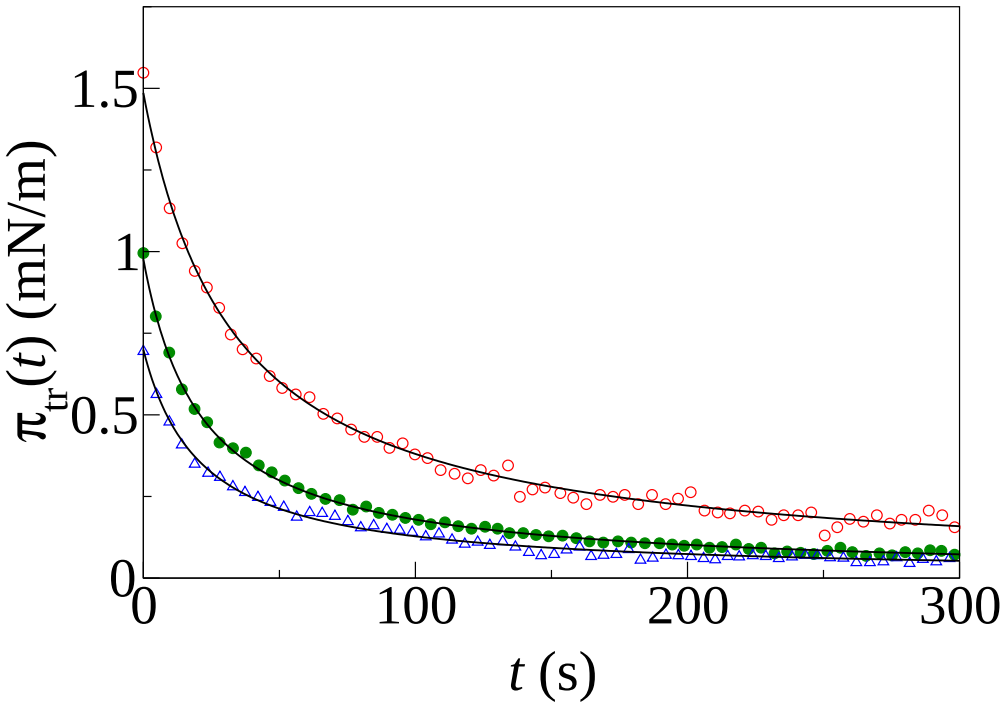

Figure 3.8: Calculated partial surface pressure of *trans* isomer ($\pi_{tr}(t)$) plotted as a function of time for three different values of A_t; (*i*) 1.87 nm^2 (open circles), (*ii*) 1.92 nm^2 (filled circles) and (*iii*) 1.96 nm^2 (open triangles). Continuous line is computed using equation 3.7 to fit the data.

For a first order *trans* to *cis* isomerization reaction, $\pi_{tr}(t)$ (which is proportional to $\Gamma_{tr}(t)$) should be an exponential function of time [8]. However from Figure 3.8, we find that the $\pi_{tr}(t)$ data could not be described by exponential function. On the other hand the curves can be fitted to a equation of the type:

$$\pi_{tr}(t) = \frac{a}{1+bt} + c \tag{3.7}$$

Here a, b and c are the fit parameters. The correlation coefficient for the fit was found to be better than 0.99.

To obtain the rate equation for the *trans* to *cis* isomerization reaction we differentiate equation 3.7 with respect to time t and express it in terms of $\pi_{tr}(t)$,

$$\frac{d\pi_{tr}(t)}{dt} = -\frac{b}{a}\pi_{tr}^2(t) + \frac{2bc}{a}\pi_{tr}(t) - \frac{bc^2}{a}$$

Since, $\pi_{tr}(t) = \Gamma_{tr}(t)\pi^{\circ}_{tr}$,

$$\frac{d\Gamma_{tr}(t)}{dt} = -\frac{b\pi^{\circ}_{tr}}{a}\Gamma^2_{tr}(t) + \frac{2bc}{a}\Gamma_{tr}(t) - \frac{bc^2}{a} \tag{3.8}$$

Kinetics model

The *trans* to *cis* photoisomerization of azobenzene molecules at air-water interface has been reported to be a first order reaction [8]. Thermal *cis* to *trans* isomerization in the LB film was also reported to be a first order reaction [4]. However, in the case of thin film of polymer containing azobenzene, Mita *et al.* reported that *trans* to *cis* photoisomerization deviates from the first order kinetics [9]. They have reported that the *trans* to *cis* photoisomerization followed first order kinetics upto 86 % conversion and then deviated from the first order kinetics. To explain the non-first order reaction, they proposed a kinetics model considering the influence of free volume distribution in the polymer matrix on the *trans* to *cis* isomerization. Interestingly, in our system the deviation was observed from the initial stage itself. In our system since the molecules are in the L_1 phase at an air-water interface, the free volume available for the azobenzene moiety is greater than the critical volume required for the isomerization. Hence the isomerization reaction is not restricted by the free volume distribution unlike in the case of the azobenzene molecules trapped in the solid polymer matrix. In equation 3.8, the $\Gamma^2_{tr}(t)$ term suggests that there is another reaction following second order kinetics, simultaneously proceeding in the opposite direction to that of the photoisomerization. The reverse reaction may be the thermal isomerization of the metastable *cis* isomer to form *trans* isomer [4].

Under the illumination of UV light on the *trans*-12D1H monolayer, the net rate of the isomerization reaction depends on two processes: (a) Photoisomerization of *trans* isomers to form *cis* isomers and (b) thermal isomerization of the *cis* isomers to form *trans* isomers by colliding with other molecules. The rate of change of *trans* isomers is thus given by the

following rate equation [10],

$$\frac{d\Gamma_{tr}(t)}{dt} = -k\,\Gamma_{tr}(t) + k_{col}\,\Gamma_c(t)\Gamma_{tr}(t) \tag{3.9}$$

where, k is the rate constant for photoisomerization reaction of *trans* isomer and k_{col} is the rate constant for the thermal isomerization reaction of the *cis* isomer. Since $\Gamma_c(t) = 1 - \Gamma_{tr}(t)$, we have,

$$\frac{d\Gamma_{tr}(t)}{dt} = -k_{col}\Gamma_{tr}^2(t) + (k_{col} - k)\Gamma_{tr}(t) \tag{3.10}$$

This equation shows that the rate of change of mole fraction of the *trans* isomer is governed in the initial stages of isomerization reaction by the first term and in the later stages by the second term. Eventually the two terms will become equal resulting in a steady value for $\Gamma_{tr}(t)$. Equation 3.10 is similar to equation 3.8, except for the constant term which is negligible ($\approx 10^{-6}$). Hence, the above kinetic model of isomerization can explain the experimental result. Solving equation 3.10 for $\Gamma_{tr}(t)$, we get,

$$\Gamma_{tr}(t) = \frac{\Gamma_\circ \Delta k}{\Delta k + (\Gamma_\circ k_{col} - \Delta k)(1 - e^{-\Delta k.t})} \tag{3.11}$$

Here, $\Delta k = k_{col} - k$ and $\Gamma_\circ$ is the concentration of *trans* isomers at $t = 0$. Since before the illumination of UV light all the molecules are in *trans* state we have $\Gamma_\circ = 1$. Equation 3.11 is fitted with the experimental data and the rate constants are calculated from the fit parameters. Figure 3.9 shows variation of Γ_{tr} as a function of t. The continuous line shows the fit according to equation 3.11. along with the fitted curve. Table 1 gives the values of the rate constants calculated for three different A_t.

We have proposed a simple model which takes into account the thermal isomerization of the *cis* isomers to form *trans* isomers. Since, in our system the monolayer is in the L_1 phase, we assume that there is no orientational ordering of the azobenzene moieties of the *cis* isomers.

Studies on the kinetics of *trans* to *cis* photoisomerization reaction in azobenzene contain-

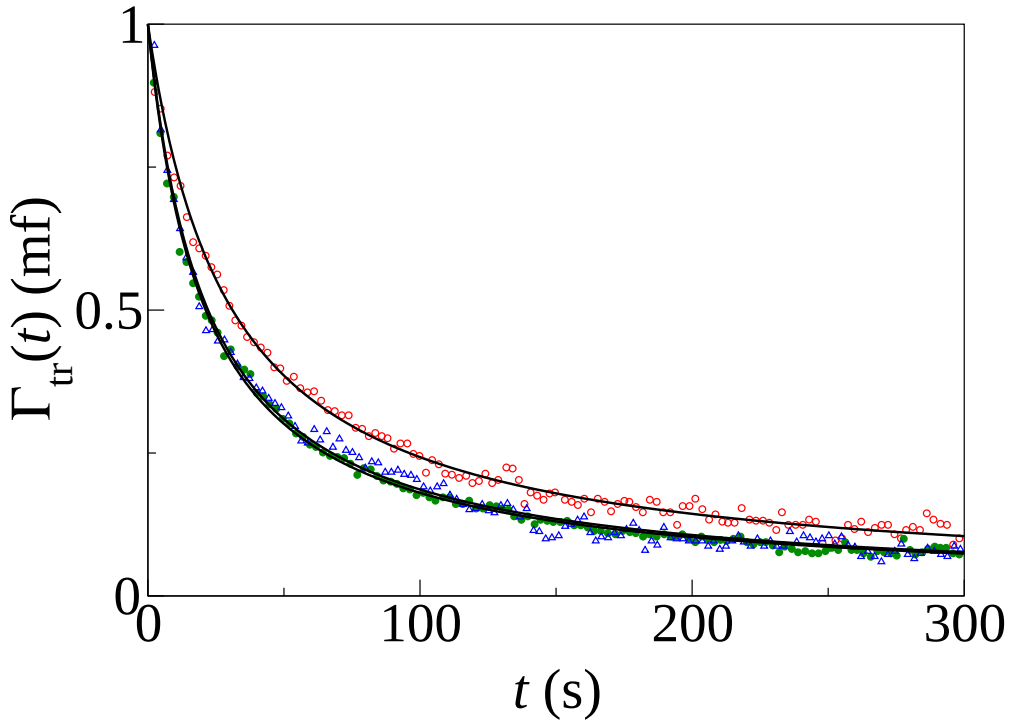

Figure 3.9: Calculated mole fraction of *trans* isomer ($\Gamma_{tr}(t)$) plotted as a function of time for three different values of A_t; (*i*) 1.87 nm^2 (open circles), (*ii*) 1.92 nm^2 (filled circles) and (*iii*) 1.96 nm^2 (open triangles). Continuous line is computed using equation 3.11 to fit the data.

Table 3.1: Values of rate constants (k and k_{col}) for *trans* to *cis* isomerization at different target area per molecule (A_t).

A_t (nm^2)	π°_{tr} (mN/m)	π°_c (mN/m)	k (s^{-1})	k_{col} (s^{-1})
1.96	0.69	2.70	0.0456	0.0465
1.92	0.99	3.18	0.0474	0.0483
1.87	1.54	3.98	0.0326	0.0335

ing fatty acid molecules at an air-water interface, have reported the rate constant values, *k* to be 9.50×10^{-2} s^{-1} and 3.55×10^{-2} s^{-1} for nearest neighbour tilt (NN) phase and next nearest neighbour tilt (NNN) phase, respectively [8]. The different *k* values for the two phases, show the influence of the molecular packing and structure of the monolayer on the rate of photoisomerization. The *k* value obtained for our system is of the same order of magnitude (Table 1) and somewhat in between that of NN and NNN phase of the fatty acid monolayer.

The considerable contribution of the thermal isomerization of the *cis* isomers towards the kinetics of isomerization of 12D1H molecules unlike in the fatty acids can be attributed to the monolayer phase. In the case of fatty acids, the *cis* isomer in the nearest neighbour phase (NN phase) and next nearest neighbour phase (NNN phase) is relatively more stable than the 12D1H *cis* isomer in the L_1 phase. In the L_1 phase of the monolayer, the molecules have more degrees of freedom and hence there will be high probability of *cis* isomers getting excited by collisions. On the other hand, the NN and NNN phases of fatty acid monolayers are condensed phases and the molecules in these phase have relatively few degrees of freedom, resulting in the higher stability of the metastable *cis* isomers.

In our system, the rate equation shows that the *cis* to *trans* thermal isomerization reaction follows the second order kinetics. This is similar to the Lindemann-Hinshelwood mechanism for unimolecular reactions [11, 14] at low concentration of reactants. Lindemann-Hinshelwood mechanism is a two step reaction mechanism [14, 15]. First, a reactant molecule with large number of degrees of freedom, gets activated by colliding with other molecules. This is a bimolecular event involving two molecules. Then the activated molecule decays to form the product. This is a unimolecular event. The overall rate of the reaction is determined by the slower reaction step. In the present case, the thermal isomerization of *cis* isomers involves two steps: (a) Formation of the activated *cis* isomers and (b) decay of the activated *cis* isomers to form *trans* isomers. In the L_1 phase of the monolayer, the collision frequency of the molecules is less and hence the formation of the activated *cis* isomers will be slow as compared to the decay of activated molecules. Hence, the formation of the activated *cis* isomers will be the rate determining step. The activation of the *cis* molecules by collision

is a bimolecular event and hence the reaction will have overall second order kinetics. In many devices which make use of thin film of azobenzene materials, e.g., the photomechanical devices [1], kinetics of isomerization plays an important role. We have shown that the reverse thermal isomerization of metastable *cis* isomers in the low density liquid phase can contribute towards the overall reaction rate. These effects have to be considered for making devices with desired applications.

3.5 Conclusions

Our studies on the monolayer in the presence of UV light showed significant changes in the $\pi - A_m$ isotherm as compared to the monolayer in dark. The collapse pressure of the monolayer in the presence of UV light (*cis*-12D1H monolayer) was about three times higher than the monolayer in dark (*trans*-12D1H monolayer) indicating that the *cis*-12D1H monolayer is more stable than the *trans*-12D1H monolayer.

We have studied the *trans* to *cis* isomerization of mesogenic azobenzene dimer (12D1H) under the illumination of UV light at an air-water interface. We have employed a novel approach to analyze the experimental results. From our analysis, we find that the *trans* to *cis* isomerization reaction shows deviation from the first order kinetics. We attribute this deviation to the simultaneous photoisomerization of *trans* isomers to form *cis* isomers and the reverse thermal isomerization of the metastable *cis* isomers to form *trans* isomers. Our analysis indicates a first order kinetics for *trans* to *cis* photoisomerization reaction and a second order kinetics for the thermal isomerization reaction of *cis* isomers to form *trans* isomers. The mechanism of thermal isomerization is similar to the Lindemann-Hinshelwood mechanism for unimolecular reactions at low concentration of reactants. In our system, the thermal isomerization reaction has two steps i.e., formation of activated *cis* isomers by collision of *cis* isomers with other molecules and then the decay of activated *cis* isomers to form *trans* isomers. The formation of activated *cis* isomers is slow as compared to the decay of the activated *cis* isomers, and hence the former step governs the rate of reaction. Since the

formation of activated *cis* isomers is a bimolecular event, the thermal isomerization reaction has an overall second order kinetics.

Bibliography

[1] C. J. Barrett, J. ichi Mamiya, K. G. Yager, and T. Ikeda, *Soft Matter* **3**, 1249 (2007).

[2] M. Alemani, M. V. Peters, S. Hecht, K. Rieder, F. Moresco, and L. Grill, *J. Am. Chem. Soc.* **128**, 14446 (2006).

[3] P. Viswanath and K. A. Suresh, *Langmuir* **20**, 8149 (2004).

[4] Z. -F. Liu, K. Morigaki, T. Enomoto, K. Hashimoto, and A. Fujishima, *J. Phys. Chem.* **96**, 1875 (1992).

[5] A. Kocer, M. Walko, W. Meijberg, and B. L. Feringa, *Science* **309**, 755 (2005).

[6] X. Feng, L. Feng, M. Jin, J. Zhai, L. I. Jiang, and D. Zhu, *J. Am. Chem. Soc.* **126**, 62 (2004).

[7] H. S. Lim, J. T. Han, D. Kwak, M. Jin, and K. Cho, *J. Am. Chem. Soc* **128**, 14458 (2006).

[8] K. S. Yim, and G. G. Fuller, *Phys. Rev. E* **67**, 041601 (2003).

[9] I. Mita, K. Horie, and K. Hirao, *Macromolecules* **22**, 558 (1989).

[10] C. A. Hollingsworth, P. G. Seybold, L. B. Kier, and C. K. Cheng, *Int. J. Chem. Kinet.* **36**, 230 (2004).

[11] P. Atkins, *Physical Chemistry* Oxford University Press, (2006).

[12] B. Kumar, A. K. Prajapati, M. C. Varia, and K. A. Suresh, *Langmuir* **25**, 839 (2009).

[13] K. Ichimura, S. Oh, and M. Nakagawa, *Science* **288**, 1624 (2000).

[14] F. A. Lindemann, *Trans. Faraday Soc.* **17**, 598 (1922).

[15] C. N. Hinshelwood, *Proc. R. Soc. (London)* **A113**, 230 (1927).

Chapter 4

Stress-strain relation in the Langmuir monolayer of a novel dimer of disc shaped moiety

4.1 Introduction

Films at air-water interface are ideal model systems for studying some physical properties in two-dimension (2D). Here different 2D phases can be obtained by compressing the monolayer between two moving barriers [1]. The monolayer can also be compressed from an uniform phase to the collapsed state wherein the molecules go into the third dimension (3D). The mechanism of the collapse depends on factors like the phase of the monolayer, pH and ions present in the subphase [2, 3]. It is known that the condensed monolayer can collapse by forming 3D crystallites, or by forming multilayers [4]. Although the physical properties of a material in two dimensional system can be different from the bulk, the concepts developed to describe the bulk materials can be extended to describe the properties of 2D systems. For example, in the study of the monolayer rheology the bulk continuum concepts have been applied to monolayers [5]. Similarly, using constitutive equations based on the stress-strain models of bulk solids, Kampf *et al.* [6] related the experimental parameters of an insoluble monolayer to study the collapse behavior.

In this chapter, we report our studies on the monolayer of a novel dimer of disk shaped triphenylene moiety, terephthalic acid bis-[6-(3,6,7,10,11-pentahexyloxy-triphenylen-2-yloxyl)-hexyl] ester (tp-dimer), at air-water interface. It is known that molecules with disk shaped moieties can take either face-on or edge-on configuration at air-water interface depending on the area per molecule and surface pressure [7, 8]. In the edge-on configuration the molecules can assemble into columns with the column axis parallel to the interface. The self-assembly of the molecules containing discotic core to form column-like structures is attributed to the strong $\Pi - \Pi$ interaction between the aromatic rings. The intermolecular distance in these columns will be about 0.34 nm. Such films transferred onto the solid substrates are of importance as they have high degree of anisotropy in conductance. The electrical conductivity along the column will be higher as compared to the conductivity across the columns. These systems behave like quasi 1-dimensional conductors and can have potential applications [9, 10]. Hence understanding the stability of the film under different conditions of temperature and strain is important.

We have studied the collapse of the tp-dimer Langmuir monolayer at air-water interface as a function of compression rate and temperature. We find that the collapse pressure increases with increase in compression rate. We consider the surface pressure of monolayer as stress and compression of monolayer as strain [6]. The strain rate is calculated from the compression rate. For metals and polymers, it has been reported that the strain rate has Arrhenius temperature dependence and the yield stress is related to the strain rate by a power law [11, 12]. We find that in the case of monolayer of tp-dimer, the strain rate is related to the collapse pressure by a power law, but in the absence of plastic flow region unlike those reported for Langmuir monolayers [6, 13]. Our studies on the effect of temperature on the collapse pressure showed that the collapse pressure decreases with increase in temperature. Assuming the Arrhenius temperature dependence of the strain rate, we have calculated the activation energy for the collapse of monolayer.

4.2 Experiment

The material tp-dimer was synthesized by Sandeep Kumar and S. K. Gupta. The purity of the material was found to be better than 99% by NMR, IR and elemental analysis techniques. The Langmuir monolayer of the material tp-dimer was studied by surface manometry and Brewster angle microscopy (BAM) techniques. The solution of tp-dimer was prepared in HPLC grade chloroform with a concentration of about 0.1 mg/ml. Surface manometry studies were carried out using a Nima trough (Model: 611M). Ultra-pure deionized water (MilliQ) of resistivity 18 MΩcm and pH of 5.7 was used as subphase. The freshly made solution was spread on the subphase using a microsyringe. The solvent was allowed to evaporate for 15 minutes before compressing the monolayer between two moving barriers. To study the effect of compression rate on the collapse pressure of monolayer, the speed of the barriers was varied in the range of 7 – 100 cm^2min^{-1}. This corresponds to a compression rate of the monolayer in the range 0.10 – 1.50 $nm^2molecule^{-1}min^{-1}$. The temperature of the subphase was controlled by circulating water through the trough using a temperature controller (Julabo, Model: F25). The monolayer was studied at different temperatures in the range 15 – 32°C. The BAM studies were carried out using MiniBAM (NFT, Nanotech) and the images were obtained using a frame grabber.

The Langmuir-Blodgett (LB) films of tp-dimer were prepared on hydrophilic and hydrophobic substrates. The double-side mirror polished silicon wafers were used as hydrophilic substrates. They were cleaned by sonicating them in boiling piranha solution (mixture of concentrated H_2SO_4 and H_2O_2 in 3 : 1 ratio) for about five minutes. The cleaned wafers were then repeatedly rinsed with fresh millipore water before transferring the film. One layer of the film gets transferred during one dipping cycle.

The hydrophobic substrates were obtained by preparing self assembled monolayer of hexamethyl disilazane (HMDS) on polished silicon wafers as explained in the experiment section of chapter 2. The cleaned hydrophobic silicon substrates were then used to transfer the film by LB technique. Two layers of the film get transferred onto a hydrophobic substrate

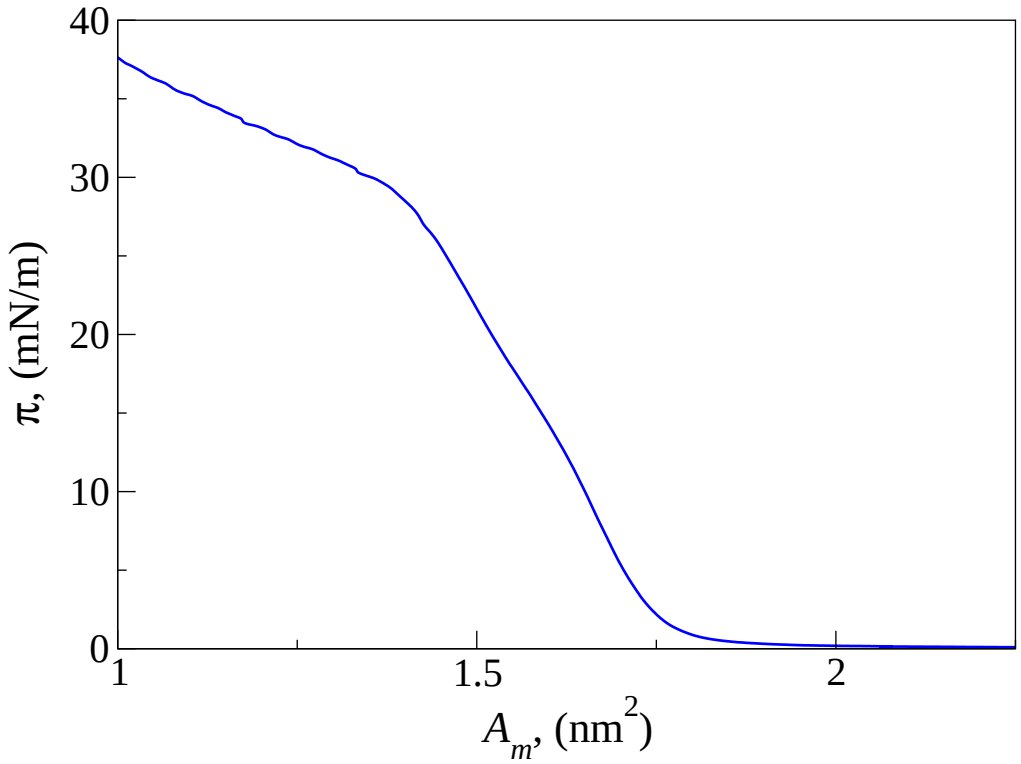

Figure 4.1: Surface pressure (π)−area per molecule (A_m) isotherm of tp-dimer monolayer at 15°C. The monolayer was compressed with a compression rate of 0.10 nm^{2}molecule^{-1}min^{-1}.

in one dipping cycle. The transfer of the film was carried out at a surface pressure of 5 mN/m with a dipping speed of 2 mm/minute.

The atomic force microscope (AFM) studies (Molecular Imaging, Model: Picoplus) were carried out to characterize the LB film of tp-dimer. The sample was scanned in the acoustic AC mode using the cantilever of spring constant of about 30 N/m and resonance frequency of about 175 kHz.

4.3 Results

4.3.1 Surface manometry

The surface pressure (π)−area per molecule (A_m) isotherm obtained by compressing the monolayer with a speed of 0.10 nm^{2}molecule^{-1}min^{-1} and at a temperature of 15°C is shown in Figure 4.1. At large A_m, the isotherm shows zero surface pressure. The π starts increasing

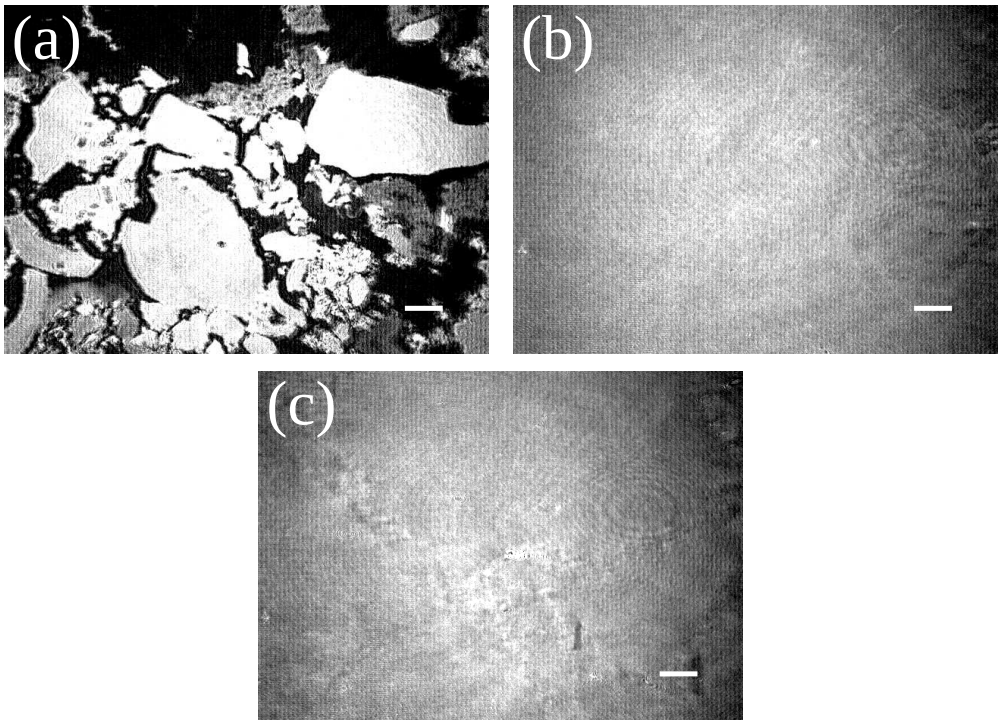

Figure 4.2: BAM images of the tp-dimer monolayer at different area per molecule. (a) Shows coexistence of gas phase (dark region) and liquid condensed phase (grey region) at A_m of 3.00 nm^2. (b) Shows uniform phase at A_m of 1.70 nm^2. (c) Shows the collapsed state at A_m of 1.61 nm^2. The scale bar in each image represents 500 μm.

at A_m of 1.80 nm^2. After the sharp rise in π, a kink is observed in the isotherm at an A_m of 1.63 nm^2, suggesting a phase transition. Below this area per molecule, the surface pressure of the monolayer held at constant A_m decreases sharply with time. This indicates the collapse of monolayer. The limiting area ($A_\circ$) obtained by extrapolating the steep region of the isotherm to zero surface pressure was 1.75 nm^2.

4.3.2 Brewster angle microscopy

The phases exhibited by the monolayer at various area per molecule as the monolayer is compressed between the moving barriers were observed using a BAM. The BAM images at A_m greater than 1.80 nm^2 showed the coexistence of dark and grey regions (Figure 4.2(a)). Uniform phase was observed between the A_m of 1.80 nm^2 and 1.63 nm^2 (Figure 4.2(b)). At an A_m of 1.63 nm^2 bright 3D crystallites appeared from the uniform grey phase (Figure 4.2(c)) which continued to grow with further increase in π. This indicated a phase transition from

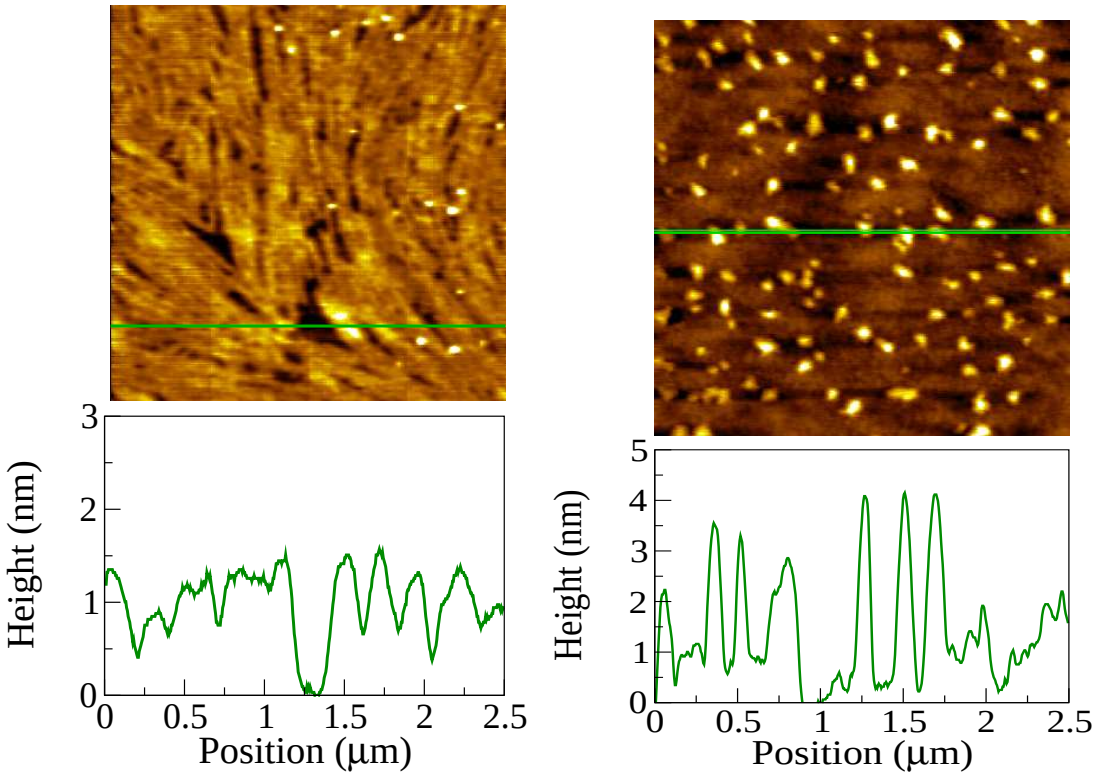

(a) 5 mN/m (b) 15 mN/m

Figure 4.3: AFM image of the LB film of tp-dimer on a hydrophilic silicon substrate. (a) Shows the monolayer film transferred at a surface pressure of 5 mN/m. The line profile yields an average thickness of the film to be about 1.5 nm. (b) Shows the film transferred at the surface pressure of 15 mN/m. Here the particles of size 2 – 4 nm were observed.

the uniform phase to the collapsed state. On expanding the film in the collapsed state, the monolayer was not restored. This suggests that the collapse of the film was irreversible.

4.3.3 Atomic force microscopy

The LB film transferred onto a hydrophilic silicon substrate was studied using an AFM. The transfer ratio of the film was about 90%. Figure 4.3(a) shows the AFM topography image of the monolayer film transferred onto a hydrophilic silicon substrate at a surface pressure of 5 mN/m. The line profile on the topography image yielded the height of the film to be about 1.5 nm. Figure 4.3(b) shows the topography image of the film transferred onto a hydrophilic silicon substrate at a surface pressure of 15 mN/m. Here 3D crystallites of height between 2 – 4 nm were observed.

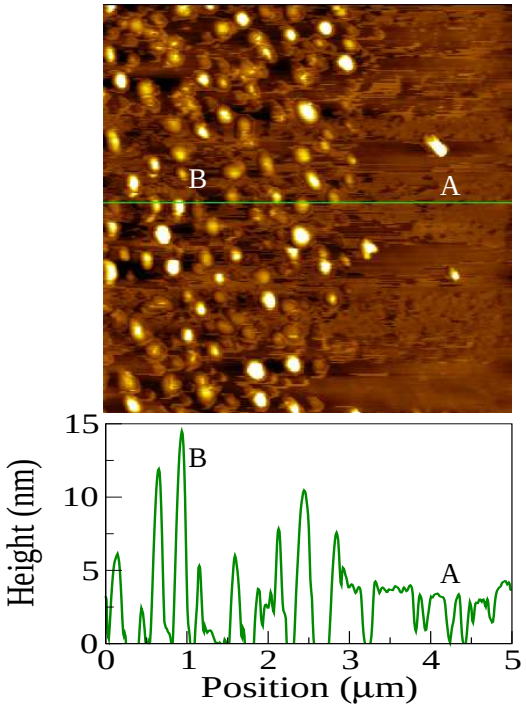

Figure 4.4: AFM image of the LB bilayer film of tp-dimer on a hydrophobic silicon substrate. Here the film was transferred at a surface pressure of 5 mN/m. The bilayer film (marked as A) of height of about 3.5 nm was observed along with the droplets (marked as B) of height varying between 5 – 15 nm.

Figure 4.4 shows the AFM topography image of the LB film on a hydrophobic silicon substrate transferred at a surface pressure of 5 mN/m. On the hydrophobic surfaces the transfer occurs during the down stroke and as well as during upstroke of the substrate and hence two layers of the film get transferred in one dipping cycle. The transfer ratio was about 80% during both downstroke and upstroke of the substrate. AFM image shows the film coexisting with the droplets of varying size. The line profile on the topography image yielded the height of the film to be about 3.5 nm. The height of the droplets varied between 5 – 15 nm as given by the line profile in Figure 4.4.

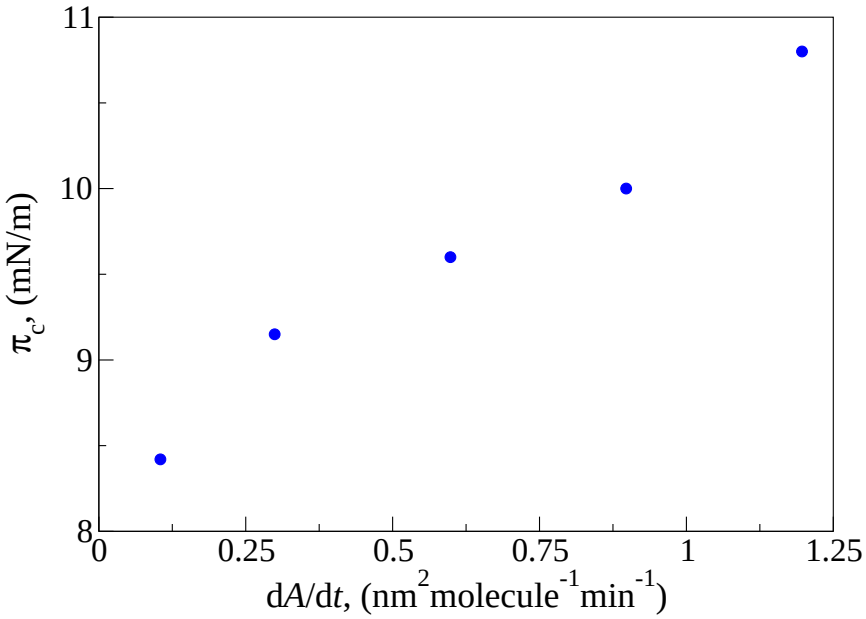

Figure 4.5: Variation of collapse pressure (π_c) as a function of compression rate (dA/dt) at a temperature of 298.15 K.

4.3.4 Effect of compression rate and temperature on the collapse of Langmuir monolayer

We have studied the effect of compression rate on the collapse of tp-dimer Langmuir monolayer. The monolayer was compressed at various rates from an A_m corresponding to the coexistence of gas and condensed phase. We find that with the increase in compression rate, the collapse pressure (π_c) increases. Figure 4.5 shows the variation of collapse pressure as a function of compression rate at a temperature of 25°C (298.15 K). Similar behavior was found in the monolayers of dicarboxylic acids [14]. The dependence of the collapse pressure on compression rate indicates that the monolayer is in a metastable state. This is also evident from the very low equilibrium spreading pressure of the material tp-dimer at air-water interface.

The effect of temperature on the collapse of Langmuir monolayer was studied from the $\pi - A_m$ isotherms. The $\pi - A_m$ isotherms were obtained for various temperatures by compressing the monolayer with a constant compression rate. We find that with the increase in temperature of monolayer the collapse pressure decreases. Figure 4.6 shows the variation of

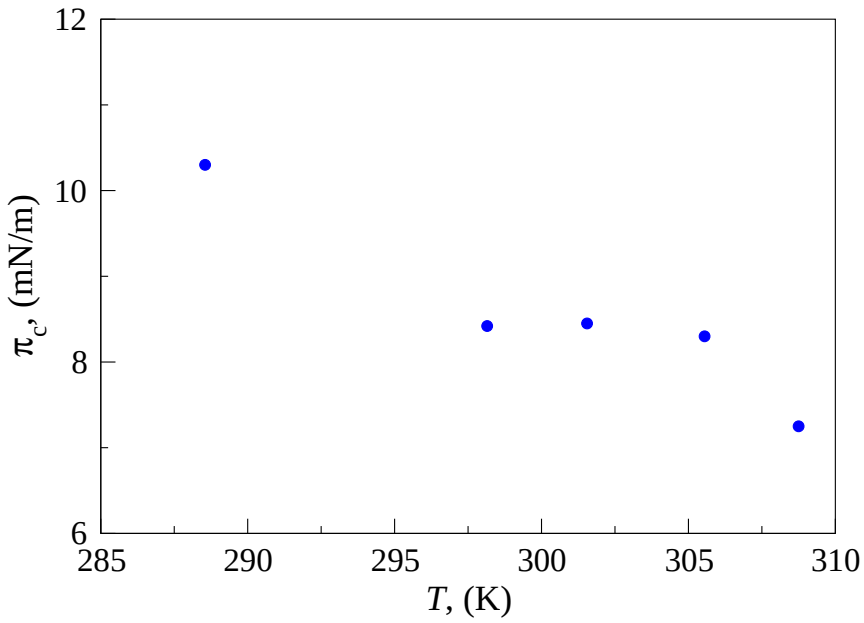

Figure 4.6: Variation of collapse pressure (π_c) as a function of temperature (T). Here the monolayer was compressed at a rate of 0.10 nm^{2}molecule^{-1}min^{-1}.

the collapse pressure as a function of temperature. Here the monolayer was compressed at a constant compression rate of 0.10 nm^{2}molecule^{-1}min^{-1}. Similar behavior has been reported in the Langmuir monolayers of systems like oligomers [15] and fluoroalkanes [16].

4.4 Discussion

The $\pi - A_m$ isotherm and BAM images suggest that the monolayer exhibited coexisting gas and liquid like phase at A_m greater than 1.80 nm^2. Below the A_m of 1.80 nm^2, the monolayer exhibited uniform phase before collapsing at 1.63 nm^2. The phase exhibited by the monolayer in the uniform region can be characterized by the compressional modulus $|E|$ of the monolayer. The $|E|$ value can be calculated from the $\pi - A_m$ isotherm using the relation,

$$|E| = A_m \left(\frac{\mathrm{d}\pi}{\mathrm{d}A_m} \right) \tag{4.1}$$

Here, $\mathrm{d}\pi/\mathrm{d}A_m$ is the change in surface pressure with area per molecule. In monolayers, the low density liquid phase has a maximum value of $|E|$ in the range 12.5 – 50 mN/m. The condensed phase of the monolayer has a maximum value of $|E|$ in the range 100 – 250

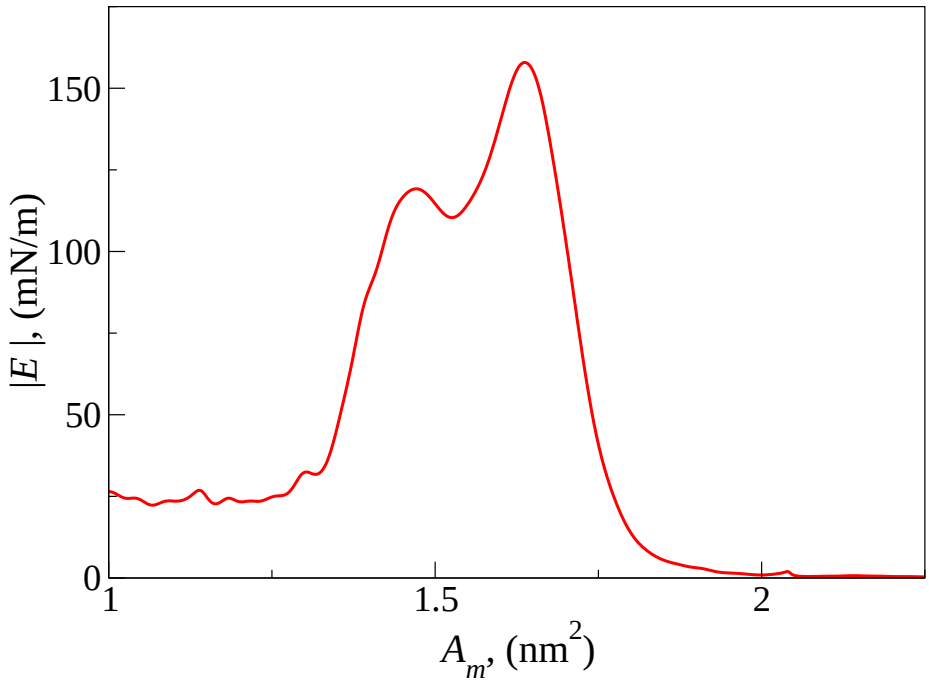

Figure 4.7: Compressional modulus $|E|$ as a function of area per molecule (A_m) for the tp-dimer monolayer at 15°C. The monolayer was compressed with a rate of 0.10 nm^{2}molecule^{-1}min^{-1}.

mN/m [16, 17]. Figure 4.7 shows the variation of $|E|$ as a function of A_m for the tp-dimer monolayer. Here, $|E|$ exhibits a maximum value of 157 mN/m at an A_m of 1.63 nm^2. This value of $|E|$ indicates that the uniform phase in the monolayer of tp-dimer corresponds to the condensed phase. From the $\pi - A_m$ isotherm, BAM and $|E|$ value, we infer that the monolayer (compression rate of 0.10 nm^{2}molecule^{-1}min^{-1}) exhibited coexistence of gas and condensed phase at large value of A_m (1.80 nm^2). Below the A_m of 1.80 nm^2, the monolayer exhibited uniform condensed phase and collapsed at an A_m of 1.63 nm^2 with a collapse pressure of 11.7 mN/m.

The estimated length of the molecules (using ChemDraw) was about 5 nm. If the molecules are stacked into columns due to $\Pi - \Pi$ interaction between the triphenylene moieties, the intermolecular distance in a column will be about 0.34 nm. Thus the estimated molecular area will be about 1.7 nm^2. Comparing this value with the $A_\circ$ value (1.75 nm^2), we infer that the molecules are in the edge-on configuration. Similar configuration of the molecules has been reported for the monolayer of triphenylene discotic molecule [18].

The equilibrium surface pressure (ESP) of the tp-dimer at air-water interface obtained by putting a speck of the crystallite on the water surface was about 0.1 mN/m. The very low ESP can be attributed to the weak hydrophilic group in the tp-dimer molecule which reduces the interaction between the subphase and the molecules. The cohesive forces between the molecules in the tp-dimer crystallite imposes an energy barrier for the molecules to go into the air-water interface from the 3D solid phase. If the surface tension of the subphase is not sufficient to overcome these cohesive forces, the molecules would prefer to stay in the 3D solid phase and the material exhibits low or zero ESP [19].

The AFM image of the LB film transferred onto a hydrophilic silicon substrate is analyzed to understand the molecular organization. The monolayer transferred at a surface pressure of 5 mN/m showed a film of uniform coverage. The line profile on the topography image yielded the thickness of the film to be about 1.5 nm. The estimated diameter of the triphenylene moiety (using ChemDraw) is about 1.6 nm. Hence the height obtained from the AFM topography image suggests that the triphenylene moieties in the molecules are in the edge-on configuration and the hydrophilic ester groups are anchored to the silicon substrate. Figures 4.8(a) and 4.8(b) show the molecular structure of the tp-dimer and the schematic diagram of the organization of molecules, respectively. The limiting area obtained from the $\pi - A_m$ isotherm indicates similar configuration of the molecules at an air-water interface. This configuration is favored as it maximizes the $\Pi - \Pi$ interaction between the triphenylene moieties. The film transferred at a surface pressure of 15 mN/m showed particles of height varying between 2 to 4 nm. This suggests that the film was transferred in a collapsed state. Surface manometry studies also indicated that the Langmuir monolayer collapses at an A_m of 1.63 nm^2.

The AFM image of the LB film transferred onto a hydrophobic silicon substrate showed the coexistence of droplets and film. On hydrophobic substrates two layers of the film will be transferred in one dipping cycle. The line profile on the topography image yielded the film thickness to be about 3.5 nm. This height corresponds to the bilayer thickness of the tp-dimer film. The height of the droplets obtained from the line profile varied between 5 to

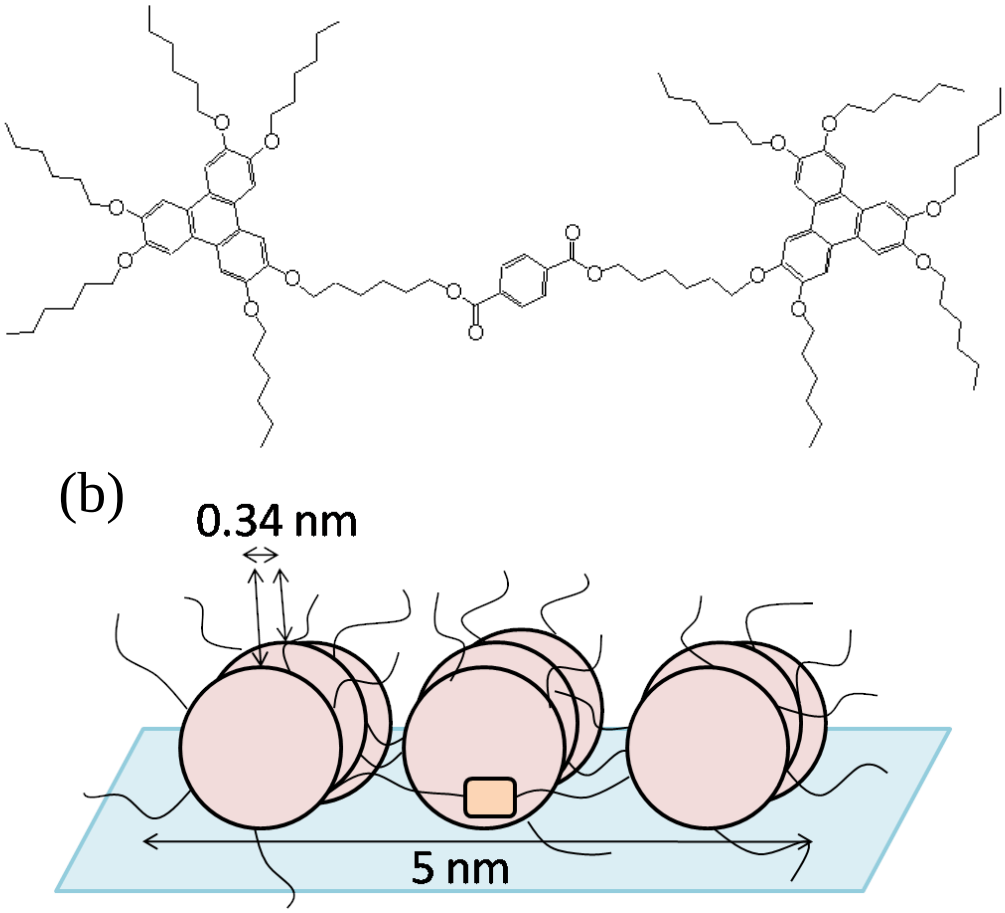

Figure 4.8: (a) Molecular structure of tp-dimer with length of the molecule according to standard bond lengths and angles. (b) Schematic diagram showing the organization of the tp-dimer molecules with the triphenylene moieties in the edge-on configuration. The estimated molecular area for this configuration is about 1.7 nm^2.

15 nm. The coexistence of droplets and bilayer film indicates that the bilayer film transferred onto the hydrophobic silicon substrate dewetted to form droplets. Similar behavior has been reported for azobenzene molecules [20] and it has been presented in chapter 2.

4.4.1 Effect of compression rate on the collapse pressure

We have studied the effect of compression rate on the collapse pressure of the metastable monolayer. The collapse process can be considered as the relaxation of the monolayer under stress. On compressing the monolayer the stress in the monolayer increases. At collapse pressure, the monolayer relaxes by the formation of multilayers or 3D crystallites, wherein the molecules go into the third dimension. The relaxation time for the monolayer depends on the molecular processes involved in the collapse process. If the relaxation time is of the order of or greater than the time of observation (inverse of compression rate), the monolayer will be compressed to high surface pressures before it collapses. Hence the collapse pressure increases with increase in compression rate [21] for metastable monolayers. Our studies on the tp-dimer also showed increase in the collapse pressure as the compression rate is increased.

In our case, during the collapse, the monolayer breaks down to form 3D crystallites. We find that on expansion, the collapsed state was not reversible to the monolayer state. Hence, the transformation from the condensed phase monolayer to the three dimensional crystallites during the collapse is similar to the transformation from elastic region to the plastic region in bulk materials [13]. With this analogy, Kampf *et al.* [6] suggested that the surface pressure can be identified as the monolayer stress. The molecular area in the monolayer can be related to the monolayer strain (α) by the expression, $\alpha = 1 - (A/A_i)$, where, A is the molecular area at time t and A_i is the initial molecular area. The strain rate (α_t) obtained from the above expression is given by the relation,

$$\alpha_t = -\frac{1}{A_i}\frac{\mathrm{d}A}{\mathrm{d}t} \tag{4.2}$$

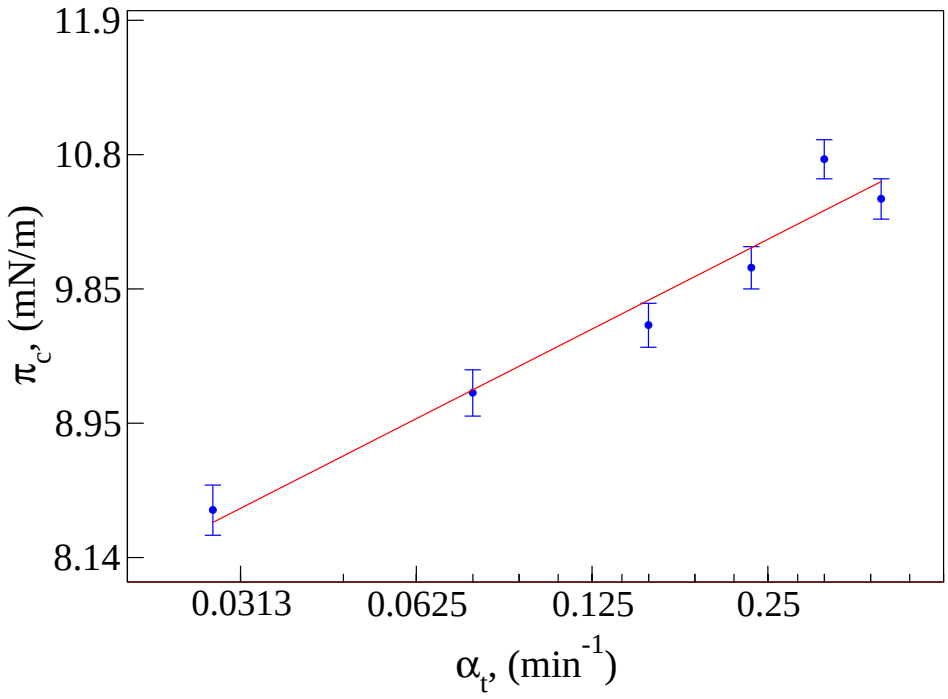

Figure 4.9: Variation of collapse pressure (π_c) as a function of strain rate (α_t) at 298.15 K (25°C). Both *X* and *Y* axes are in logarithmic scale. The solid line represents the power law fit ($\pi_c = C_1\alpha_t^{1/n}$) to the data points. The fit parameter yields the value of *n* to be 11.14. The error involved in the surface pressure data are indicated.

Here (d*A*)/(d*t*) is the compression rate. The strain rate can be calculated from the compression rate using equation 4.2. The A_i value is obtained from the lift off area (i.e., onset of the uniform condensed phase) in the $\pi - A_m$ isotherm. Figure 4.9 shows the variation of collapse pressure as a function of strain rate at a temperature of 25°C (298.15 K). We find that the data can be fitted with a power law [6] given by the equation,

$$\pi_c = C_1\alpha_t^{1/n} \tag{4.3}$$

Here C_1 is constant at a given temperature.

The value of *n* calculated from the fit was about 11.14. In our system, the monolayer does not exhibit a plastic flow region (a plateau region after the monolayer collapse in the $\pi - A_m$ isotherm). In literature, the power law relation between the collapse pressure and strain rate has been reported in the Langmuir monolayers of dendrimer [6] and alkanethiol [13]

which exhibit the plastic flow region. We find that the value of n obtained for tp-dimer is of the same order as that reported for the dendrimer and alkanethiol monolayers ($n \approx 13$). In bulk, similar power law relation between strain rate and shear stress has been reported for polymers [12, 22], where the constant C_1 is called the *consistency* and n is called power-law index. The deformation mechanism for linear polymers in the plastic flow region is known and the power law relation can be attributed to the nature of deformation mechanism. The insufficient experimental evidence to determine the nature of collapse in the monolayer makes it difficult to understand the power law relation between the strain rate and collapse pressure for the case of Langmuir monolayer [6]. Hence, our study of power law relation in the absence of plastic flow region is important.

4.4.2 Effect of temperature on the collapse pressure

In the tp-dimer monolayer, we find that the collapse pressure decreases with increase in temperature when the monolayer is compressed with a fixed strain rate. For the monolayers of dendrimers [6] and alkanethiol [13] molecules, it has been reported that the strain rate shows an Arrhenius temperature dependence. We have analyzed our experimental data by considering the strain rate to have Arrhenius temperature dependence of the form $\alpha_t \propto \exp\{-\varepsilon/(RT)\}$ [13], where ε is the activation energy for the collapse of monolayer, R is the universal gas constant and T is the absolute temperature. With this assumption, rearranging equation 4.3 and by adding the temperature dependence of the strain rate, we get the following:

$$\alpha_t = C_2 \pi_c^n \exp\left(-\frac{\varepsilon}{RT}\right) \tag{4.4}$$

Here, C_2 is a constant. In order to get the value of ε, equation 4.4 is linearized and rearranged to get the following expression,

$$ln(\pi_c) = \frac{1}{n} ln(C' \alpha_t) + \frac{\varepsilon}{nRT} \tag{4.5}$$

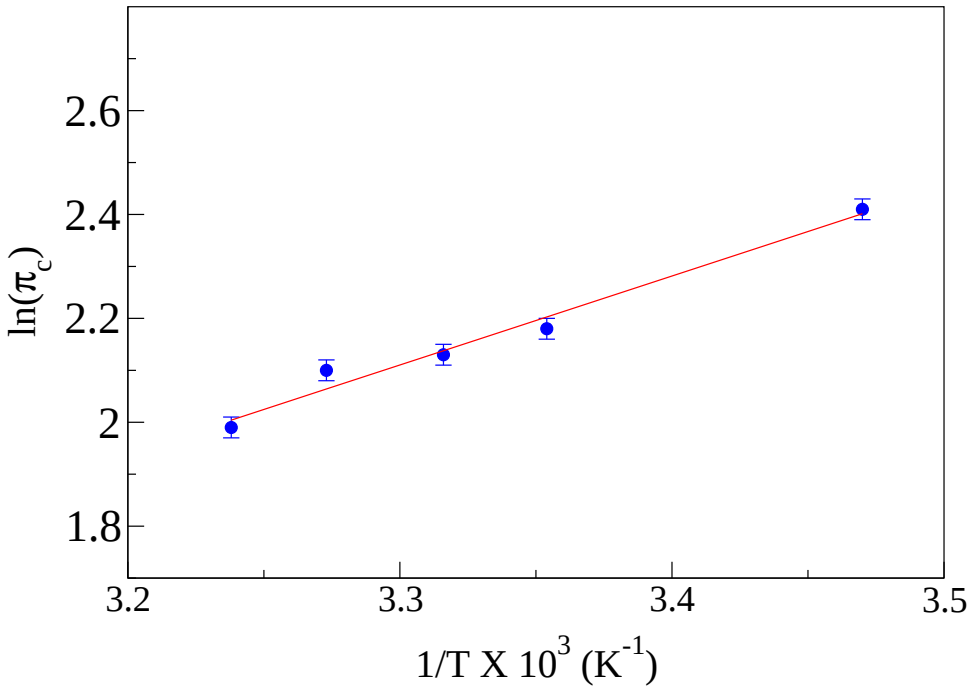

Figure 4.10: Variation of $\ln(\pi_c)$ as a function of $1/T$. The monolayer was compressed at a rate of 0.10 $nm^2 molecule^{-1} min^{-1}$. Solid line represents the straight line fit to the data points. The slope of the line (ε/nR), was about 1.71×10^3.

Here, C' is a constant. The variation of $\ln(\pi_c)$ as a function of $1/T$ yields a straight line. From the slope ε/nR, we can obtain the activation energy (ε) for the collapse of monolayer. Figure 4.10 shows the variation of the $\ln(\pi_c)$ as a function of $1/T$. The data points are fitted to a straight line. The activation energy obtained from the slope of the straight line was equal to 158.6 kJ/mol. The activation energy is the measure of energy required for the molecules in the 2D monolayer to escape into the third dimension. The activation energy reported for the monolayer of dendrimer and alkanethiol were 596 kJ/mol [6] and 108 kJ/mol [13], respectively. The ε value depends on many factors like interaction between the amphiphilic molecules, their interaction with the subphase and the mechanism of the collapse.

Studies on the alkanethiol monolayer at air-water interface showed Arrhenius temperature dependence of strain rate at high temperatures and non-Arrhenius temperature dependence of strain rate at low temperatures [13]. In our system, the Arrhenius temperature dependence was found throughout the temperature range studied as in the case of Langmuir

monolayer of dendrimers [6].

4.5 Conclusions

The novel dimer of disk shaped triphenylene moieties (tp-dimer) spreads at air-water interface to form a monolayer. Surface manometry and BAM studies indicated that the monolayer exhibited coexistence of gas and condensed phase at A_m greater than 1.80 nm^2. In between the A_m of 1.80 – 1.63 nm^2 the monolayer exhibited uniform condensed phase. At 1.63 nm^2 the monolayer collapsed. The limiting area value (1.75 nm^2) obtained from the isotherm suggests that the triphenylene moieties in the molecule are in the edge-on configuration at air-water interface. The monolayer film transferred onto a hydrophilic silicon substrate in the condensed phase was studied using AFM. The line profile on the topography image showed the height of the film to be 1.5 nm which is close to the value of the diameter of the triphenylene moiety. This indicates that the triphenylene moieties of the molecule are in the edge-on configuration on the hydrophilic substrate. The AFM studies of the LB film transferred onto a hydrophobic silicon substrate showed a coexistence of bilayer film with droplets of size varying between 5 – 15 nm. This indicated that the bilayer film on the hydrophobic silicon substrate dewetted to form droplets.

We find that the collapse pressure of the tp-dimer monolayer increases with increase in compression rate at a given temperature. Our analysis of the experimental data showed that the strain rate is related to the collapse pressure by a power law. Our studies on the effect of the temperature on the collapse showed that the collapse pressure decreases with increase in temperature. We have analyzed the data by using the bulk constitutive equations and assuming the Arrhenius temperature dependence of the strain rate. Our analysis yielded an activation energy of 158.6 kJ/mol for the collapse of the monolayer.

Bibliography

[1] G. Roberts, *Langmuir-Blodgett Films*, Plenum Press: New York and London, (1990).

[2] E. Hatta, and T. M. Fischer, *J. Phys. Chem. B* **106**, 589 (2002).

[3] C. Ybert, W. Lu, G. Möller, and C. M. Knobler, *J. Phys. Chem. B* **106**, 2004 (2002).

[4] A. Gopal, Ka. Lee, and C. Yee. *J. Phys. Chem. B* **110**, 22079 (2006).

[5] T. Maruyama, J. Lauger, G. G. Fuller, C. W. Frank, and C. R. Robertson, *Langmuir* **14**, 1836 (1998).

[6] J. P. Kampf, C. W. Frank, E. E. Malmström, and C. J. Hawker, *Science* **283**, 1730 (1999).

[7] J. Y. Josefowicz, N. C. Maliszewskyj, S. H. J. Idziak, P. A. Heiney, J. P. McCauley Jr., and A. B. Smith III, *Science* **260**, 323(1993).

[8] A. Nayak, K. A. Suresh, S. K. Pal, and S. Kumar. *J. Phys. Chem. B* **111**, 11157 (2007).

[9] A. D. F. Dunbar, T. H. Richardson, A. J. McNaughton, J. Hutchinson, and C. A. Hunter, *J. Phys. Chem. B* **110**, 16646 (2006).

[10] J. P. Schmidtke, and R. H. Friend, *J. Chem. Phys.* **124**, 174704 (2006).

[11] W. J. Evans, and G. F. Harrison, *J. Mater. Sci.* **18**, 3449 (1983).

[12] L. E. Govaert, C. W. M. Bastiaansen, and P. J. R. Leblans, *Polymer* **34**, 534 (1993).

[13] P. Burriel, J. Claret, J. Ignes-Mullol, and F. Sagues, *Eur. Phys. J. Special Topics* **143**, 165 (2007).

[14] P. M. Jeffers, and J. Daen, *J. Phys. Chem.* **69**, 2368 (1965).

[15] J. Deng, J. R. Hottle, J. T. Polidan, H-J. Kim, C. E. Farmer-Creely, B. D Viers, and A. R. Esker, *Langmuir* **20**, 109 (2004).

[16] M. Broniatowski, S. I. Macho, J. Minones, Jr., and P. Dynarowicz-Latka, *J. Phys. Chem. B* **108**, 13403 (2004).

[17] D. J. Dervichian, *J. Chem. Phys.* **7**, 932 (1939).

[18] V. V. Tsukruk, H. Bengs, and H. Ringsdorf, *Langmuir* **12**, 754 (1996).

[19] J. J. Bikerman, *Kolloid-Zeitschrift und Zeitschrift fur Polymere* **201**, 48 (1964).

[20] Bharat Kumar, A. K. Prajapati, M. C. Varia, and K. A. Suresh, *Langmuir* **25**, 839 (2009).

[21] T. Kato, *Langmuir* **6**, 870 (1990).

[22] J. M. G. Cowie, and V. Arrighi, *Polymers: Chemistry and Physics of modern materials* CRC Press, Taylor and Francis Group (2008).

Chapter 5

Direct to injection tunneling transition in the Langmuir-Blodgett film of a novel star shaped liquid crystalline oligomer

5.1 Introduction

Organic materials with electron rich and electron deficient groups are interesting because of their unique electrical properties [1, 2]. Thin films of these materials find technological applications in the field effect transistors, light-emitting diodes and photovoltaic devices [3, 4]. For such applications, the molecules must be well ordered in thin film [5], since the structure and morphology of the film are important in fabricating the devices. The Langmuir-Blodgett (LB) technique is a convenient method to prepare thin film of organic molecules with good ordering and orientation [6]. Molecular ordering can also be obtained by the process of self organization. Combination of the phenomenon of self organization along with the LB technique can give well oriented and highly ordered thin films [7]. In this context, the amphiphilic discotic molecules are interesting, since the $\Pi - \Pi$ stacking of the disk shaped cores in the LB film can result in the formation of two dimensional anisotropic structures [8, 9]. The LB film of discotic molecules with different cores like anthraquinone [4], triphenylene [10, 11, 12] and phthalocyanine [13] have been studied. The anthraquinone moiety is electron deficient

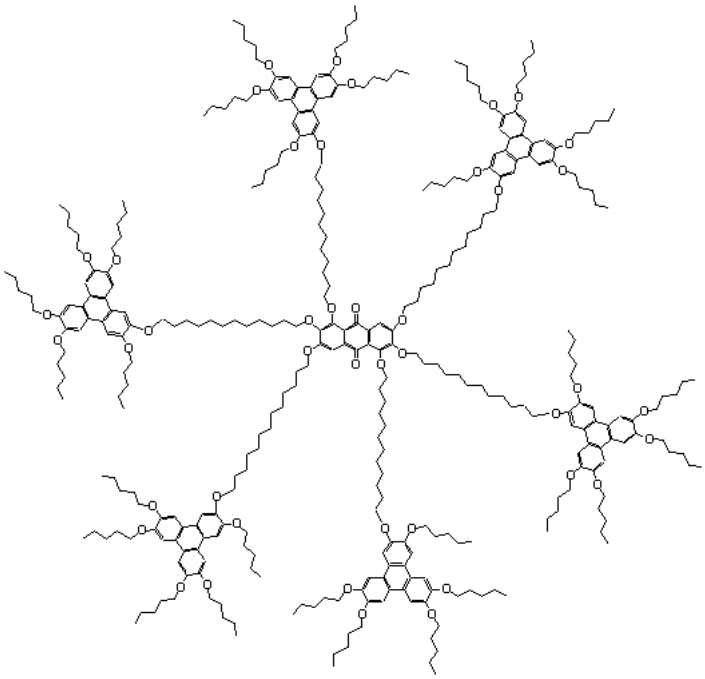

Figure 5.1: Chemical structure of AQD6 molecule. The anthraquinone core is connected to six triphenylene moieties by dodecyloxy chain through ether linkage. The triphenylene is substituted with five pentyloxy chains.

whereas the triphenylene moiety is electron rich.

We have studied the Langmuir monolayer and LB films of a star shaped liquid crystalline oligomer made up of disk shaped moieties, hexatriphenylene substituted anthraquinone (AQD6). Figure 5.1 shows the structure of the AQD6 molecule. The molecule has a central core of electron deficient anthraquinone which is connected to six disk shaped, electron rich triphenylene moieties by flexible alkyl chains. These molecules with electron rich and electron deficient moieties, can have interesting electrical properties when organized in thin film. The limiting area obtained from the surface pressure-area per molecule isotherm and the AFM topography images of the LB film suggest that the anthraquinone moiety is in face-on configuration on the substrate and the triphenylene moieties are extended away from the substrate in edge-on configuration. We have studied the nanoscale electrical conductivity of the LB film on a gold coated silicon substrate using a current sensing atomic force microscope (CSAFM). The monolayer film between AFM cantilever tip and substrate forms a metal-film-metal junction, where the monolayer film introduces a potential barrier for the

electron transfer. Our analysis of the current (I)-voltage (V) characteristics indicated that the current flow across the junction is through electron tunneling. Further, as the bias voltage is increased gradually, we find a transition in the tunneling mechanism, from direct tunneling to injection tunneling, which is also known as Fowler-Nordheim tunneling.

5.2 Experiment

The material AQD6 was synthesized by Sandeep Kumar and H. K. Bisoyi [14]. It was purified by repeated column chromatography and the purity was better than 99% as indicated by NMR, IR and elemental analyzer techniques. The Langmuir monolayer film at air-water interface was studied by surface manometry and Brewster angle microscopy (BAM). The surface manometry studies were carried out using a Nima trough (Model: 611M). Ultrapure deionized water of resistivity greater than 18 MΩcm (millipore water, MilliQ) and pH 5.7 was used as subphase. The AQD6 solution in chloroform (concentration=0.1 mg/ml) was used as spreading solution. The monolayer was compressed at a rate of about 22 $Å^2 molecule^{-1} min^{-1}$. The experiments were carried out at a temperature of 24.0 ± 0.1°C. The BAM studies were carried out using MiniBAM (NFT, Nanotech).

The LB film of AQD6 molecules was prepared by transferring the monolayer onto different solid substrates like mica, hydrophilic silicon and gold coated silicon. The mica sheet was freshly cleaved before the transfer of the film. To obtain hydrophilic silicon substrates, the polished silicon wafers were treated with boiling piranha solution (3 : 1 ratio of concentrated sulphuric acid and hydrogen peroxide) for about 5 min. The transfer of the monolayer was carried out at a surface pressure of 4 mN/m, with a dipping speed of 2 mm/min. Mica sheet, hydrophilic silicon and gold coated silicon are hydrophilic substrates and one layer of the film will be transferred onto them in one dipping cycle (consisting of one downstroke and one upstroke). The transfer of the film occurred during upstroke. Surface morphology and thickness of the LB film were obtained from the atomic force microscope (AFM) studies (Model:PicoPlus, Molecular Imaging). The film was scanned in the acoustic AC mode using

silicon cantilevers of average resonance frequency 175 kHz and spring constant of 31 N/m.

The nanoscale electrical conductivity of the AQD6 monolayer on a gold coated silicon substrate was studied using CSAFM. An advantage of CSAFM is that it provides a simple method to study the metal-molecule-metal junction. Another advantage of using CSAFM is that it gives simultaneous topography and current images which can be correlated to understand the electrical properties of thin film. Platinum coated silicon cantilevers with a spring constant in the range of 0.02 – 0.8 N/m were used. The tip radius was about 30 nm. The conducting tip and the gold coated silicon substrate act like two metal electrodes separated by the AQD6 monolayer film. The bias voltage was applied to the substrate and the tip was kept at virtual ground. A preamplifier with an operational range of 1 pA to 10 nA was connected to the tip to measure the current. The noise level in our system was about 10 pA and a current higher than this value was measurable. The film was scanned in the contact mode with a constant force and the topography and current images were acquired simultaneously. The force applied by the tip on the film and the bias voltage values were suitably chosen so that the film does not get damaged during the scan. The $I - V$ characteristics were obtained by holding the tip over the desired position on the film. During $I - V$ measurements, the feed back loop was enabled to keep the force between the tip and film at a fixed value. All the measurements were carried out in ambient conditions at a temperature of 25°C and relative humidity of ~ 30%.

5.3 Results

The material AQD6 was studied under a polarizing microscope. The material, a room temperature mesophase melts to isotropic phase on heating to 123°C. On cooling from isotropic phase, the sample transformed to a mesophase at 116°C and continued to be in the mesophase till about 15°C. The X-ray characterization of the mesophase indicated that the molecules are stacked one above the other to form a hexagonal columnar phase, usually observed in the discotic liquid crystals [14].

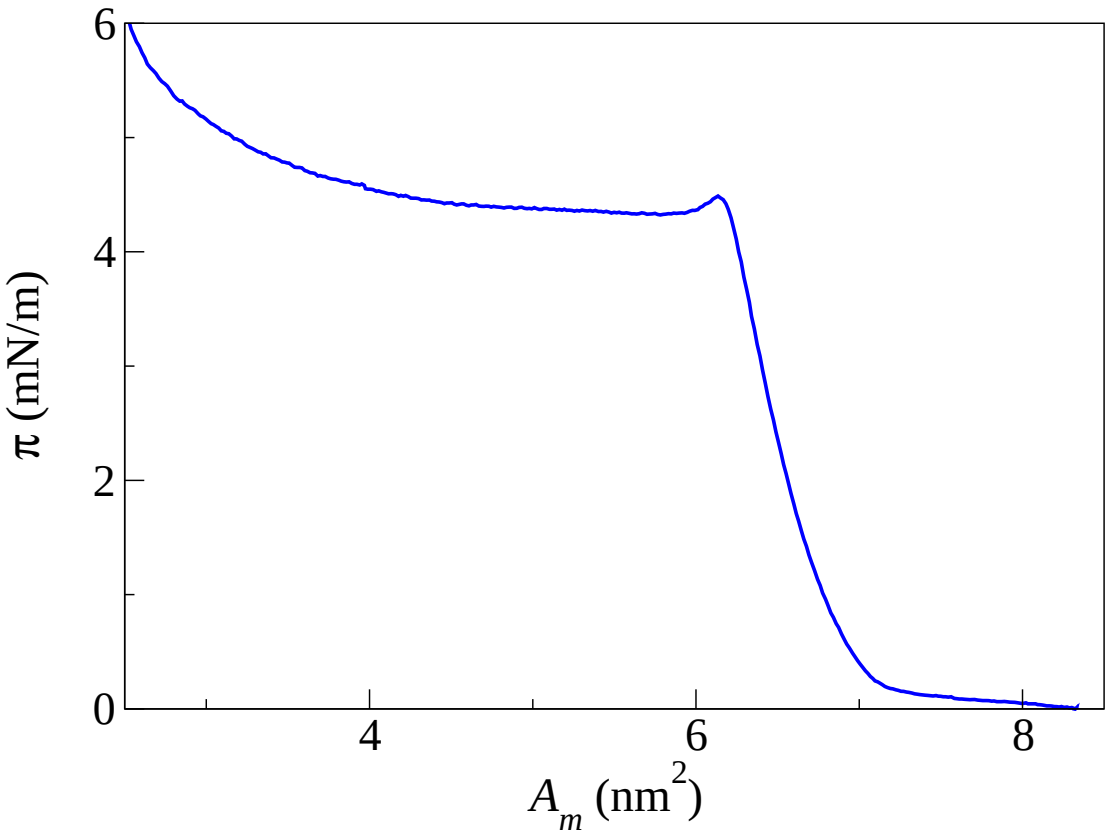

Figure 5.2: Surface pressure (π)−area per molecule (A_m) isotherm of the AQD6 monolayer at air-water interface at a temperature of 24.0 ± 0.1°C.

5.3.1 Surface manometry

Surface manometry studies showed that the material AQD6 forms a stable monolayer at air-water interface. Surface pressure (π)−area per molecule (A_m) isotherm of the AQD6 monolayer at air-water interface is shown in Figure 5.2. At large A_m the isotherm shows zero surface pressure. On compression, around 7.0 nm^2 the π value sharply increases. At an A_m of 6.2 nm^2, the monolayer collapsed with a collapse pressure of about 4.3 mN/m. The stability of the monolayer was checked by holding the barriers at a constant A_m and monitoring the π as a function of time. We find the monolayer to be stable for A_m values above 6.2 nm^2. The limiting area per molecule $A_\circ$, which gives the area occupied by the molecule in the monolayer, was 6.8 nm^2.

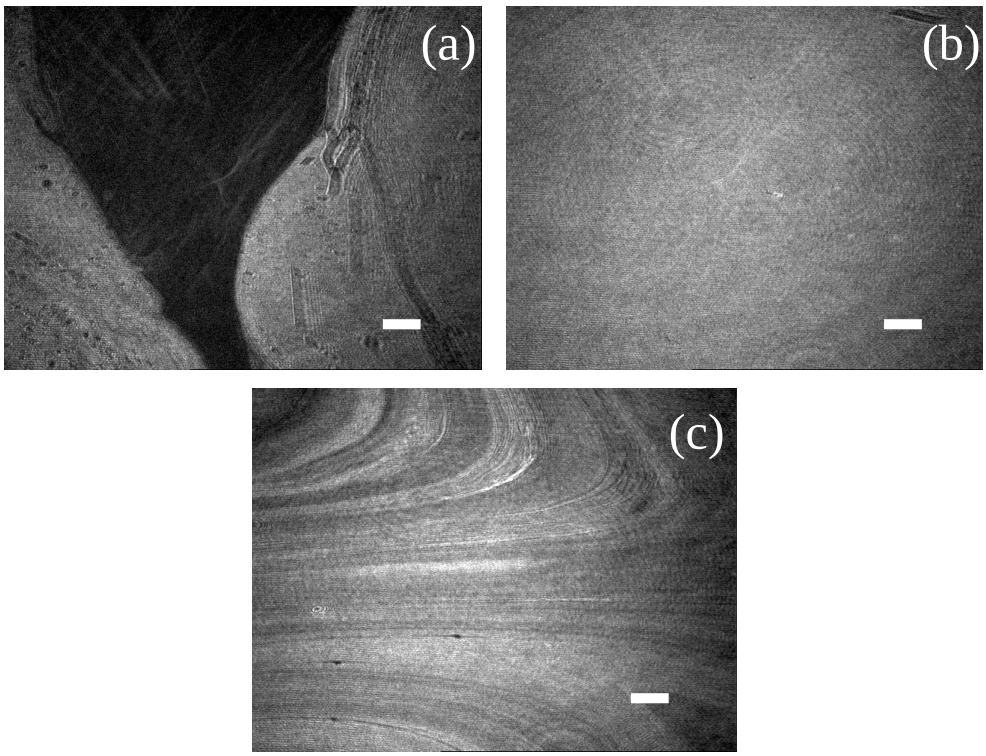

Figure 5.3: BAM images of the AQD6 monolayer at different area per molecule. (a) Shows coexistence of gas (dark region) and low density liquid (L_1) phase (grey region) at A_m = 7.60 nm^2. (b) Shows uniform L_1 phase at A_m = 6.65 nm^2. (c) Shows the collapsed state (bright striations in the grey background) at A_m = 4.40 nm^2. The scale bar in each image represents 500 μm.

5.3.2 Brewster angle microscopy

The BAM studies showed the phases exhibited by the AQD6 monolayer at different A_m values (Figure 5.3). Figure 5.3(a) represents the BAM image at large A_m showing the coexistence of dark and grey regions. Between A_m values of 7.0 nm^2 and 6.2 nm^2, the monolayer exhibited uniform phase (Figure 5.3(b)). On further compression, the monolayer collapsed exhibiting bright striations in the grey background (Figure 5.3(c)).

5.3.3 Atomic force microscopy

The LB films of AQD6 monolayer on the solid substrates of mica and hydrophilic silicon were studied using AFM in the acoustic AC mode. The transfer ratio of the film on a hydrophilic mica substrate was about 85%. Figure 5.4 shows the AFM topography image of

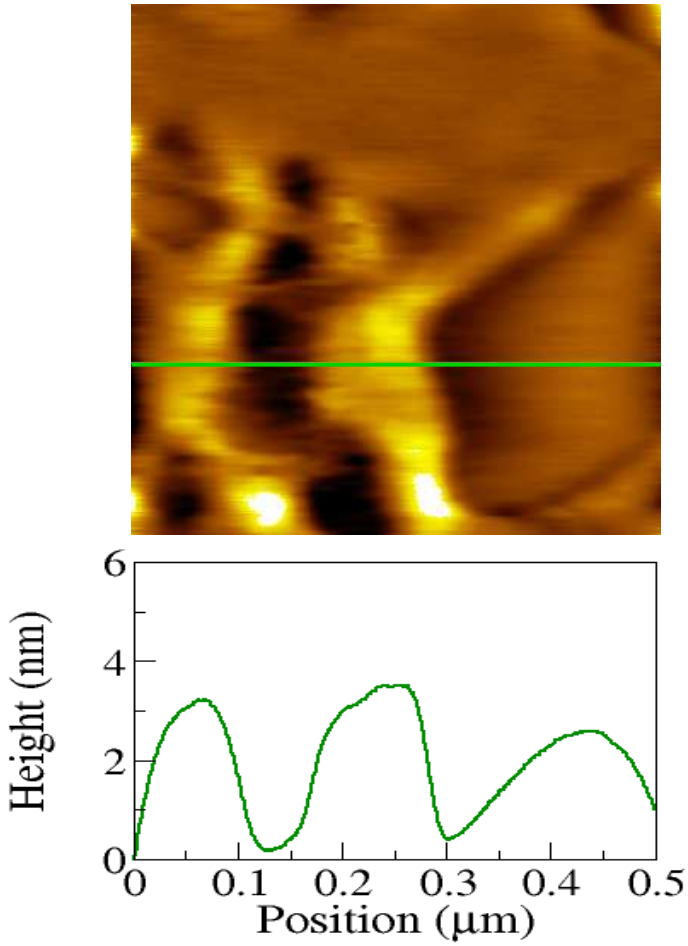

Figure 5.4: AFM topography image of AQD6 monolayer on a hydrophilic mica substrate. Here the film was transferred at a surface pressure of 4 mN/m. The image was obtained in the acoustic AC mode. The line profile on the image yields an average height of 3.4 nm.

the monolayer LB film on the mica substrate. The line profile over the film in the topography image yielded a height of 3.4 nm.

The AQD6 monolayer film transferred onto a hydrophilic silicon, had the transfer ratio of about 70%. Figure 5.5 shows the AFM topography image of the LB film on the silicon substrate. The line profile on the topography image yielded a height of about 3.4 nm.

5.3.4 Electrical conductivity using current sensing AFM

The ability of the CSAFM to simultaneously get surface topography and electrical conductivity makes it a convenient tool for studying thin film properties. We have employed this technique to study the electrical conductivity of the AQD6 monolayer transferred onto a gold

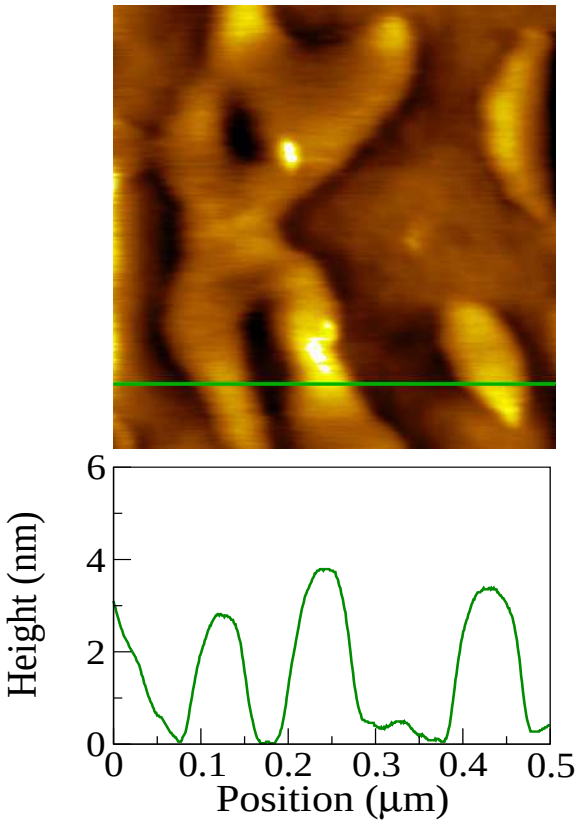

Figure 5.5: AFM topography image of AQD6 monolayer on a hydrophilic silicon substrate. Here the film was transferred at a surface pressure of 4 mN/m. The image was obtained in the acoustic AC mode. The line profile on the image yields an average height of 3.4 nm.

coated silicon substrate. The AQD6 monolayer film between the tip and the substrate forms metal-film-metal junction. Positive bias voltage of 0.4 V was applied to the substrate and the tip was kept at virtual ground. The film was scanned in the contact mode with a constant force of 3 nN. Figure 5.6 shows the topography and the corresponding current images. The height of the film measured from the line profiles drawn on the topography image was about 3.4 nm. Figure 5.6(b) shows the current image of the film. In regions without the film, the line profiles show high current value. In the regions covered with the film, the average current obtained from the line profile was about 1.5 nA.

We have carried out the $I-V$ measurements by keeping the conducting tip in contact with the film with a constant force of 3 nN. The tip was kept at a virtual ground and the voltage ramp of -1.0 V to $+1.0$ V was applied to the gold coated silicon substrate with a scan rate of 1 Hz. Figure 5.7 shows a typical $I-V$ curve. At low voltages, the current gradually increased and at high voltages there was a rapid increase in the current. The forward and the reverse bias had a small current offset of about $20-25$ pA at zero voltage.

5.4 Discussion

Surface manometry and BAM studies indicated that the monolayer exhibited coexistence of gas and liquid phase at A_m greater than 7.0 nm^2. Between the A_m of 7.0 nm^2 and 6.2 nm^2 the monolayer was in a uniform phase and it collapsed at an A_m of 6.2 nm^2 with a collapse pressure of 4.3 mN/m. The uniform phase exhibited by the monolayer can be characterized by calculating the compressional modulus ($|E|$) using the relation,

$$|E| = A_m \frac{\mathrm{d}\pi}{\mathrm{d}A_m} \tag{5.1}$$

Here, $\mathrm{d}\pi/\mathrm{d}A_m$ is the variation of π as a function of A_m. Figure 5.8 shows the variation of $|E|$ as a function of A_m. The compressional modulus has a maximum value of 32 mN/m, which corresponds to low density liquid (L_1) phase of the monolayer [15, 16]. Hence, from the $\pi - A_m$ isotherm, $|E|$ value and BAM images, we infer that above an A_m of 7.0 nm^2,

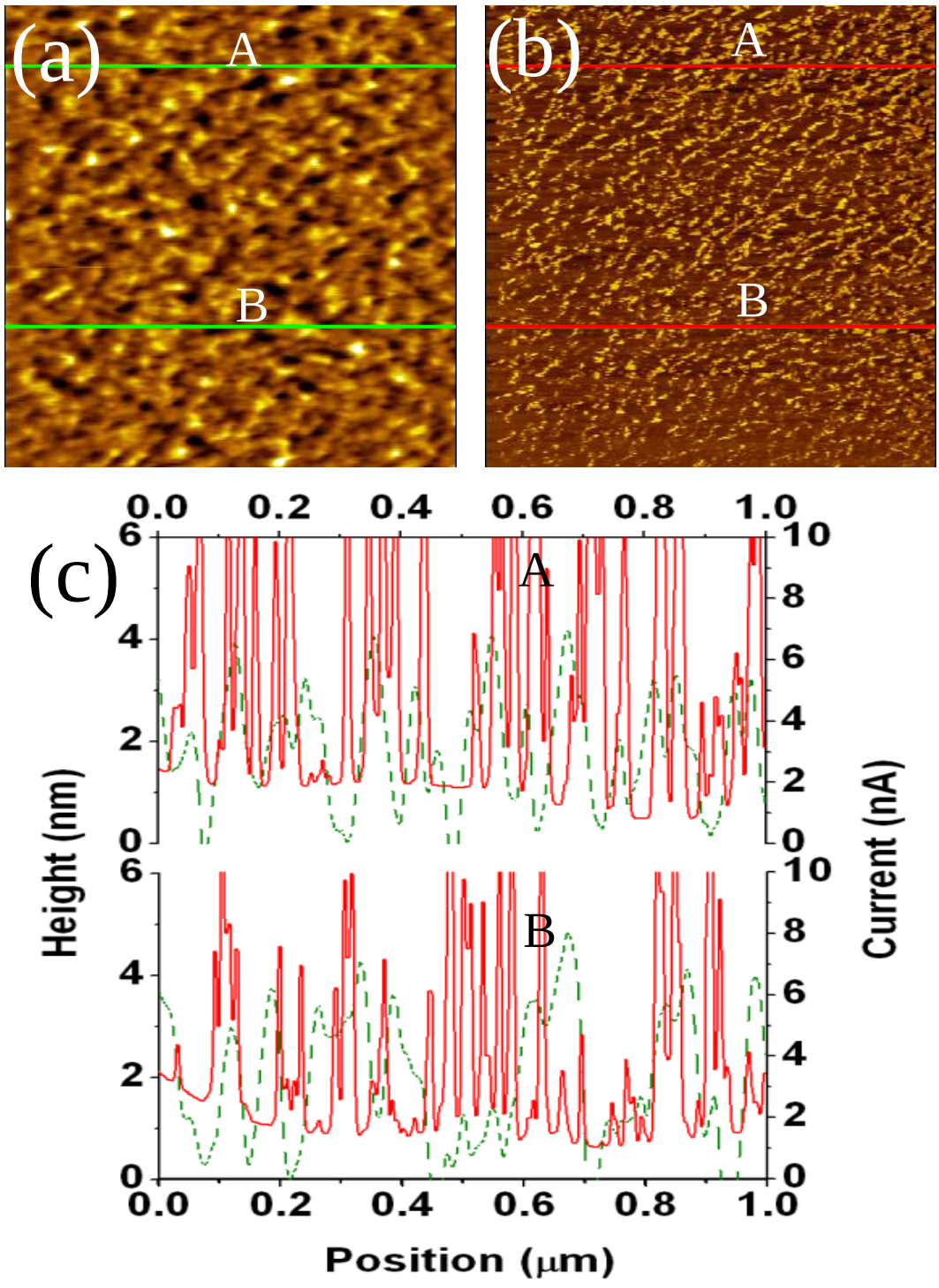

Figure 5.6: CSAFM images of AQD6 monolayer transferred onto a hydrophilic gold coated silicon substrate. Here the film was transferred at a surface pressure of 4 mN/m. The film was scanned in the contact mode with a constant force of 3 nN. Positive bias of 0.4 V was applied to the substrate. (a) Shows the topography image. (b) Shows the current image. (c) Shows the line profiles on the topography (dotted line) and current images (solid line) at two positions, A and B. The line profile on the topography image yields an average height of 3.4 nm for the film. The line profile on the current image yields an average current of 1.5 nA in the region covered with the film.

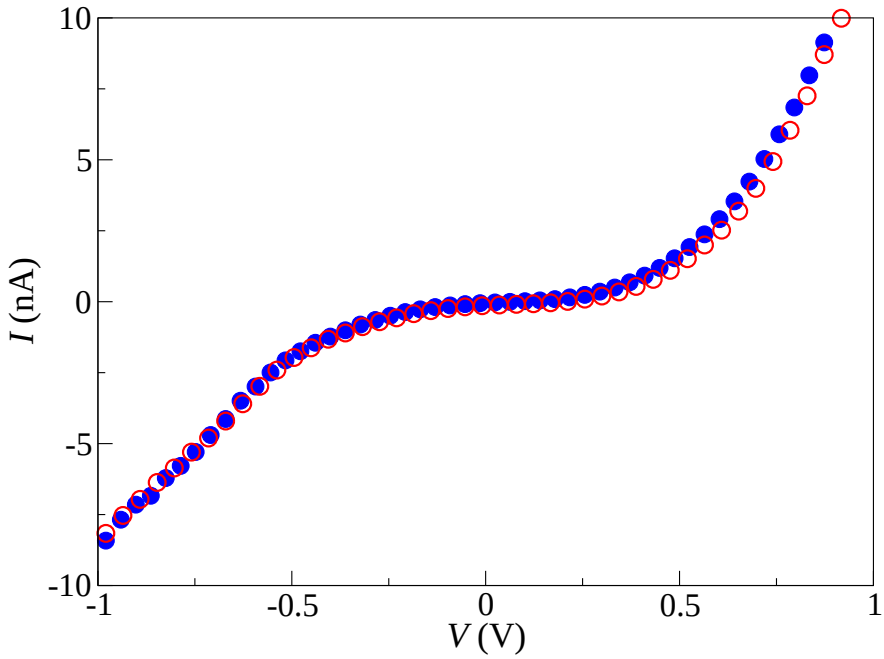

Figure 5.7: Typical $I - V$ characteristics of the AQD6 monolayer film on a hydrophilic gold coated silicon substrate. The tip was held at virtual ground and a voltage ramp was applied to the substrate with a scan rate of 1 Hz. The filled circles represent forward voltage scan and the open circles represent reverse voltage scan.

the monolayer exhibited coexisting gas and L_1 phase and between 7.0 nm^2 and 6.2 nm^2 it exhibited a uniform L_1 phase.

The LB film of the AQD6 monolayer transferred onto substrates of hydrophilic mica and hydrophilic silicon at a surface pressure of 4.0 mN/m is studied using an AC mode AFM. The line profile on the topography image of the AQD6 film on hydrophilic mica substrate shows domains of height 3.4 nm. The length of the triphenylene moiety substituted with the alkyl chains (pentyl chain) is estimated (using ChemDraw) to be about 2.0 nm. The length of the alkyl chains (dodecyl chain) connecting the triphenylene moieties with the anthraquinone core is estimated to be 1.2 nm. Thus, the total length of triphenylene moiety and alkyl chains is expected to be about 3.2 nm. This value is close to the height of the domains obtained from the AFM topography image. Hence we suggest that the anthraquinone moiety is in face-on configuration on the substrate and all the triphenylene moieties are extended away from the substrate in edge-on configuration. Similar conformation of the molecules has been reported for the Langmuir monolayer of molecules with electron rich triphenylene core connected to

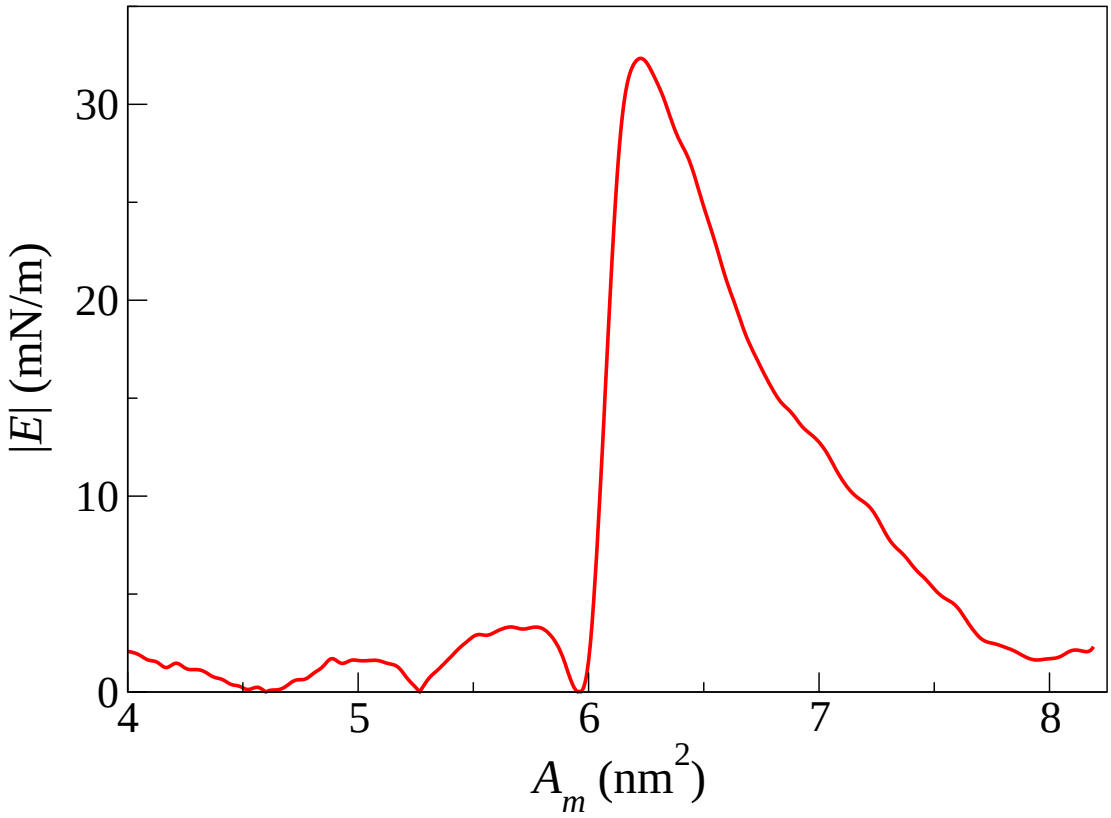

Figure 5.8: Variation of compressional modulus ($|E|$) as a function of area per molecule (A_m). The maximum value of $|E|$ is about 32 mN/m at A_m of 6.2 nm^2. This value of $|E|$ corresponds to a low density liquid (L_1) phase of the monolayer.

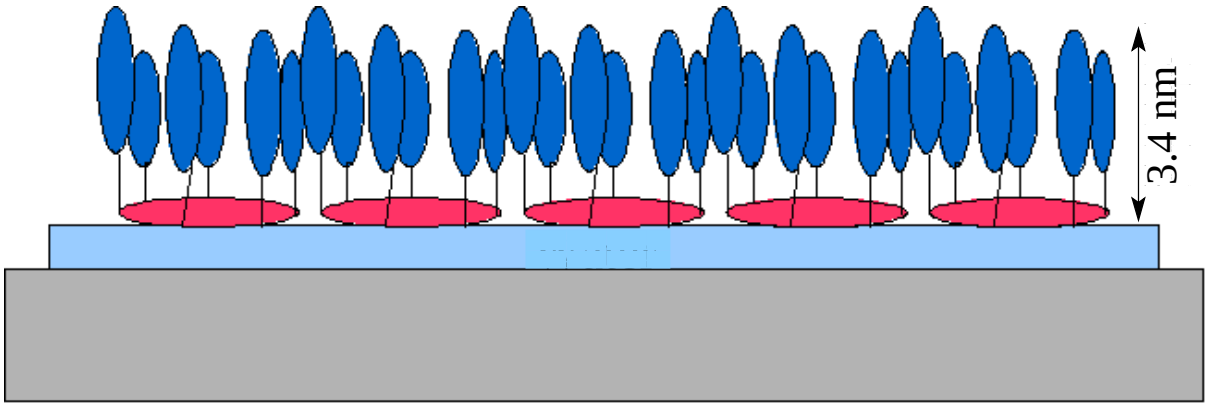

Figure 5.9: Schematic diagram showing the organization of AQD6 molecules on silicon substrate. The anthraquinone moiety (red disks) of the molecule is in face-on configuration and the six triphenylene moieties (blue disks) attached to it by alkyl chains (dodecyl chain) are in edge-on configuration.

six triphenylene moieties [12]. The monolayer film transferred at lower surface pressures and different dipping speeds also showed similar features.

The AFM images of the LB film transferred onto a hydrophilic silicon substrate also showed similar features. The line profile on the topography image yielded a height of about 3.4 nm. This suggests that the molecular conformation on the silicon substrate is similar to that on the mica substrate with anthraquinone moiety in face-on configuration and triphenylene moieties in edge-on configuration. Figure 5.9 shows the schematic diagram of the organization of molecules on hydrophilic solid substrates.

In the AQD6 monolayer, the hydrophilic anthraquinone moiety is expected to anchor the molecules at the air-water interface. The area occupied by the AQD6 molecule at air-water interface can be considered to be the area of an assembly of six edge-on triphenylene moieties [12]. The limiting area of an edge-on triphenylene unit in the Langmuir monolayer is about 1.1 nm^2 [10, 17]. Hence the area occupied by the assembly of six edge-on triphenylene moieties will be about 6.6 nm^2. This value is close to the limiting area ($A_\circ$ = 6.8 nm^2) of the AQD6 molecule obtained from the $\pi - A_m$ isotherm. Hence the molecules at air-water interface would be organized with their anthraquinone moieties in face-on configuration and the six triphenylene moieties in the edge-on configuration. This kind of organization of molecules is further supported by the AFM studies of the LB films transferred from the

air-water interface onto hydrophilic substrates.

5.4.1 Nanoscale electrical conductivity studies

The LB film transferred onto a hydrophilic gold coated silicon substrate at a surface pressure of 4 mN/m was studied by CSAFM. The line profile on the topography image (Figure 5.6) yielded a height of 3.4 nm. This suggests that the organization of molecules on gold coated silicon substrate is similar to that on the hydrophilic mica and silicon substrates. Hence we infer that the anthraquinone moiety is in face-on configuration on the gold substrate and the triphenylene moiety is extended away from the substrate in edge-on configuration.

The current image obtained by scanning the LB film in contact mode by applying a sample bias of 0.5 V showed an average current value of about 1.5 nA in the region covered with film. In the region which is not covered with the film, high current value (> 10 nA) was obtained. This is because in the region with out the film, the tip will be in direct contact with the conducting gold substrate yielding high current value. On the other hand, in the region covered with the film the tip comes in contact with the triphenylene moieties and the current value depends on the electrical conductivity of the metal-film-metal junction.

The nanoscale electrical conductivity of the metal-film-metal junction was studied from the $I - V$ characteristics. As can be seen from Figure 5.7, the current value increases slowly for low applied bias voltages and then it sharply increases for relatively high applied bias voltages. Also there was a small offset of current value at zero applied bias voltage. This offset is usually attributed to the charging current of the system capacitance [18]. The shape of the $I - V$ curve strongly suggests that there is a potential barrier for the electron transfer between the two electrodes [19].

When two electrodes are separated by a film, the electron has to transfer across the insulating film. At equilibrium the top of the energy gap of the film will be above the Fermi level of the electrodes. Hence the film introduces a potential barrier between the metal electrodes which impedes the flow of electrons. The potential barrier extends from the electrode Fermi level to the bottom of the film conduction band. Electron transport between two electrodes

separated by a potential barrier can occur by two basic mechanisms. It can be either by Schottky emission (thermionic emission) or by electron tunneling. In Schottky emission, the electrons with sufficient energy pass over the potential barrier. When the electrons do not have sufficient energy to pass over the potential barrier, they can be transported by the mechanism of electron tunneling. Below we present the characteristics of these two mechanisms. We have analyzed our experimental data to find out the mechanism of electron transfer in the metal-AQD6-metal junction.

Schottky emission

Electron transport by Schottky emission or thermionic emission is usually observed in the metal-semiconductor junction [20]. In the metal-semiconductor junction the charges are separated and a region depleted of charge carriers is formed in the semiconductor. This results in the potential barrier for the charge transfer across the junction. Figure 5.10 shows the schematic energy band diagram for the metal-semiconductor junction. Energy band diagram for free metal and semiconductor are also shown. The current through such a junction is controlled by two processes, viz., thermionic emission and by drift and diffusion in the depletion region. If the barrier height is considered to be the difference between the work functions of the metal and semiconductor, then the resulting current-voltage relation can be written as,

$$I(V) = \frac{4\pi m^* e k_b^2 A}{h^3} T^2 \exp\left(-\frac{\phi_b}{k_b T}\right)\left[\exp\left(-\frac{e}{k_b T}V\right) - 1\right] \tag{5.2}$$

Here, A is the contact area, T is the temperature, k_b is the Boltzmann's constant, ϕ_b is the barrier height, e is the charge of electron, m^* is the effective mass of electron, and h is the Planck's constant.

In case of metal-semiconductor-metal junction there will be two metal-semiconductor interfaces in series. When a bias voltage is applied across the metal electrodes, one of the metal-semiconductor contacts will be forward biased and the other will be reverse biased. If the forward bias voltage is V_f and the reverse bias is V_r, then the total voltage across the

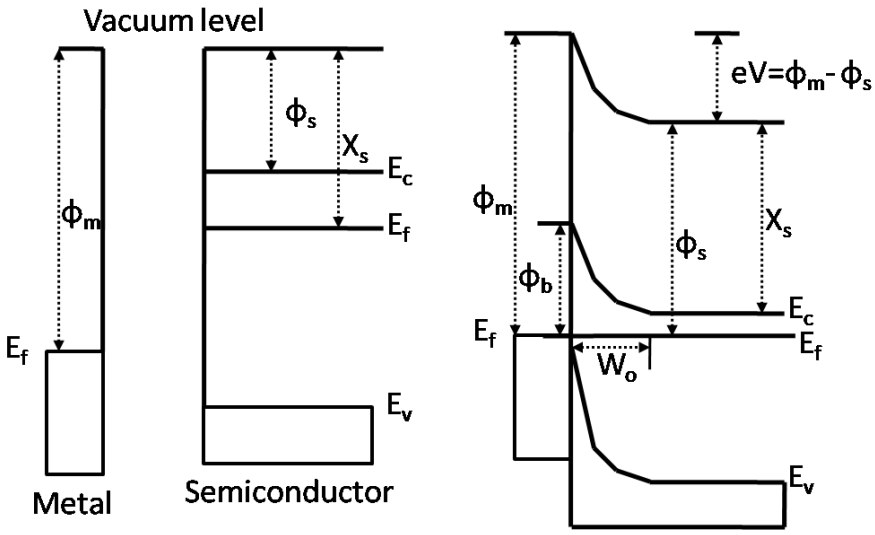

(a) (b)

Figure 5.10: (a) Shows the energy band diagram of metal and n-type semiconductor. (b) Shows the energy band diagram for metal-semiconductor interface. Here ϕ_m and ϕ_s are the work functions of metal and semiconductor, respectively. E_f is the Fermi energy, V is the applied voltage, X_s is the electron affinity, E_c is the lowest electron energy in the conduction band and E_v is the highest electron energy in the valance band. W_o is the width of the depletion layer. The Schottky barrier height is given by $\phi_b = \phi_m - \phi_s + E_c - E_f$.

electrodes is given by $V = V_f + V_r$. The current-voltage relation in such junctions is given by the following,

$$I = \frac{4\pi m^* e k_b^2 A}{h^3} T^2 \exp\left(-\frac{\phi_b}{k_b T}\right)\left[\frac{\exp\left(\frac{eV}{k_b T}\right) - 1}{\exp\left(\frac{eV}{k_b T}\right) + 1}\right] \tag{5.3}$$

Equation 5.3 suggests that the current value increases rapidly at low applied bias voltages and then saturates at high applied bias voltages. Hence in the Schottky emission, the $\mathrm{d}I/\mathrm{d}V$ decreases with increasing current.

Electron tunneling

Electron tunneling is a quantum mechanical phenomenon. Here a particle can penetrate through a classically forbidden region and transfer from one classically allowed region to another. This behavior can be explained by the wave nature of the particles. Electron tunneling can occur when two metal electrodes are separated by a thin insulating film and the current flows between the metal electrodes. The thin insulating film introduces a poten-

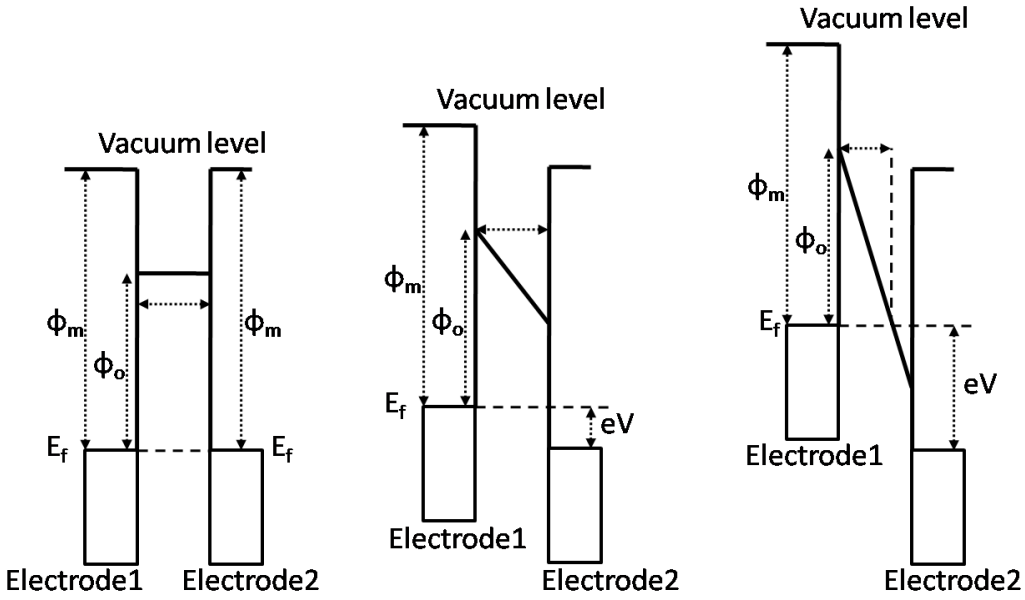

(a) $V \approx 0$ (b) $V < \phi_\circ/e$ (c) $V > \phi_\circ/e$

Figure 5.11: Figure shows the schematic energy band diagram of metal-film-metal junction for three applied bias voltages. (a) $V = 0$, Here the potential barrier is rectangular in shape (b) $V < \phi_\circ/e$, here the barrier is trapezoidal in shape and (c) $V > \phi_\circ/e$, here the barrier is triangular in shape.

tial barrier for the electron transfer. The energy band diagram of metal-film-metal junction with similar metal electrodes are shown in Figure 5.11. Simmons has derived a generalized formula for the electron tunneling effect between two electrodes separated by an insulating film [21]. According to his formula, the $I - V$ relation for the tunneling through the potential barrier of arbitrary shape is given by the equation,

$$I = \frac{eA}{2\pi h\overline{d}^2}\left[\overline{\phi}\exp\left(-\frac{4\pi\overline{d}\sqrt{2m^*\overline{\phi}}}{h}\right) - (\overline{\phi} + eV)\exp\left(-\frac{4\pi\overline{d}\sqrt{2m^*(\overline{\phi} + eV)}}{h}\right)\right] \tag{5.4}$$

Here, e is the charge of the electron, A is the effective electrical contact area between the tip and the film, $\overline{\phi}$ is the mean barrier height, $\overline{d}$ is the mean barrier width, m^* is the effective mass of electron and h is the Planck's constant. For very low applied bias voltage, the potential barrier is approximately of rectangular shape (Figure 5.11(a)). Here, $\overline{\phi} \approx \phi_\circ$ and $\overline{d} \approx d$, where $\phi_\circ$ is the height of rectangular barrier and d is the distance between the electrodes.

With these approximations [21], equation 5.4 reduces to,

$$I = \frac{A\sqrt{2m^*\phi_\circ}}{d}\left(\frac{e}{h}\right)^2 V\exp\left(-\frac{4\pi d\sqrt{2m^*\phi_\circ}}{h}\right). \tag{5.5}$$

At intermediate bias voltages ($V < \phi_\circ/e$), the potential barrier can be considered to be of trapezoidal shape as shown in Figure 5.11(b). In this regime, $\overline{\phi} \approx \phi_\circ - eV/2$ and $\overline{d} \approx d$. For the alkyl chain molecules it has been reported that the electron transport mechanism at intermediate bias voltages ($V < \phi_\circ/e$) is by direct tunneling [22]. Direct tunneling refers to the tunneling of the electron from one electrode to the other, without hopping or diffusing into the insulating medium.

In the high bias voltage regime ($V > \phi_\circ/e$), the barrier is approximately of triangle shape and is synonymous with the injection tunneling or Fowler-Nordheim (FN) tunneling [23]. Figure 5.11(c) shows the schematic energy band diagram of metal-film-metal junction for high applied bias voltage. In this regime, by assuming the $\overline{\phi}$ to be approximately equal to $\phi_\circ/2$ and $\overline{d}$ to be approximately equal to $d\phi_\circ/(eV)$, the following tunneling current-voltage relation [24] can be obtained. .

$$I = \frac{Ae^3V^2m_e}{8\pi h\phi_\circ d^2m^*}\exp\left(-\frac{8\pi d\sqrt{2m^*\phi_\circ^3}}{3heV}\right). \tag{5.6}$$

Here, m_e is the mass of free electron. In injection (FN) tunneling, the electron is first injected into the insulating medium through the triangular barrier before it is transported to the second electrode.

A transition in the electron transport mechanism from the direct tunneling at low voltages to the injection tunneling at high voltages is possible, when the value of applied bias voltage is in the vicinity of the barrier height of the film [23]. In direct tunneling, the value of $\ln(I/V^2)$ logarithmically increases with $1/V$ and in injection tunneling, $\ln(I/V^2)$ linearly decreases with $1/V$. Hence a minimum in the variation of $\ln(I/V^2)$ as a function of $1/V$ indicates a transition. The bias voltage corresponding to the transition is called transition voltage (V_{trans}).

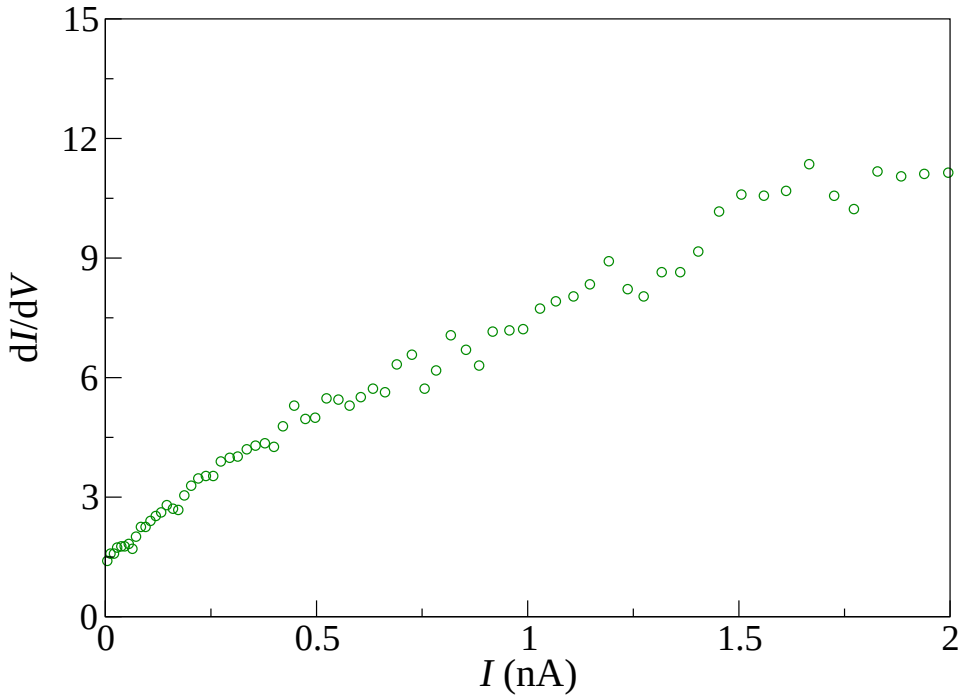

Figure 5.12: Variation of dI/dV as a function of I. Since dI/dV increases with increase in I, Schottky emission is not the dominating mechanism for the electron transport.

We have analyzed the $I-V$ characteristics for the gold-AQD6-platinum junction. We find that the derivative dI/dV increases with increase in I value (Figure 5.12). Since the Schottky emission is characterized by decrease in the dI/dV as the current increases, we infer that Schottky emission is not the dominating mechanism for the electron transfer [25]. Hence the electron tunneling is a possible means of current flow between the tip and the substrate separated by AQD6 monolayer.

In order to find the barrier height of the metal-AQD6-metal junction, we have further analyzed the $I-V$ characteristics. The variation of $\ln(I/V^2)$ as a function of $1/V$ gives information about the electron tunneling mechanism. We find that there is a transition in the electron tunneling mechanism as the applied bias voltage is increased. Figure 5.13 shows the typical plot of $\ln(I/V^2)$ as a function of $1/V$ for AQD6 monolayer film for the positive bias voltages. We have indicated the transition from the direct tunneling regime to the injection tunneling regime by a dashed line (Figure 5.13). The corresponding V_{trans} value can be used to estimate the barrier height ($\phi_\circ$) [26]. The average value of $\phi_\circ$ obtained from thirty

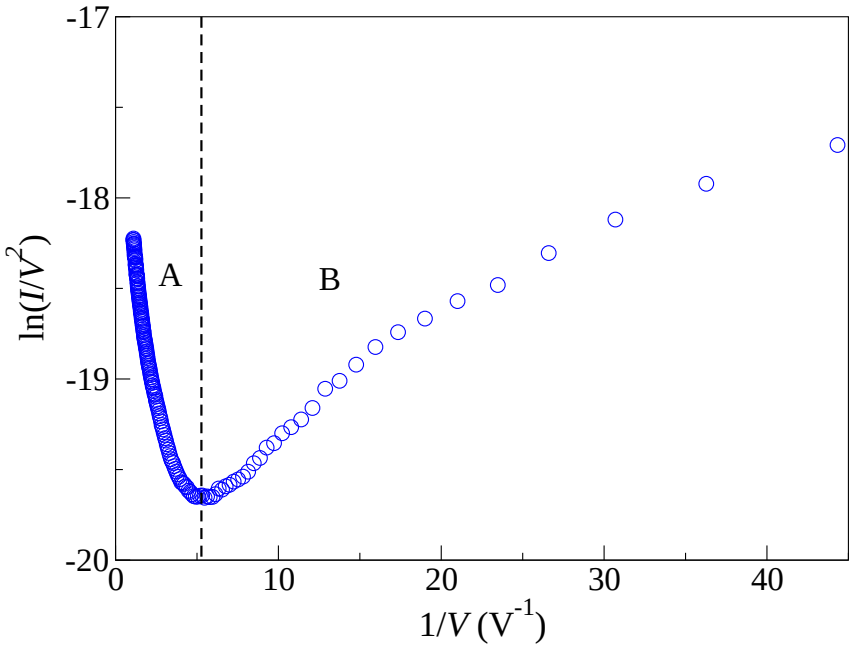

Figure 5.13: Variation of $\ln(I/V^2)$ as function of $1/V$, showing injection tunneling regime (A) and direct tunneling regime (B) separated by a dashed line. Logarithmic increase of $\ln(I/V^2)$ can be seen for direct tunneling and the linear decay of $\ln(I/V^2)$ can be seen for injection tunneling. The dashed line shows the transition point.

independent $I - V$ curves taken at different locations over three sample plates was about (0.19 ± 0.02) eV.

The values of the effective mass of electron and effective electrical contact area between tip and film can be obtained by analyzing the $I - V$ data in the high voltage regime. In this regime, $\ln(I/V^2)$ varies linearly with $1/V$ and they are related by the following equation,

$$ln\left(\frac{I}{V^2}\right) = -\left(\frac{8\pi d\sqrt{2m^*\phi_\circ^3}}{3he}\right)\left(\frac{1}{V}\right) + \frac{Ae^3m_e}{8\pi h\phi_\circ d^2m^*} \tag{5.7}$$

Equation 5.7 represents a straight line with slope (S) and intercept (C) which are given by the following expressions:

$$S = -\frac{8\pi d\sqrt{2m^*\phi_\circ^3}}{3he}$$

and

$$C = \frac{Ae^3m_e}{8\pi h\phi_\circ d^2m^*}$$

The values of S and C can be obtained by fitting a straight line to the $\ln(I/V^2)$-$(1/V)$ data

in the high voltage regime. Substituting the values of S, $\phi_\circ$, h, e and d in the appropriate units into the expression for S, the effective mass of electron (m^*) can be calculated. In our system, d corresponds to the thickness of the film (3.4 nm) since the tip is located just at the surface of the film. We obtain the m^* value to be $(0.120 \pm 0.004)m_e$. From the intercept of the straight line, we have calculated the value of the effective electrical contact area (A) between the tip and the film to be (0.54 ± 0.02) nm^2.

The V_{trans} calculated for the positive and negative applied bias voltages were different. The value of V_{trans} obtained by applying positive bias voltage to the substrate (V^+_{trans} = (0.19± 0.02) V) was less than the value of V_{trans} obtained for negative bias voltage (V^-_{trans} = (0.34 ± 0.02) V). Similar behavior has been reported in the case of π-conjugated thiol system and was attributed to the asymmetry in the two metal-film contacts [23]. The molecules of AQD6 in the LB monolayer were oriented in such a way that the triphenylene moiety was in contact with the conducting platinum tip and the anthraquinone moiety was in contact with the gold substrate. Hence the electronic states at the gold substrate-film interface arising from the coupling between the electrons of anthraquinone and gold will be different from that of the tip-film interface arising due to the coupling between the electrons of triphenylene and platinum [2]. This asymmetry in the potential barrier between the metal electrodes results in unequal potential drop at the two metal-film interfaces.

It should be noted that the $\phi_\circ$ value was estimated assuming the potential barrier to be of simple geometrical shape (trapezoidal, triangle). To get more accurate values of the barrier height, actual potential barrier has to be modeled by considering the structure and organization of the molecules. In literature, the transition in the electron transport mechanism has been reported only in the self assembled monolayer of $\pi-$conjugated thiol molecules [23] and in the purple membrane monolayer [26]. For the alkyl systems [22], direct tunneling is the dominant mechanism for the electron transport. The absence of the injection tunneling in this case has been attributed to the high value of band gap (8 eV) between the highest occupied molecular orbital (HOMO) and lowest unoccupied molecular orbital (LUMO). CSAFM studies on the LB film of a derivative of electron rich triphenylene moiety has shown that the

electron transport is by injection tunneling [25]. The absence of the direct tunneling in this system was attributed to the low band gap between the HOMO and LUMO in the film. The molecular conduction behavior significantly changes not only with the molecular structure but also with the molecular environment [27]. The transition in the tunneling mechanism in our system can be attributed to the relatively low barrier height imposed by the metal-AQD6-metal junction for the electron transport. Our studies are useful in understanding the role of the molecular architecture on the electrical conductivity of ultra thin films.

5.5 Conclusions

Monolayer film of a star shaped discotic oligomer made up of triphenylene and anthraquinone moieties was studied at air-water and air-solid interfaces. At air-water interface the material exhibits stable monolayer. At A_m greater than 7.0 nm^2 the monolayer exhibited coexistence of gas and low density liquid (L_1) phase which transformed into uniform L_1 phase on compression. On further compression, the monolayer collapsed at an A_m of 6.2 nm^2 with a collapse pressure of 4.3 mN/m. The monolayer films transferred onto the hydrophilic substrates of mica and silicon by LB technique were studied by AFM. The line profile on the topography images yielded the height of the films on the two substrates to be about 3.4 nm. The limiting area of the molecule in the Langmuir monolayer and height of the LB film suggest that the anthraquinone moiety is in face-on configuration on the substrate and the triphenylene moieties are in edge-on configuration extended away from the substrate.

The film transferred onto a hydrophilic gold coated silicon substrate was studied by CSAFM. We find that the current through the film is by electron tunneling. Our analysis of the $I-V$ characteristics shows a transition in the electron transfer mechanism as the applied bias voltage is increased. At low bias voltages, the electron transfer was through direct tunneling and at high bias voltages, the electron transfer was through injection tunneling. The bias voltage at which the transition occurs (V_{trans}) was obtained from the $\ln(I/V^2)$ versus $1/V$ plot. The V_{trans} value was used to estimate the barrier height $\phi_\circ$ of the film. From the

analysis of the $I - V$ data in the high voltage regime, we have calculated the effective mass of electron m^* to be $0.12m_e$ and the effective electrical contact area between the cantilever tip and the film to be 0.54 nm^2.

Bibliography

[1] A. Aviram, and M. A. Ratner, *Chem. Phys. Lett.* **29**, 277 (1974).

[2] K. Moth-Poulsen, and T. Bjrnholm, *Nature Nanotech.* **4**, 1 (2009).

[3] L. Schmidt-Mende, A. Fechtenkotter, K. Mullen, E. Moons, R. H. Friend, and J. D.MacKenzie, *Science* **293**, 1119 (2001).

[4] B. W. Laursen, K. Norgaard, N. Reitzel, J. Simonsen, C. B. Nielsen, J. Als-Nielsen, T. Bjornholm, T. I. Solling, M. M. Nielson, O. Bunk, *et al.*, *Langmuir* **20**, 4139 (2004).

[5] N. V. Tkachenko, A. Y. Tauber, P. H. Hynninen, A. Y. Sharonov, and H. Lemmetyinen, *J. Phys. Chem. A* **103**, 3657 (1999).

[6] S. Sergeyev, W. Pisula, and Y. H. Geerts, *Chem. Soc. Rev.* **36**, 1902 (2007).

[7] J. Y. Josefowicz, N. C. Maliszewskyj, S. H. J. Idziak, P. A. Heiney, J. P. McCauley, and A. B. Smith, *Science* **260**, 323 (1993).

[8] H. Schonherr, F. J. B. Kremer, S. Kumar, J. A. Rego, H. Wolf, H. Ringsdorf, M. Jaschke, H. J. Butt, and E. Bamberg, *J. Am. Chem. Soc.* **118**, 13051 (1996).

[9] F. Charra and J. Cousty, *Phys. Rev. Lett.* **80**, 1682 (1998).

[10] A. Nayak, K. A. Suresh, S. K. Pal, and S. Kumar, *J. Phys. Chem. B* **111**, 11157 (2007).

[11] V. V. Tsukruk, H. Bengs, and H. Ringsdorf, *Langmuir* **12**, 754 (1996).

[12] N. C. Maliszewskyj, P. A. Heiney, J. Y. Josefowicz, T. Plesnivy, H. Ringsdorf, and P. Schuhmacher, *Langmuir* **11**, 1666 (1995).

[13] J. P. Pradeau, H. Perez, and F. Armand, *J. Phys. D: Appl. Phys.* **32**, 968 (1999).

[14] S. Kumar, *Liquid Crystals* **36**, 607 (2009).

[15] J. T. Davies and E. K. Rideal, *Interfacial Phenomena*, Academic Press: NewYork, (1963).

[16] D. J. Dervichian, *J. Chem. Phys.* **7**, 932 (1939).

[17] O. Albrecht, W. Cumming, W. Kreuder, A. Laschewsky, and H. Ringsdorf, *Colloid Polym. Sci.* **264**, 659 (1986).

[18] P. Mishra, P. Karmakar, and D. Ghose, *Nucl. Instrum. Methods Phys. Res. B* **243**, 16 (2006).

[19] D. Xu, G. D. Watt, J. N. Harb, and R. C. Davis, *Nano Lett.* **5**, 571 (2005).

[20] S. M. Sze, *Physics of Semiconductor Devices*, John Wiley and Sons: New York (1981).

[21] J. G. Simmons, *J. Appl. Phys.* **34**, 1793 (1963).

[22] W. Wang, T. Lee, and M. A. Reed, *Phys. Rev. B* **68**, 035416 (2003).

[23] J. M. Beebe, B. Kim, J. W. Gadzuk, C. D. Frisbie, and J. G. Kushmerick, *Phys. Rev. Lett.* **97**, 026801 (2006).

[24] M. Lenzlinger, and E. H. Snow, *J. Appl. Phys.* **40**, 278 (1969).

[25] A. Nayak, and K. A. Suresh, *Phys. Rev. E* **78**, 021606 (2008).

[26] I. Casuso, L. Fumagalli, J. Samitier, E. Padros, L. Reggiani, V. Akimov, and G. Gomila, *Phys. Rev. E* **76**, 041919 (2007).

[27] Y. Selzer, L. Cai, M. A. Cabassi, Y. Yao, J. M. Tour, T. S. Mayer, and D. L. Allara, *Nano Lett.* **5**, 61 (2005).

Chapter 6

Langmuir and Langmuir-Blodgett films of novel mesogenic polymers of triphenylene and anthraquinone moieties

6.1 Introduction

Polymer thin films is an emerging area driven by their enormous technological potential [1]. Thin films of polymers have technological applications like in the fabrication of nonvolatile memory devices [2], sensors [3] etc. Polymers of discotic liquid crystals are finding special interest because of their supramolecular ordering, easy processability and spontaneous self-organization. These can be used as functional materials for device applications such as one-dimensional conductors, photoconductors, light emitting diodes [4], photovoltaic solar cells [5], field effect transistors [6] and gas sensors [7]. For many applications, ultrathin films of thickness less than 25 nm are required to get desired properties [8]. Langmuir-Blodgett (LB) technique enables one to fabricate uniform ordered films with thickness of the order of molecular length [9]. Hence, understanding the assembly and organization of such polymers in Langmuir monolayers and LB films is important.

In the previous chapter, we have studied the Langmuir monolayer and LB films of a star shaped liquid crystalline oligomer made up of electron rich triphenylene moiety and elec-

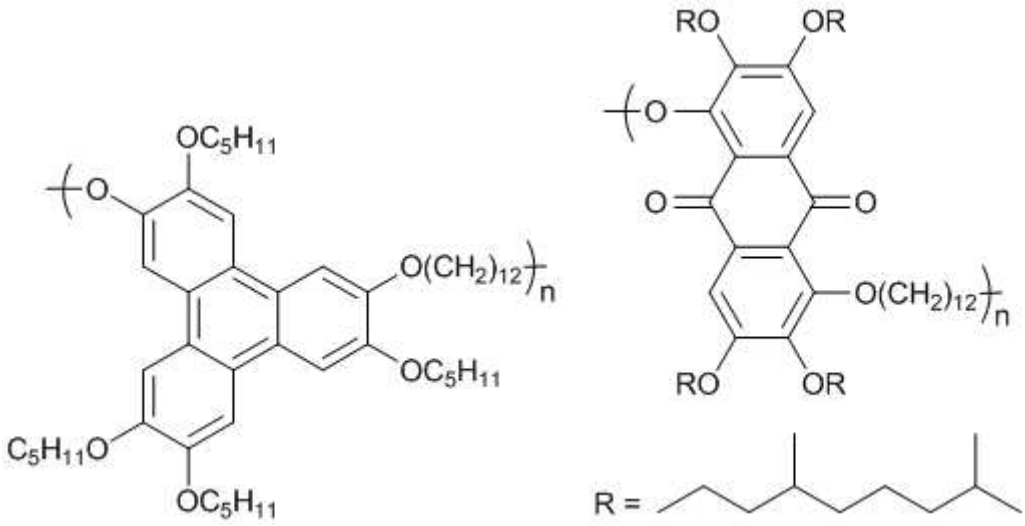

(a) Triphenylene polymer (b) Anthraquinone polymer

Figure 6.1: Molecular structure of (a) triphenylene polymer (Trp) and (b) anthraquinone polymer (Aqp). The average molecular weight of Trp was 13, 515 and that of Aqp was 13, 691.

tron deficient anthraquinone moiety. In this chapter, we report our studies on the polymers of triphenylene moiety and anthraquinone moiety. Here the polymer of triphenylene (Trp) is electron rich and the polymer of anthraquinone (Aqp) is electron deficient. We find that the Trp and Aqp molecules form stable monolayer at air-water interface. The Trp and Aqp monolayers on compression exhibit uniform low density liquid phase before collapsing. Ultrathin films of both the materials on the solid substrates were prepared by LB technique. Atomic force microscope studies were carried out to characterize the LB films. We find that in the LB films of both materials, the discotic moieties were in edge-on configuration.

6.2 Experiment

The materials Trp and Aqp were synthesized by Sandeep Kumar and H. K. Bisoyi [10]. The purity of the materials was found to be better than 99% by NMR, IR and elemental analysis techniques. Gel permeation chromatography analysis of the materials yielded the average molecular weight of Trp to be 13, 515 and that of Aqp to be 13, 691. Figure 6.1 shows the molecular structure of the Trp and Aqp molecules. Films of Trp and Aqp molecules were

studied at air-water interface using the surface manometry and Brewster angle microscopy (BAM) techniques. The surface manometry studies were carried out using a Nima trough (Model: 611M). The trough was enclosed in an aluminum box to prevent ambient light, air drag and contaminants. Ultra-pure deionized water (millipore water, MilliQ) was used as subphase. Dilute solutions of the materials were prepared in HPLC grade chloroform. The concentration of the Trp-chloroform solution was 0.13 mg/ml and that of Aqp-chloroform solution was 0.15 mg/ml. The Langmuir monolayers of the two polymers were formed by spreading the respective stock solution at air-water interface using a micro-syringe. The temperature of the monolayer was maintained at 24.0 ± 0.1°C by circulating water in the trough using a controller (Julabo, F25). Wilhelmy method was used to measure the surface pressure. The film at the air-water interface was compressed between two barriers symmetrically moving at a constant rate. BAM studies were carried out using a MiniBAM (NFT, Nanotech).

Films of Trp molecules were transferred by Langmuir-Blodgett (LB) technique onto the hydrophilic mica and hydrophobic silicon substrates. On the hydrophilic mica substrate one layer of the film will be transferred in one dipping cycle (consisting of one down-stroke and one up-stroke). The transfer of the film occurred during the up-stroke. The hydrophobic silicon substrate was obtained by preparing the self assembled monolayer of hexamethyl disilazane (HMDS) on a polished silicon wafer as explained in Chapter 2. Two layers of the film get transferred on a hydrophobic silicon substrate in one dipping cycle. The transfer of the film occurred both during down-stroke and up-stroke. The LB transfer was carried out at a surface pressure of 5 mN/m, with a dipping speed of 2 mm/min.

Films of Aqp molecules were transferred by LB technique onto the mica and gold coated silicon substrates. The film was transferred at a surface pressure of 7 mN/m, with a dipping speed of 2 mm/min. Freshly cleaved mica and gold coated silicon substrates have hydrophilic surface. Hence, one layer of the film gets transferred in one dipping cycle. The transfer occurred during the up-stroke.

The LB films of Trp and Aqp molecules were studied by employing an atomic force

microscope (AFM) (Model: PicoPlus, Molecular Imaging). Silicon cantilevers with a spring constant of about 31 N/m and resonance frequency of 200 kHz were used. The AFM images were acquired using the AC mode in ambient conditions.

6.3 Results

6.3.1 Triphenylene polymer (Trp)

The average molecular weight of the Trp was 13,515 [10]. Since the molecular weight of each monomer is 770, we infer that each Trp molecule has approximately 17 discotic monomer units. The material Trp exhibits a birefringence texture under a polarizing microscope. On heating, it slowly transformed to isotropic state at 89°C. On cooling, a birefringence texture gradually appears. The material Trp exhibits columnar hexagonal phase at room temperature [10].

Surface manometry

Surface manometry studies showed that the Trp molecules form a stable monolayer at air-water interface. Figure 6.2 shows the surface pressure (π)−area per molecule (A_m) isotherm of Trp monolayer. At large A_m the π was zero. The π starts increasing at an A_m of about 19 nm^2. After steep rise in π, the monolayer collapsed at an A_m of 15 nm^2 with a collapse pressure of 6.3 mN/m. The limiting area per molecule ($A_\circ$) was obtained by extrapolating steep region of the isotherm to zero surface pressure which yielded a value of 18.6 nm^2.

Brewster angle microscopy

Brewster angle microscope (BAM) studies showed the phases exhibited by the Langmuir monolayer of Trp molecules for various values of A_m. For A_m greater than 19 nm^2, the Trp monolayer showed dark region (Figure 6.3(a)). This on compression formed uniform grey region as shown in Figure 6.3(b). On further compression of the monolayer, at an A_m of

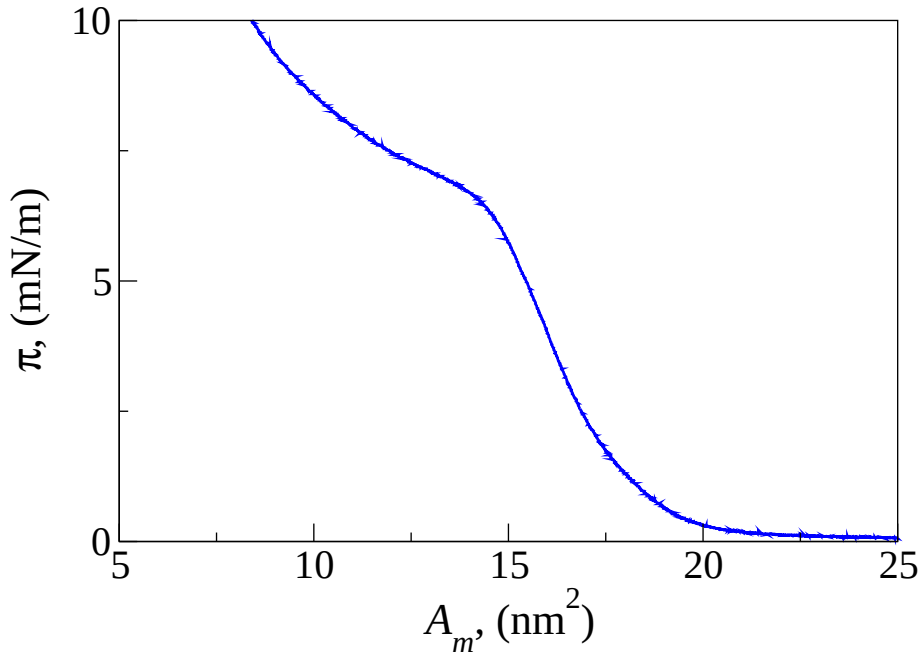

Figure 6.2: Surface pressure(π)−area per molecule(A_m) isotherm of triphenylene polymer (Trp). The monolayer was compressed at a rate of 7 cm^{2}min^{-1} at a temperature of 24.0°C.

15 nm^2, bright patches appeared in the grey region indicating a collapse. This is shown in Figure 6.3(c).

Atomic force microscopy

To understand the configuration of the Trp molecules at air-solid interface, we have carried out the AFM studies of LB film transferred onto the hydrophilic mica and hydrophobic silicon substrates. We have transferred the Langmuir monolayer onto a hydrophobic silicon substrate at a surface pressure of 5 mN/m. Two layers of the film was transferred onto it with a transfer ratio of about 0.95. Figure 6.4 shows the AFM image of the LB film on hydrophobic silicon substrate. The line profile on the topography image yields a height of about 3.7 nm.

Figure 6.5 shows an AFM image of the Trp monolayer transferred onto a mica substrate at a surface pressure of 5 mN/m. The transfer ratio was about 0.90. The AFM topography image shows a mesh like pattern. The line profile on the topography image yields a height of 1.9 nm.

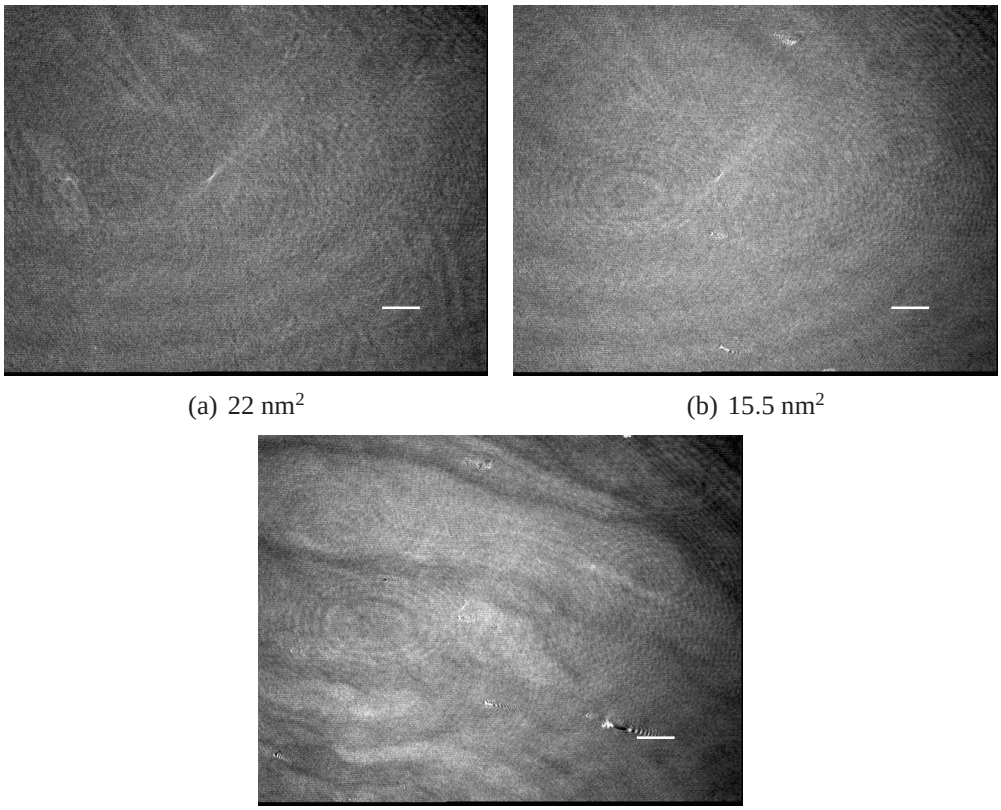

(a) 22 nm^2 (b) 15.5 nm^2

(c) 10.2 nm^2

Figure 6.3: BAM images of the monolayer of Trp molecules at air-water interface for various values of A_m. (a) Shows dark region at an A_m of 22 nm^2. (b) Shows uniform grey region at an A_m of 15.5 nm^2. This corresponds to the low density liquid (L_1) phase of the Trp monolayer. (c) Shows the collapsed state with bright patches growing in the grey region at an A_m of 10.2 nm^2. The scale bar in each image represents 500 μm.

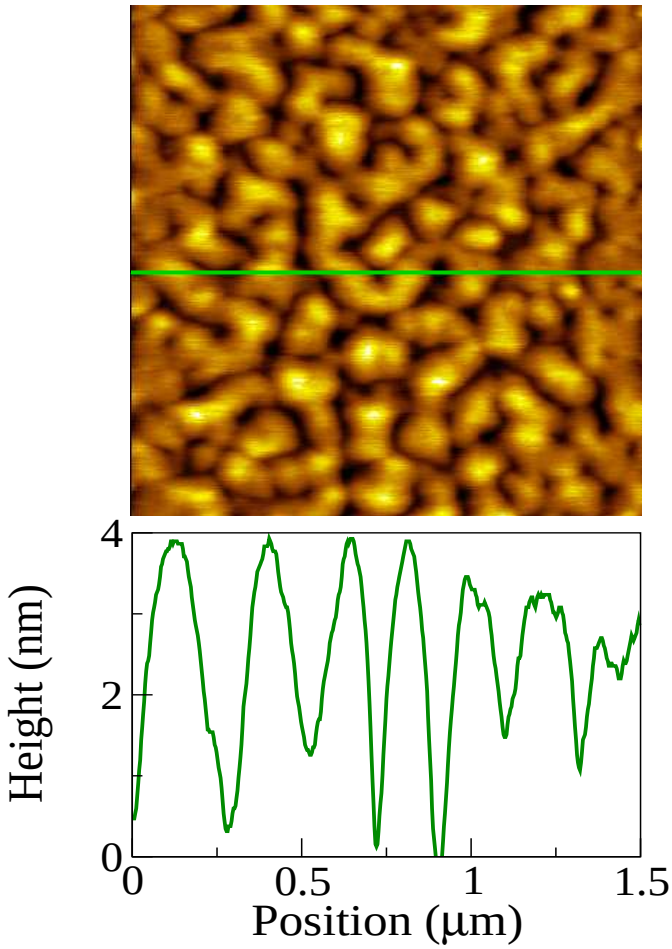

Figure 6.4: AFM topography image of Trp LB film on a hydrophobic silicon substrate transferred at a surface pressure of 5 mN/m. The line profile yields a height of 3.7 nm. This height corresponds to the bilayer thickness when the discotic moieties are in edge-on configuration.

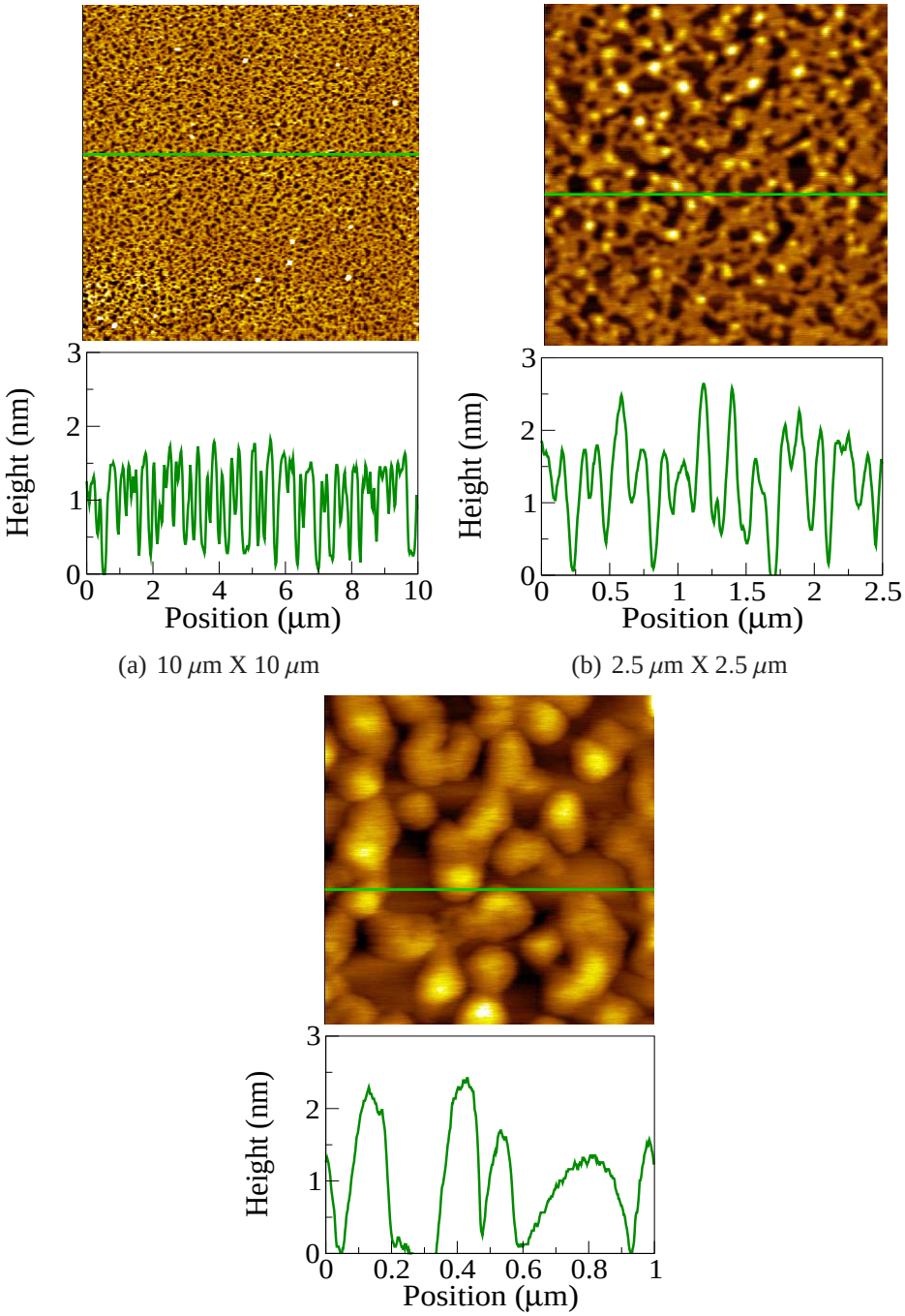

(a) 10 μm X 10 μm

(b) 2.5 μm X 2.5 μm

(c) 1 μm X 1 μm

Figure 6.5: AFM topography image of Trp monolayer LB film on a hydrophilic mica substrate transferred at a surface pressure of 5 mN/m. (a) Shows 10 μm X 10 μm scan area, (b) shows 2.5 μm X 2.5 μm scan area and (c) shows 1 μm X 1 μm scan area. The line profile yields a height of about 1.9 nm.

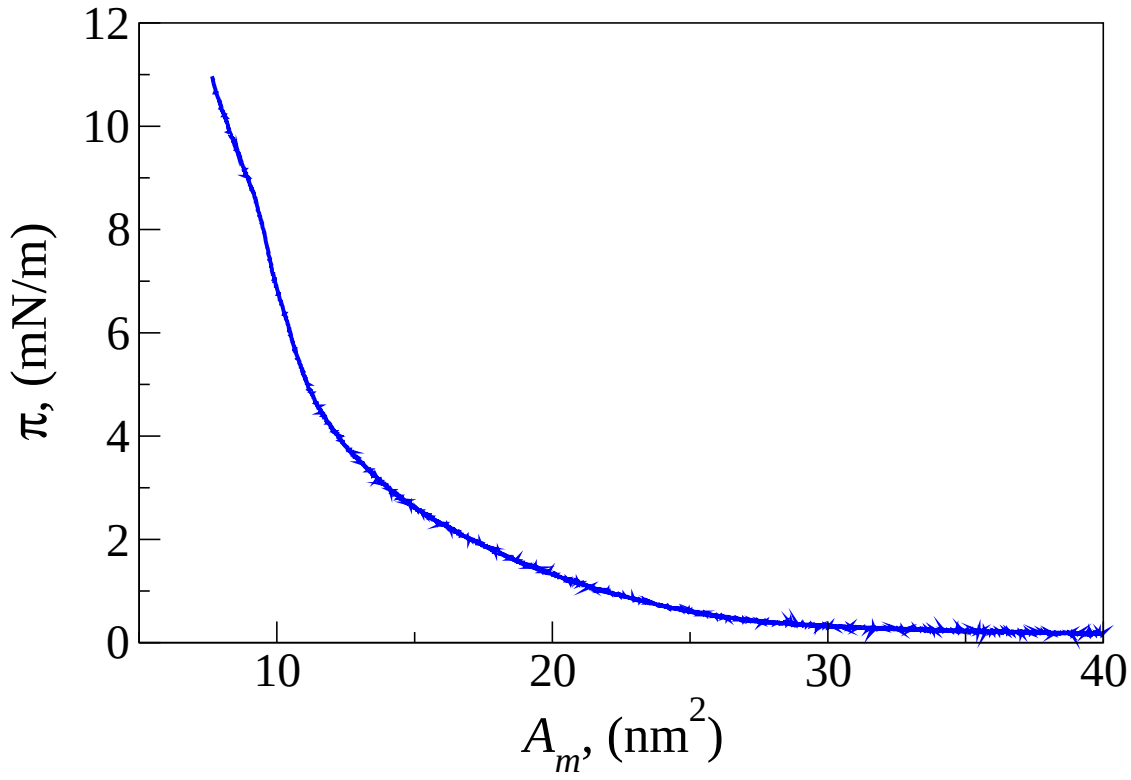

Figure 6.6: Surface pressure (π)−area per molecule (A_m) isotherm of anthraquinone polymer. The monolayer was compressed at a rate of 7 cm^{2}min^{-1} at a temperature of 24°C.

6.3.2 Anthraquinone polymer (Aqp)

The average molecular weight of Aqp was 13, 691 [10]. Since the molecular weight of each monomer is 1, 090, we infer that each Aqp molecule has approximately 13 discotic monomer units. The material Aqp exhibits a birefringence texture under a polarizing microscope. On heating, it slowly transformed to isotropic state at 56.3°C. On cooling, a birefringence texture slowly appears. The X-ray and miscibility studies showed that the Aqp exhibits rectangular columnar phase at room temperature [10].

Surface manometry

Surface manometry studies showed that the Aqp molecules form stable monolayer at air-water interface. Figure 6.6 shows the $\pi - A_m$ isotherm of Aqp monolayer. At high A_m the surface pressure is zero. On compression, around the A_m value of 30 nm^2 the π gradually increases. At A_m of 11.5 nm^2 the π steeply increases before collapsing at an A_m of 9.2 nm^2

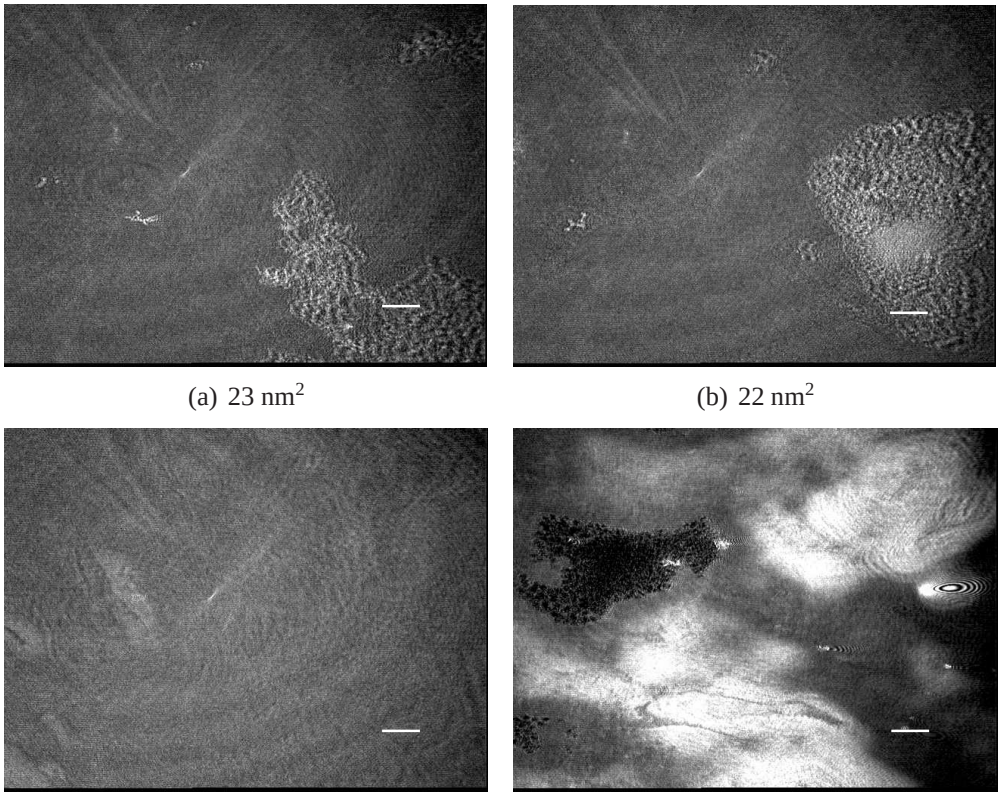

(a) 23 nm^2 (b) 22 nm^2

(c) 11.5 nm^2 (d) 6.7 nm^2

Figure 6.7: BAM images of the Aqp monolayer at air-water interface. (a) Shows the coexistence of grey and dark regions at 23 nm^2. (b) Shows the growing grey region at 22 nm^2. (c) Shows uniform grey region in the monolayer at an A_m of 11.5 nm^2. This uniform phase corresponds to the low density liquid (L_1) phase. (d) Shows the bright region at an A_m of 6.7 nm^2 corresponding to the collapsed state of the monolayer. The scale bar in each image represents 500 μm.

with a collapse pressure of 8.6 mN/m. The limiting area $A_\circ$ of the molecules is obtained by extrapolating the $\pi - A_m$ isotherm to surface pressure. The $A_\circ$ has a value of 12.7 nm^2.

Brewster angle microscopy

Brewster angle microscope (BAM) studies showed the phases exhibited by Langmuir monolayer of Aqp molecules at various A_m. The monolayer of Aqp at A_m greater than 30 nm^2 showed coexistence of grey and dark regions (Figure 6.7(a)). On compressing the monolayer, the grey region grew in size (Figure 6.7(b)). At an A_m below 11.5 nm^2 the monolayer exhibited uniform grey region (Figure 6.7(c)). On further compression, the brightness of the grey region gradually increased until the monolayer collapsed at an A_m of 9.2 nm^2 (Fig-

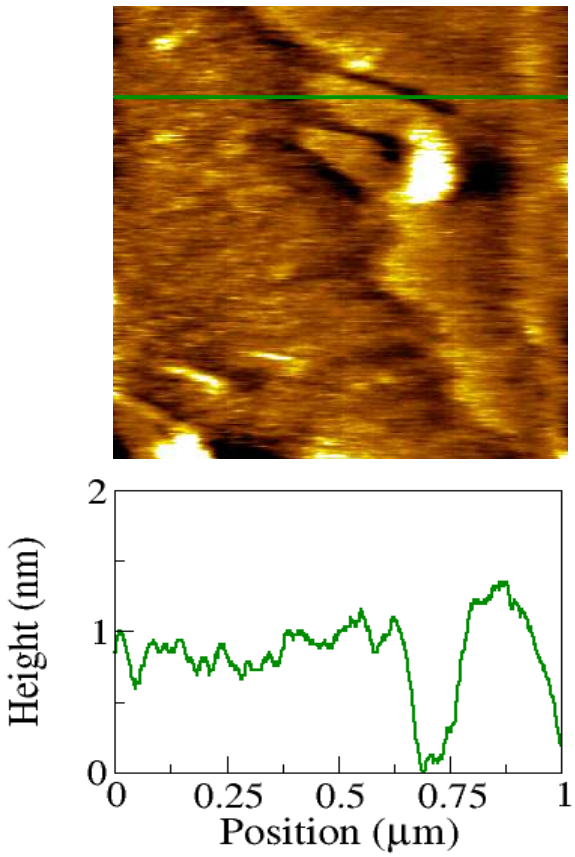

Figure 6.8: AFM topography image of Aqp monolayer LB film on a mica substrate transferred at a surface pressure of 7 mN/m. The line profile yields a height of 1.0 nm.

ure 6.7(d)).

Atomic force microscopy

To understand the configuration of the molecules at air-solid interface we have carried out the AFM studies of LB film transferred onto the hydrophilic mica and gold coated silicon substrates. The film was transferred at a surface pressure of 7 mN/m. The transfer ratio on both the substrates was about 0.80. AC mode AFM was employed to acquire the topography images. Figure 6.8 shows the AFM image of the Aqp monolayer on a hydrophilic mica substrate. The line profile on the topography image yields a height of 1.0 nm.

Figure 6.9 shows the AFM image of the monolayer transferred onto a gold coated silicon substrate. The line profile on the topography image yields a height of about 1.0 nm.

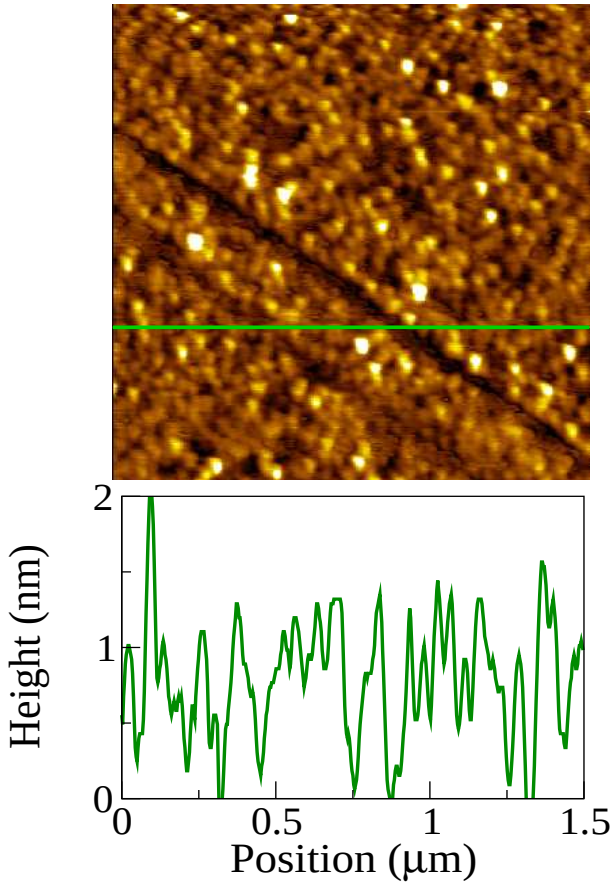

Figure 6.9: AFM topography image of Aqp monolayer LB film on a gold coated silicon substrate transferred at a surface pressure of 7 mN/m. The line profile yields a height of about 1.0 nm.

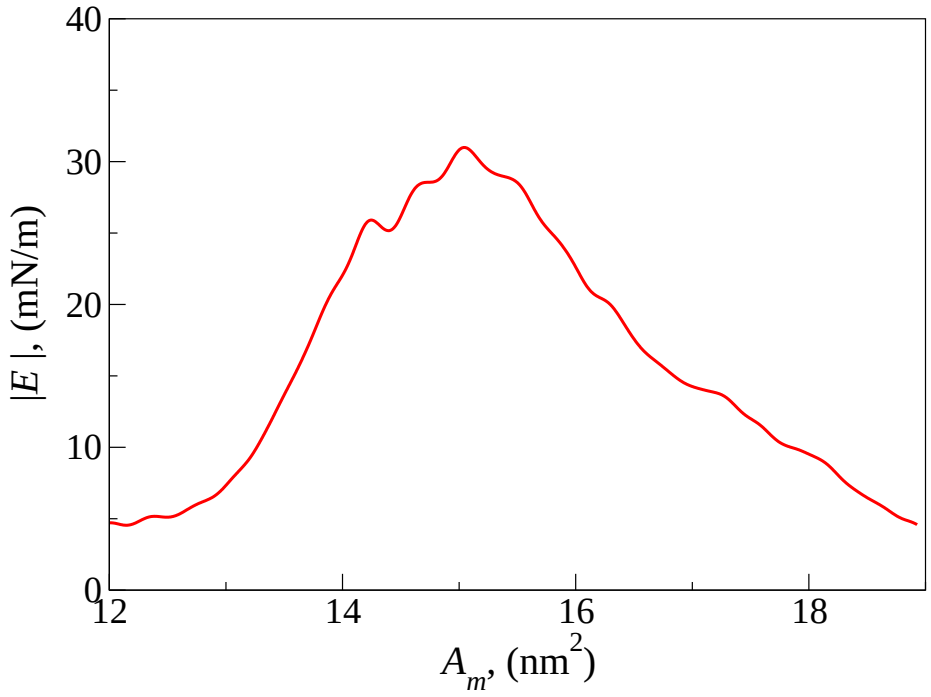

Figure 6.10: Compressional modulus $|E|$ as a function of area per molecule (A_m) for the monolayer of triphenylene polymer. The maximum value of $|E|$ was about 30 mN/m which corresponds to low density liquid (L_1) phase.

6.4 Discussion

Surface manometry and BAM studies of the Trp Langmuir monolayer suggested that it exhibited gas phase at high A_m. On compression, the monolayer transformed to an uniform phase at an A_m of 19 nm^2. It collapsed at an A_m of about 14 nm^2. The uniform phase exhibited by the Trp monolayer can be characterized from the compressional modulus $|E|$ of the monolayer [11]. The $|E|$ value can be calculated from the $\pi - A_m$ isotherm using the following relation.

$$|E| = A_m \left(\frac{\mathrm{d}\pi}{\mathrm{d}A_m} \right) \tag{6.1}$$

Figure 6.10 shows the variation of compressional modulus as a function of area per molecule for the Trp monolayer. According to the criteria given in the literature [12, 13], the monolayer phase with maximum $|E|$ value in the range of 12.5 mN/m to 50 mN/m corresponds to the low density liquid (L_1) or liquid expanded phase. The maximum value of $|E|$ obtained for the Trp monolayers in the uniform region was 30 mN/m (Figure 6.10). Hence we infer that the

monolayer exhibited gas phase at high area per molecule. On compression, it transformed into uniform low density liquid phase at an A_m of 19 nm^2. At an A_m of 14 nm^2 the monolayer collapsed with a collapse pressure of 6.3 mN/m.

The limiting area of a triphenylene monomer in the edge-on configuration [14] is about 1.1 nm^2 and the estimated number of monomers in the Trp is about 17 (obtained from the molecular weight). Hence the area occupied by 17 edge-on triphenylene moieties is 18.7 nm^2. Since the limiting area for Trp molecule (18.6 nm^2) is equal to the limiting area of 17 triphenylene monomers in the edge-on configuration, we suggest that the triphenylene moieties in the Trp molecule assemble in edge-on configuration at air-water interface.

AFM images of the Trp film on hydrophilic mica substrate showed mesh like pattern. The line profile on the topography image yielded a height of about 1.9 nm. This height is equal to the estimated diameter (using ChemDraw) of the triphenylene moieties. Hence we suggest that the triphenylene moieties are in the edge-on configuration on the substrate. This is further supported by our surface manometry studies which yielded the limiting area corresponding to the edge-on configuration of the triphenylene moieties. The LB film on the hydrophobic silicon substrate showed a film of height 3.7 nm. Since the thickness of the monolayer film was about 1.9 nm, the height obtained for the film on hydrophobic silicon substrate corresponds to the bilayer thickness.

The $\pi - A_m$ isotherm and the BAM images showed that the Aqp molecules form stable monolayer at air-water interface. At high A_m, the monolayer exhibited coexistence of gas and liquid phase. Between the A_m of 11.5 nm^2 and 9.2 nm^2 the monolayer exhibited an uniform phase as indicated by the uniform grey region in the BAM images. The phase in the uniform grey region can be characterized from the compressional modulus ($|E|$) value of the monolayer [11]. The $|E|$ values can be obtained from the $\pi - A_m$ isotherm using equation 6.1. Figure 6.11 shows the variation of $|E|$ as a function of A_m for the Aqp monolayer. In the uniform region, the $|E|$ has a maximum value of about 52 mN/m. This value of $|E|$ corresponds to the low density liquid (L_1) phase of the monolayer [12, 13]. Hence we infer that the monolayer of Aqp exhibited coexistence of the low density liquid phase and gas phase

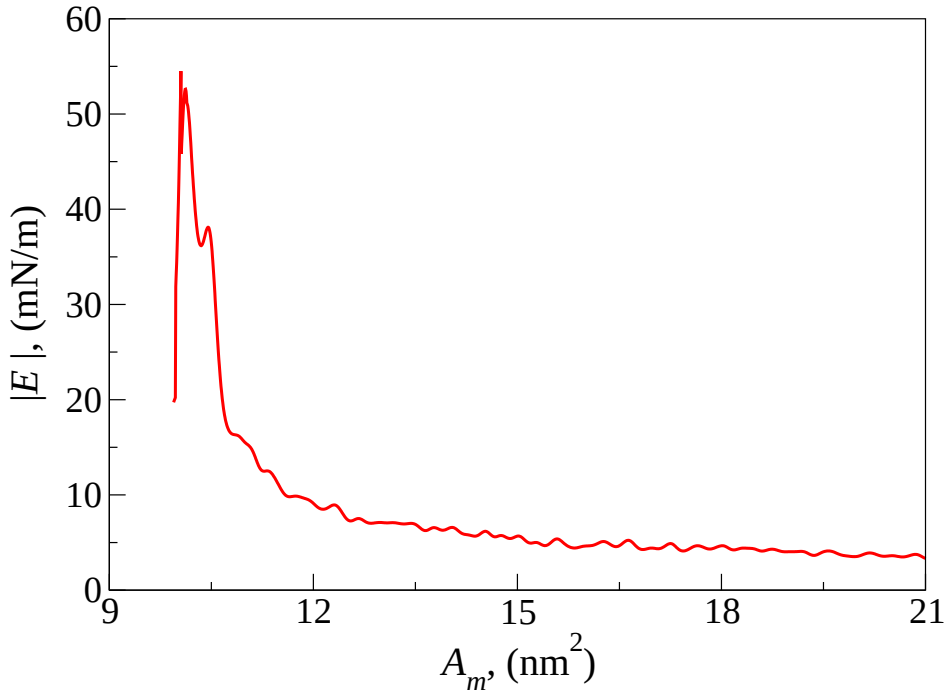

Figure 6.11: Compressional modulus $|E|$ as a function of area per molecule (A_m) for the monolayer of anthraquinone polymer.

for high values of A_m. On compression the monolayer smoothly transformed to an uniform L_1 phase. The Aqp monolayer collapses at an A_m of 9.2 nm^2 with a collapse pressure of about 8.6 mN/m.

LB films transferred onto the hydrophilic substrates of mica and gold coated silicon were studied using atomic force microscopy in the AC mode. The line profile on the topography images of the monolayer film on both the mica and gold coated silicon substrates yielded a height of about 1.0 nm. Also, the estimated height of the anthraquinone moiety (using ChemDraw) is about 1.0 nm. Hence, the height of the LB film obtained from the topography images suggest that the anthraquinone moieties in the film are in edge-on configuration on the substrate.

It is interesting to note that the discotic moieties in the LB films of Trp and Aqp molecules organizes in the edge-on configuration. The rigid aromatic rings in the polymers have de-localized Π electrons. These cores overlap due to the strong $\Pi - \Pi$ interaction, to form two-dimensional analog of columnar phase. Figure 6.12 shows the schematic diagram of organization of Trp and Aqp molecules with discotic moieties in edge-on configuration.

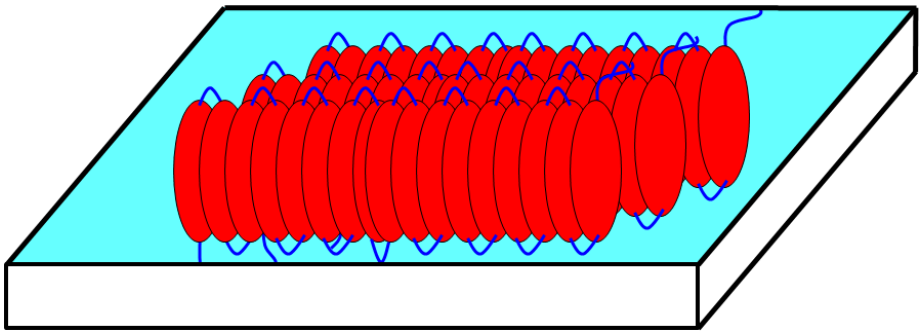

Figure 6.12: Schematic diagram showing the organization of Trp and Aqp molecules. Discotic moieties (red disks) i.e., triphenylene moiety in case of Trp monolayer and anthraquinone moiety in case of Aqp monolayer, are in the edge-one configuration.

Langmuir monolayers of monomeric triphenylene derivatives have been reported to exhibit both face-on and edge-on configuration depending on the area available for the molecules [14]. At high value of A_m, the molecules were in face-on configuration. On compression there was a phase transition from the face-on configuration to the edge-on configuration of the molecules. This was indicated by the initial gradual rise followed by a steep increase in surface pressure of the monolayer. But in the present studies we find that both the polymers exhibit edge-on configuration.

While the Langmuir monolayer of Trp molecules did not exhibit the coexistence phase, the Langmuir monolayer of Aqp molecules exhibited coexistence of gas and low density liquid phase at high area per molecule. The organization of the polymeric discotic liquid crystals are highly influenced by the strong $\Pi - \Pi$ interaction between the aromatic cores. In thin films of such molecules additional parameters like the interaction between the molecules and subphase/substrate and steric intermolecular interactions also affect the organization of the molecules.

6.5 Conclusions

We have studied the films of novel liquid crystalline polymers, Trp and Aqp, at air-water and air-solid interfaces. The Trp was made up of electron rich triphenylene moiety and the Aqp was made up of electron deficient anthraquinone moiety. We find that the Trp molecules

form a stable monolayer at air-water interface. At large A_m the monolayer exhibited gas phase. On compression the monolayer transformed into low density liquid phase at an A_m of 19 nm^2. The monolayer collapsed at an A_m of 15 nm^2 with a collapse pressure of about 6.3 mN/m. The LB films of Trp molecules were prepared by transferring the film onto the hydrophilic mica and hydrophobic silicon substrates and studied by AC mode AFM. AFM studies of the LB film on the hydrophilic mica substrate and the limiting area value obtained from the $\pi - A_m$ isotherm suggest that the triphenylene moieties in the Trp monolayer are in edge-on configuration. AFM studies of the LB film on the hydrophobic silicon substrate yielded a height corresponding to the bilayer film with the discotic moieties in the edge-on configuration.

Surface manometry and BAM studies showed that the material Aqp forms stable monolayer at air-water interface. At large A_m the monolayer exhibited coexistence of gas and low density liquid (L_1) phase. On compression, the monolayer slowly transformed to an uniform L_1 phase before collapsing with a collapse pressure of 8.6 mN/m. The LB film transferred onto the hydrophilic mica and gold coated silicon substrates showed domains of height 1.0 nm, which suggests that the anthraquinone moieties are in edge-on configuration.

The polymers of discotic liquid crystals can have potential applications in many devices because of their special electrical properties. Hence the electrical conductivity measurements of the LB films of these materials will be interesting. In the next chapter, we investigate the nanoscale electrical properties of these LB films on conducting substrates using current sensing AFM.

Bibliography

[1] O. K. C. Tsui, and T. P. Russell, *Polymer Thin Films*, World Scientific, (2008).

[2] A. V. Bune, V. M. Fridkin, S. Ducharme, L. M. Blinov, S. P. Palto, A. V. Sorokin, S. G. Yudin, and A. Zlatkin, *Nature* **391**, 874 (1998).

[3] A. L. Holt, J. P. Bearinger, C. L. Evans, and S. A. Carter, *Sensors and Actuators B: Chemical* , *doi* : 10.1016/ *j.snb*.209.09.055 (2009).

[4] J. P. Schmidtke, and R. H. Friend, *J. Chem. Phys.* **124**, 174704 (2006).

[5] S. Kumar, and S. Varshney, *Angew. Chem. Int. Edit.* **39**, 3140 (2000).

[6] W. Pisula, A. Menon, M. Stepputat, I. Lieberwirth, U. Kolb, A. Tracz, H. Sirringhaus, T. Pakula, and K. Mullen, *Adv. Mater.* **17**, 684 (2005).

[7] A. D. Dunbar, T. M. Richardson, A. J. McNaughton, J. Hutchinson, and C. A. Hunter *J. Phys. Chem. B* **110**, 16646 (2006).

[8] S. Palto, L. Blinov, A. Bune, E. Dubovik, V. Fridkin, N. Petukhova, K. Verkhovskaya, and S. Yudin, *Ferroelectr. Lett. Sect.* **19**, 65 (1995).

[9] G. Roberts, *Langmuir-Blodgett Films*, Plenum Press: New York and London, (1990).

[10] H. K. Bisoyi, and S. Kumar, *J. Mater. Chem.* **18**, 3032 (2008).

[11] Bharat Kumar, A. K. Prajapati, M. C. Varia, and K. A. Suresh, *Langmuir* **25**, 839 (2009).

[12] J. T. Davies, and E. K. Rideal, *Interfacial Phenomena*, Academic Press: NewYork, (1963).

[13] D. J. Dervichian, *J. Chem. Phys.* **7**, 932 (1939).

[14] A. Nayak, K. A. Suresh, S. K. Pal, and S. Kumar, *J. Phys. Chem. B* **111**, 11157 (2007).

Chapter 7

Nanoscale electrical conductivity of monolayer films of triphenylene and anthraquinone polymers at air-solid interface

7.1 Introduction

Studies on electron transport properties of the organic molecules are important to understand and build nanoscale electronic devices. Ultrathin film of organic molecules transferred onto a metal substrate forms an ideal system to study the nanoscale electrical properties. It has been reported that the monolayer film of these molecules between the metal electrodes exhibit nonlinear current(I)−voltage(V) characteristics. Such behavior of the metal-film-metal junctions can have potential applications [1, 2]. Since the last one decade, studies have been carried out in this direction, to understand the charge transport through thin films of various organic molecules. Depending on the molecule and its environment, the charge transport can occur by various mechanisms [3]. The electron conduction in a self-assembled alkanethiol monolayer device is reported to be dominated by the direct tunneling mechanism [4]. The dominance of direct tunneling in the alkyl chains was attributed to a large gap between

the highest occupied molecular orbital (HOMO) and lowest unoccupied molecular orbital (LUMO) of the alkyl chains. Molecules with relatively low HOMO-LUMO gap show a transition in the conduction mechanism from the direct tunneling at low bias voltages to the injection tunneling at high bias voltages [5]. This has been discussed in chapter 5 of this thesis. In addition to the electronic configuration of the molecules, the molecular conduction also depends on other factors like interaction of the molecules with metal substrate and its interaction with neighboring molecules, effect of polarization of molecules, etc [6].

Studies on the LB film of triphenylene monolayer have shown that the charge transfer occurs by injection (or Fowler-Nordheim) tunneling mechanism [7]. In chapter 5, we have reported our studies on the nanoscale electrical properties of the Langmuir-Blodgett (LB) film of oligomer containing both electron rich triphenylene moiety and electron deficient anthraquinone moiety. In this chapter, we report the nanoscale electrical conductivity studies carried out on the ultrathin films of novel liquid crystalline polymers of triphenylene and anthraquinone. The triphenylene polymer (Trp) is electron rich and the anthraquinone polymer (Aqp) is electron deficient. Monolayers of these materials were transferred by LB technique onto a gold coated silicon substrate. Current sensing atomic force microscope was employed to study the nanoscale electrical conductivity of the LB films. In contrast to the LB film of triphenylene monomer, the charge transfer through metal-Trp-metal and metal-Aqp-metal junctions show direct tunneling. From the analysis of the $I - V$ characteristics we obtained the barrier height of 2.48 eV for metal-Trp-metal junction and 1.95 eV for metal-Aqp-metal junction. We find the effective mass of electron for metal-Trp-metal and metal-Aqp-metal junctions to be about $0.07m_e$ and $0.09m_e$, respectively.

7.2 Experiment

Trp and Aqp were purified by column chromatography and the purity was better than 99% [8]. The monolayer films of both the materials, Trp and Aqp, were prepared on gold coated silicon substrates by LB technique. Gold coated silicon substrate being hydrophilic,

one layer of the film gets transferred onto the substrate in one dipping cycle (consisting of one down-stroke and one upstroke). The transfer of the film occurred during the upstroke. Here the dipping speed was 2 mm/min. The Trp monolayer was transferred at a surface pressure of 5 mN/m and the Aqp monolayer was transferred at a surface pressure of 7 mN/m.

The electrical measurements of the film transferred onto a gold coated silicon substrate were carried out using a current sensing atomic force microscope (CSAFM) (Molecular Imaging, Picoplus). Platinum coated silicon cantilevers (AppNano) having spring constant in the range of $0.02 - 0.8$ N/m and resonance frequency in the range $5 - 25$ kHz were used as conducting probes. The tip radius was about 30 nm. To get the current image, the film was scanned by keeping the tip at virtual ground and applying a sample bias voltage of 50 mV to the substrate. The film was scanned in the contact mode to acquire simultaneous topography image. A constant force of 4 nN between the cantilever tip and sample was maintained during the scan. This value of force was carefully chosen so that it was low enough not to damage the film but sufficient to maintain good contact between the tip and film. The film along with the gold coated silicon substrate and conducting tip can be considered as a metal-film-metal junction. To obtain the current(I)−voltage(V) characteristics of the junction, the conducting tip was kept at virtual ground and a voltage ramp was applied to the gold substrate. A preamplifier, with a sensitivity of 1 nA/V and operational range in between 1 pA and 10 nA was connected to the tip to measure the current. The RMS noise in our system was about 10 pA and a current value higher than this was detectable. The $I-V$ measurements were performed by placing the tip at the desired position on the film and carefully selecting the force between the tip and film. After every $I - V$ measurement we scanned the same region of the film to check for any damage.

7.3 Results

The ultraviolet(UV)/visible spectroscopy studies of the Trp and Aqp were carried out. We have estimated the energy gap E_g between the HOMO and LUMO of Trp and Aqp molecules

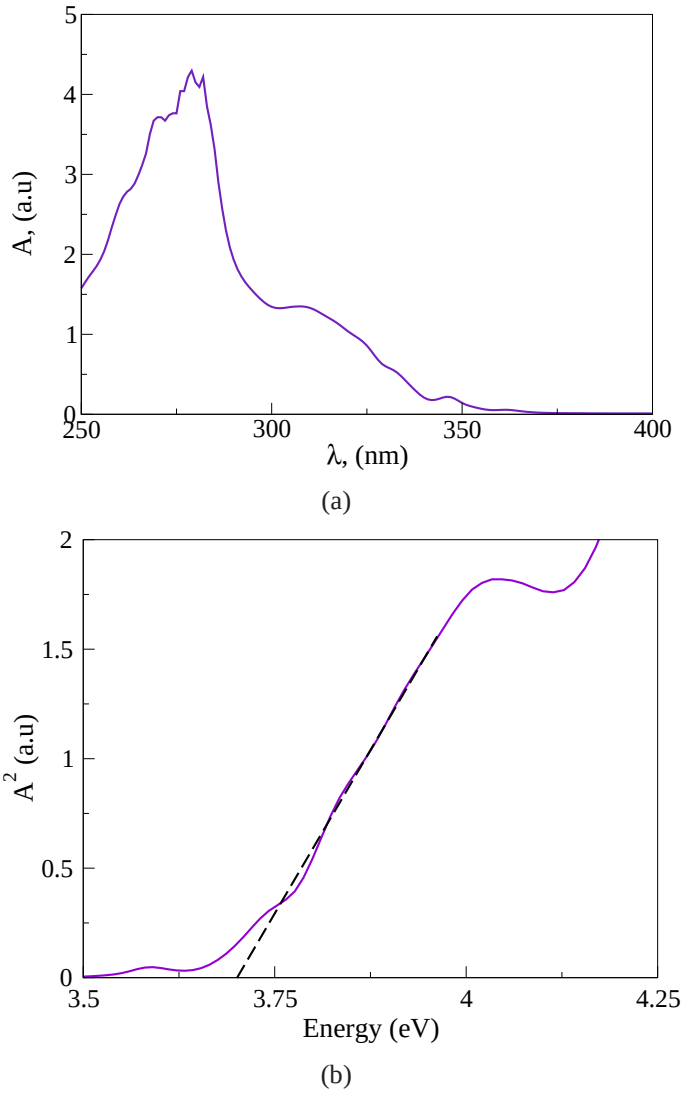

Figure 7.1: (a) Shows the UV-visible spectra for Trp molecules. (b) Shows absorbance squared versus the photon energy $h\nu$. The curve is extrapolated to zero absorption to estimate the E_g value for Trp. The HOMO-LUMO gap (E_g) for Trp was about 3.7 eV.

from the optical absorption curve. The E_g value can be estimated from the absorbance (A) using the relation $Ah\nu = (h\nu - E_g)^{1/2}$, where $h\nu$ is the photon energy [9]. Figures 7.1 and 7.2 show the variation of A^2 as a function of $h\nu$ for Trp and Aqp, respectively. The values of direct optical band gap were estimated by extrapolating the linear region of the curve to zero A^2 value. The E_g values of 3.7 eV and 2.7 eV were obtained for Trp and Aqp molecules, respectively.

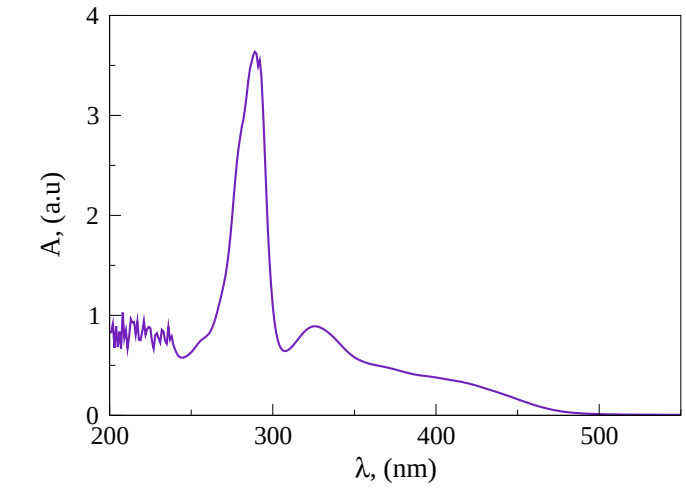

(a)

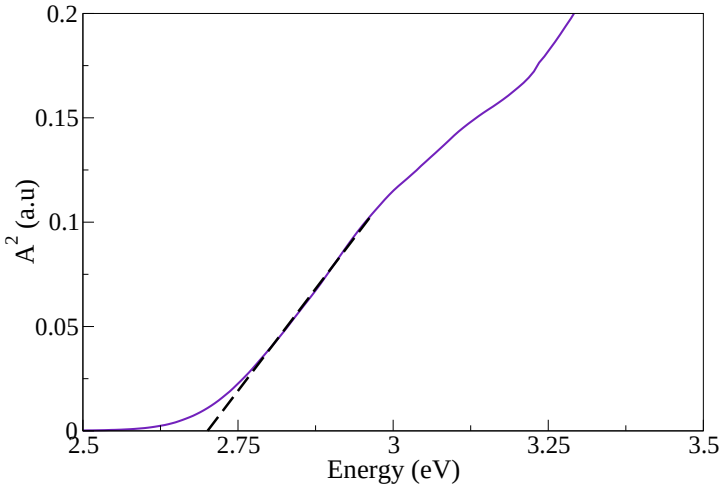

(b)

Figure 7.2: (a) Shows the UV-visible spectra for Aqp molecules. (b) Shows absorbance squared versus the photon energy $h\nu$. The curve is extrapolated to zero absorption to estimate the E_g value for Aqp. The HOMO-LUMO gap (E_g) for Aqp was about 2.7 eV.

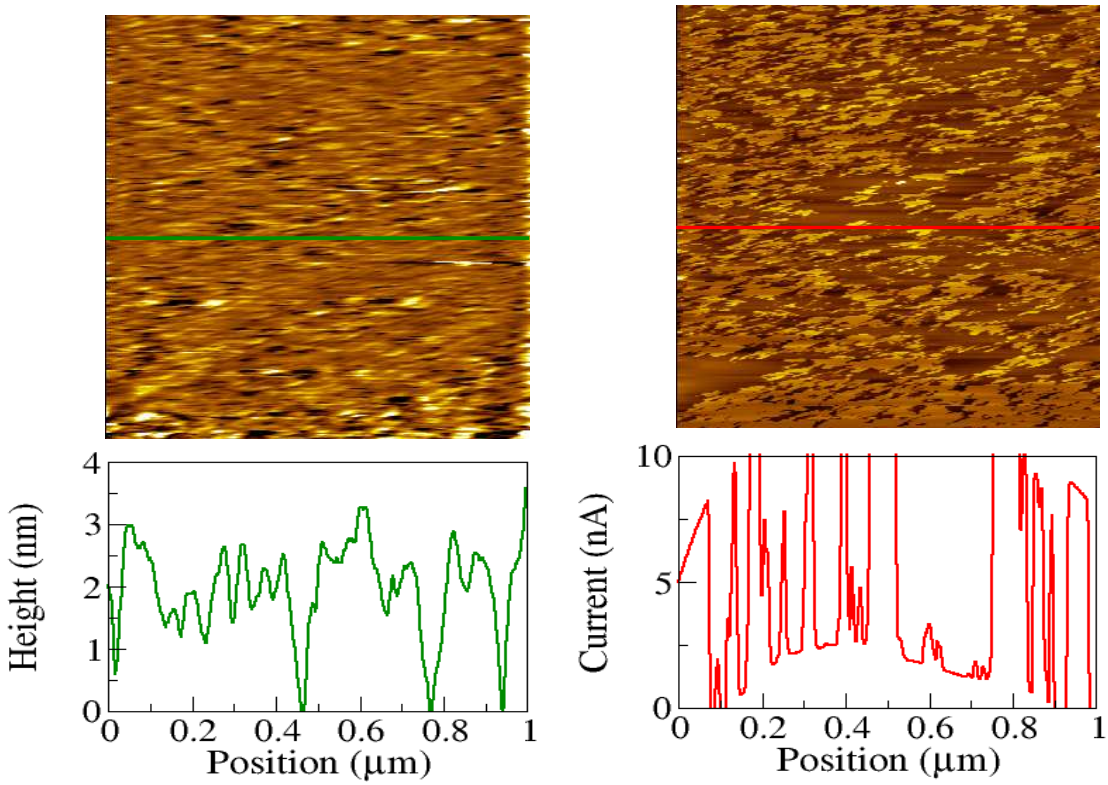

(a) Topography image (b) Current image

Figure 7.3: Current sensing AFM images of the Trp monolayer LB film on a gold coated silicon substrate transferred at a surface pressure of 5 mN/m. (a) Shows the topography image. The line profile yields a height of 1.9 nm. (b) Shows the current image. The line profile yields an average current value of 2 nA in the regions covered with the film.

7.3.1 Triphenylene polymer (Trp) film

LB film of Trp molecules transferred onto a gold coated silicon substrate was studied using CSAFM. Figure 7.3 shows the topography and current images of the Trp monolayer. The line profile on the topography image yields an average height of 1.9 nm. The line profile on the current image shows variation in the current values. In the region where the substrate is covered with the film, the measurements yielded an average I value of 2 nA. In the regions where there is no film the current shoots up to a high value (> 10 nA).

The $I-V$ measurements of the monolayer film was carried out by holding the conducting tip in contact with the film. The force applied by the tip on the monolayer was controlled by a feed back loop and it was low enough not to damage the film but sufficient to maintain good electrical contact with the film. A voltage ramp of -0.2 V to $+0.2$ V was applied with a

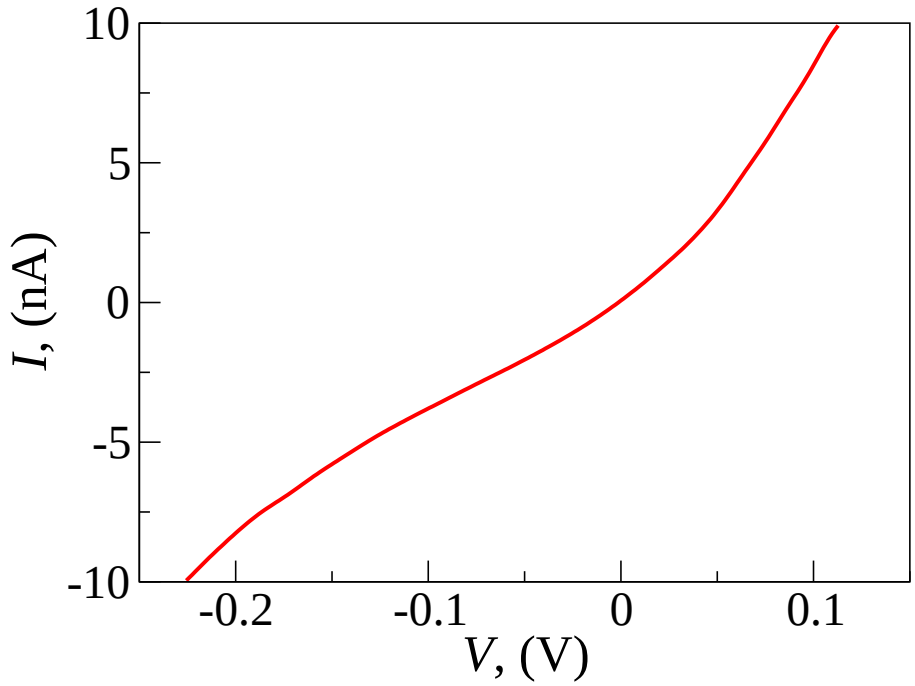

Figure 7.4: Current(I)−voltage(V) characteristics of the monolayer of triphenylene polymer on a gold coated silicon substrate.

scan rate of 1 Hz to the substrate and the tip was kept at the virtual ground. Figure 7.4 shows the typical $I - V$ characteristics of Trp monolayer. A small current offset of about 50 pA was observed at zero voltage.

7.3.2 Anthraquinone polymer (Aqp) film

The LB film of Aqp was prepared by transferring the monolayer film onto a gold coated silicon substrate. The film was transferred at a surface pressure of 7 mN/m. Contact-mode CSAFM was employed to study the LB film as explained in the section 7.2. Figure 7.5 shows the topography and current images of the Aqp monolayer. The line profile on the topography image yields a height of the film to be 1 nm. The line profile on the current image yields an average current value of 2.5 nA in the regions covered by the film. The region not covered with the film showed high current value (> 10 nA).

The $I - V$ measurements of the Aqp LB monolayer film were carried out in the same manner as in the case of Trp film. Figure 7.6 shows the typical $I - V$ characteristics of Aqp

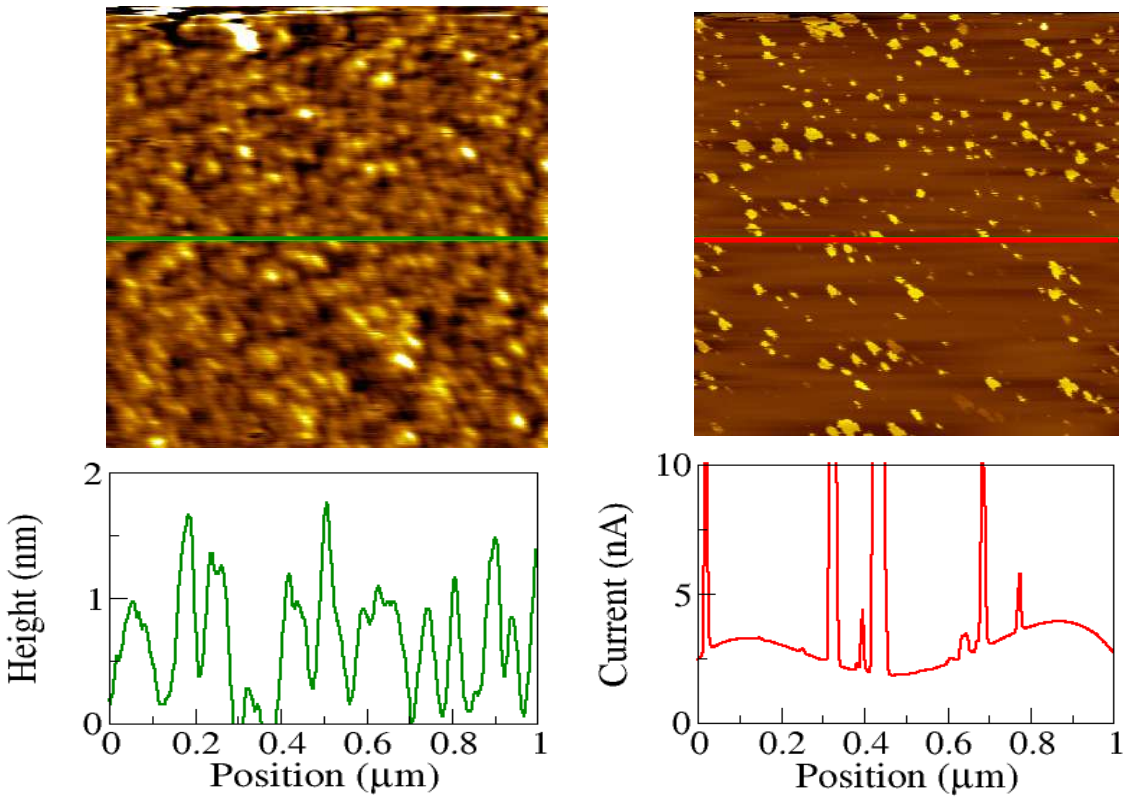

(a) Topography image

(b) Current image

Figure 7.5: Current sensing AFM images of the Aqp monolayer LB film on a gold coated silicon substrate transferred at a surface pressure of 7 mN/m. (a) Shows the topography image. The line profile yields an average height of 1.0 nm. (b) Shows the current image. The line profile yields an average current value of 2.5 nA in the regions covered with the film.

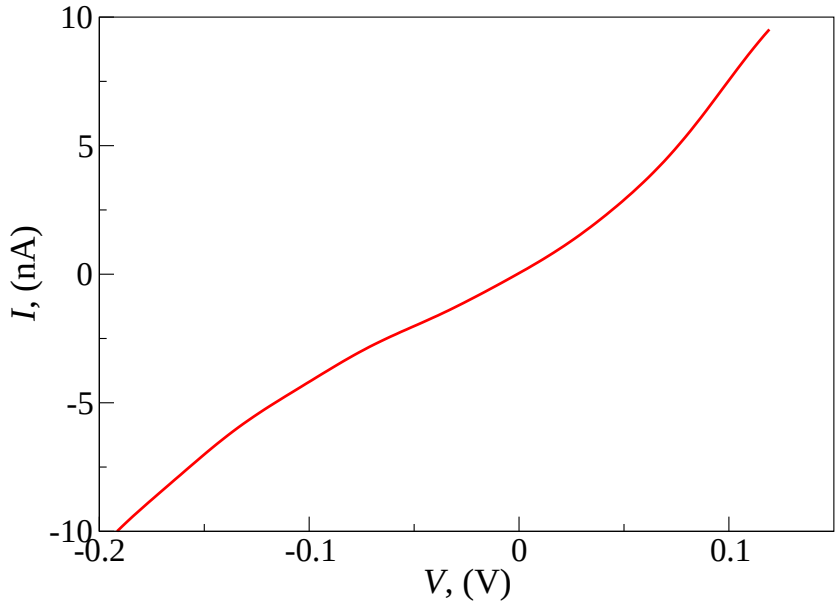

Figure 7.6: Current(I)−voltage(V) characteristics of the monolayer of anthraquinone polymer on a gold coated silicon substrate.

monolayer. At low applied bias voltages the current value increased gradually and then it increased rapidly at high applied bias voltages. A small current offset of about 50 pA was observed at zero voltage.

7.4 Discussion

Current sensing atomic force microscope (CSAFM) studies of the Trp LB film on a hydrophilic gold coated silicon substrate was carried out to get topography and current images. The line profile on the topography image yielded a height of about 1.9 nm. Since the diameter of the triphenylene moieties (estimated using ChemDraw) is also about 1.9 nm, we suggest that the discotic moieties of Trp molecules are in edge-on configuration. The limiting area obtained from the $\pi - A_m$ isotherm also indicates edge-on configuration. Similar organization of the molecules was found in the LB film on a mica substrate.

The line profile on the current image shows variation in the current values. The I value of about 2 nA was found in the region where the substrate is covered by the film. In regions without the film, the current shoots up to a high value since the conducting tip is in contact

with the gold substrate.

In the previous chapter, we have shown that the anthraquinone moieties of the Aqp molecules in the LB film transferred onto a gold coated silicon substrate assemble in the edge-on configuration. The height of the film was about 1.0 nm. The topography image obtained from the contact mode CSAFM also yielded a height of 1.0 nm corresponding to the edge-on configuration of the anthraquinone moieties on the substrate.

The line profile on the current image obtained from the CSAFM studies of the Aqp film showed varying current values. In regions without the film, the current shoots up to a high value since the conducting tip is in contact with the conducting substrate. In the regions where the substrate is covered by the film, the line profile yielded an average current value of 2.5 nA.

7.4.1 Nanoscale electrical measurements

The nanoscale electrical conductivity of the metal-Trp-metal junction was studied from the $I-V$ measurements. The $I-V$ characteristics showed non-linear behavior. A current offset of about 50 pA was found at zero voltage. This offset is usually attributed to the charging current of the system capacitance [10]. The shape of the $I-V$ curve indicated that the charge transfer through the metal-Trp-metal junction is through a potential barrier [11]. Hence the Trp monolayer introduces a potential barrier for the charge transfer between the gold coated silicon substrate and the platinum coated cantilever tip, leading to a non-linear $I-V$ characteristics. Electron transport between two electrodes separated by a potential barrier can occur by two mechanisms: Schottky emission and electron tunneling. In Schottky emission, the electrons in the electrode have enough thermal energy to surmount the potential barrier and flow in the conduction band. Here, the electronic current is characterized by decrease in the $\mathrm{d}I/\mathrm{d}V$ as the value of V increases. Figure 7.7 shows the variation of $\mathrm{d}I/\mathrm{d}V$ as a function of applied bias voltage for the metal-film-metal junction. We find that, $\mathrm{d}I/\mathrm{d}V$ increases with increase in applied bias voltage. This suggests that the charge transfer is not due to the Schottky emission. Hence we infer that the current through the junction is due to the electron

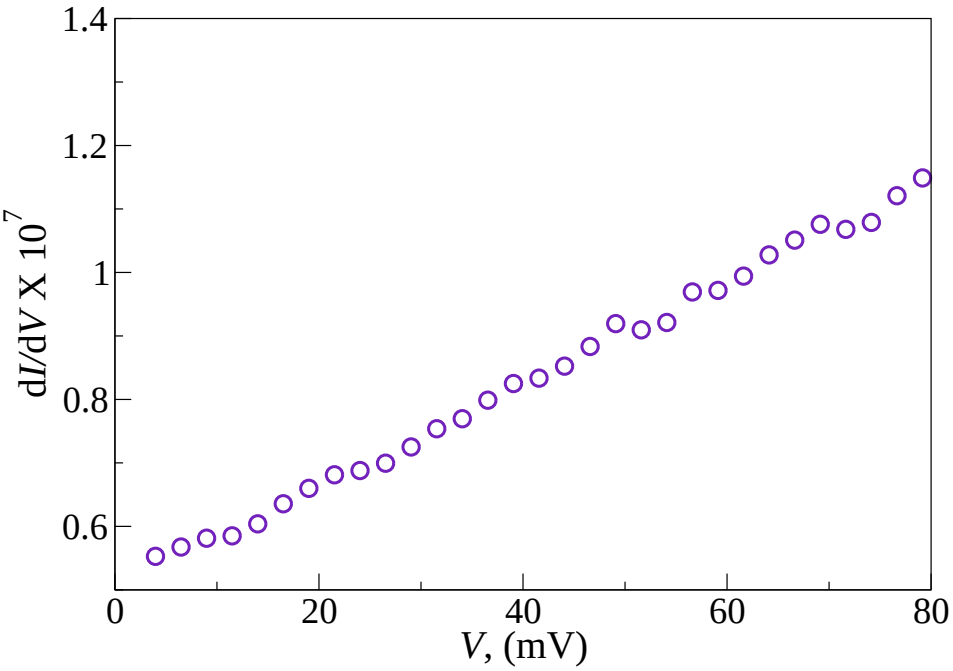

Figure 7.7: Variation of $\mathrm{d}I/\mathrm{d}V$ as a function of V for the metal-Trp-metal junction. The increase in the value of $\mathrm{d}I/\mathrm{d}V$ as a function of V suggests that the electron transfer is not dominated by Schottky emission.

tunneling.

A generalized formula for the electric tunnel effect between two electrodes separated by an arbitrary potential barrier was suggested by Simmons [12]. The formula holds good for the metal-insulator-metal junction where, either the highest occupied molecular orbital (HOMO) level or the lowest unoccupied molecular orbital (LUMO) level of the insulator is near to the Fermi level of the electrode (E_f). The $I-V$ relation for the tunneling through the potential barrier of arbitrary shape is given by the equation,

$$I = \frac{eA}{2\pi h\bar{d}^2}\left[\bar{\phi}exp\left(-\frac{4\pi\bar{d}\sqrt{2m^*\bar{\phi}}}{h}\right) - (\bar{\phi}+eV)exp\left(-\frac{4\pi\bar{d}\sqrt{2m^*(\bar{\phi}+eV)}}{h}\right)\right] \qquad (7.1)$$

where, e is the charge of electron, A is the effective electrical contact area between tip and film, $\bar{\phi}$ is the mean barrier height, $\bar{d}$ is the mean barrier width, m^* is the effective mass of electron and h is the Planck's constant. For very low applied bias voltage, the shape of the potential barrier can be considered to be rectangular. Here, $\bar{\phi} \approx \phi_\circ$ and $\bar{d} \approx d$, where $\phi_\circ$ is

the height of the rectangular barrier and d is the distance between the electrodes. With these approximations, equation 7.1 reduces to,

$$I = \frac{A\sqrt{2m^*\phi_\circ}}{d}\left(\frac{e}{h}\right)^2 V exp\left(-\frac{4\pi d\sqrt{2m^*\phi_\circ}}{h}\right). \tag{7.2}$$

At intermediate bias voltages ($V < \phi_\circ/e$), the potential barrier can be considered to be of trapezoidal shape. In this regime, $\overline{\phi} \approx \phi_\circ - eV/2$ and $\overline{d} \approx d$. For the $\pi-$conjugated molecules it has been reported that the charge transport mechanism at intermediate bias voltages ($V < \phi_\circ/e$) is by direct tunneling [5]. Direct tunneling refers to the tunneling of the charge from one electrode to the other, without hopping or diffusing into the insulating medium. In this regime, the variation of $\ln(I/V^2)$ as a function of $1/V$ exhibit logarithmic growth.

At very high voltages, equation 7.1 reduces to the injection or Fowler-Nordheim tunneling equation [13]. It has been suggested that the potential barrier in this regime can be assumed to be of triangular shape. In this charge transport mechanism, the charge from an electrode is injected into the insulator by tunneling and then it is transported to the other electrode. This mechanism of charge transfer is characterized by a linear relationship between $\ln(I/V^2)$ and $1/V$. If the potential barrier between the electrodes is appropriate then transition from direct tunneling to injection tunneling can be obtained by varying the applied bias voltage [5]. Detailed discussion of the charge transport through the metal-insulator-metal junction is given in chapter 5.

We have analyzed the $I - V$ characteristics of the Trp film by fitting equation 7.1 to the data points. The potential barrier ($\phi_\circ$) and the effective mass of electron (m^*) are varied to obtain a good fit. Figure 7.8 shows the variation of I as a function of positive bias voltage (V) for the metal-Trp-metal junction. The solid line in the figure shows the fit to the experimental data. The fit parameters yielded the $\phi_\circ$ and m^* values of 2.48 eV and 0.079 m_e, respectively. Since the applied bias voltages were less than the barrier height, we conclude that the charge transport is through direct tunneling. This was further confirmed by plotting $\ln(I/V^2)$ as a

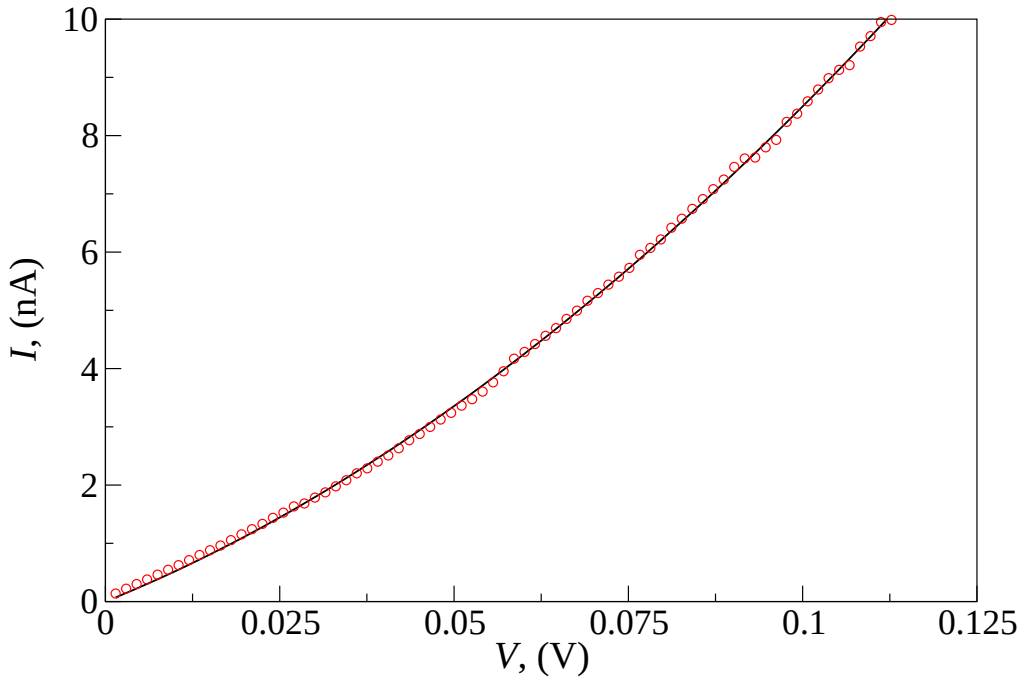

Figure 7.8: Variation of current (I) as a function of bias voltage (V) for the monolayer of triphenylene polymer. The data represented by the open circles is fitted to the equation 7.1 (solid line). The barrier height of the film obtained from the fit parameter was 2.48 eV.

function of V. We find that the $\ln(I/V^2)$ logarithmically increases with increase in $1/V$, which is characteristic of direct tunneling. Because of the experimental limitations, we could not study the $I-V$ characteristics of the film for the current values greater than 10 nA.

The charge transport properties of the monolayer film of Aqp on the gold coated silicon substrate were similarly studied. Figure 7.6 shows the typical $I-V$ characteristics of the Aqp film between two metal electrodes. The $I-V$ curve was non-linear. Similar to the Trp film, the shape of $I-V$ curve indicated a potential barrier for the charge transfer between the electrodes. Hence the charge transport in the metal-Aqp-metal junction can occur either by Schottky emission or by electron tunneling. The $\mathrm{d}I/\mathrm{d}V$ value increases with increase in the applied bias voltage, suggesting that the charge transfer is not due to the Schottky emission. Figure 7.9 shows the variation of $\mathrm{d}I/\mathrm{d}V$ as a function of applied bias voltage. The potential barrier and the effective mass of electron were calculated by fitting equation 7.1 to the $I-V$ data. Figure 7.10 shows the variation of I as a function of V for the metal-Aqp-metal junction. The solid line is the fit to the data. The fit parameters yielded the $\phi_\circ$ and m^* values

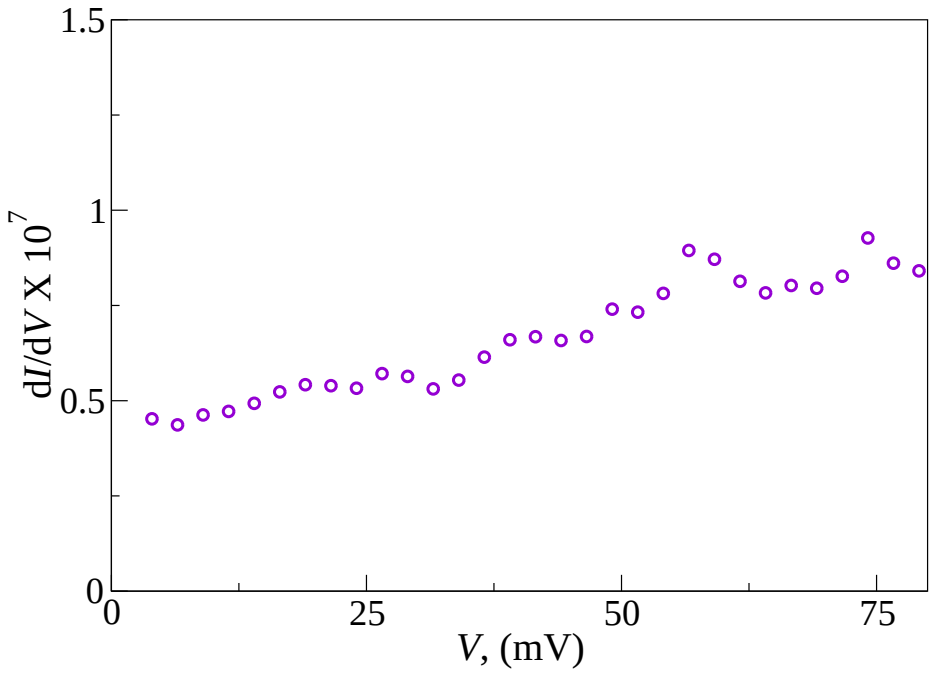

Figure 7.9: Variation of dI/dV as a function of bias voltage (V) for the monolayer of anthraquinone polymer. The increase in the value of dI/dV as a function of V suggests that the electron transfer is not dominated by Schottky emission.

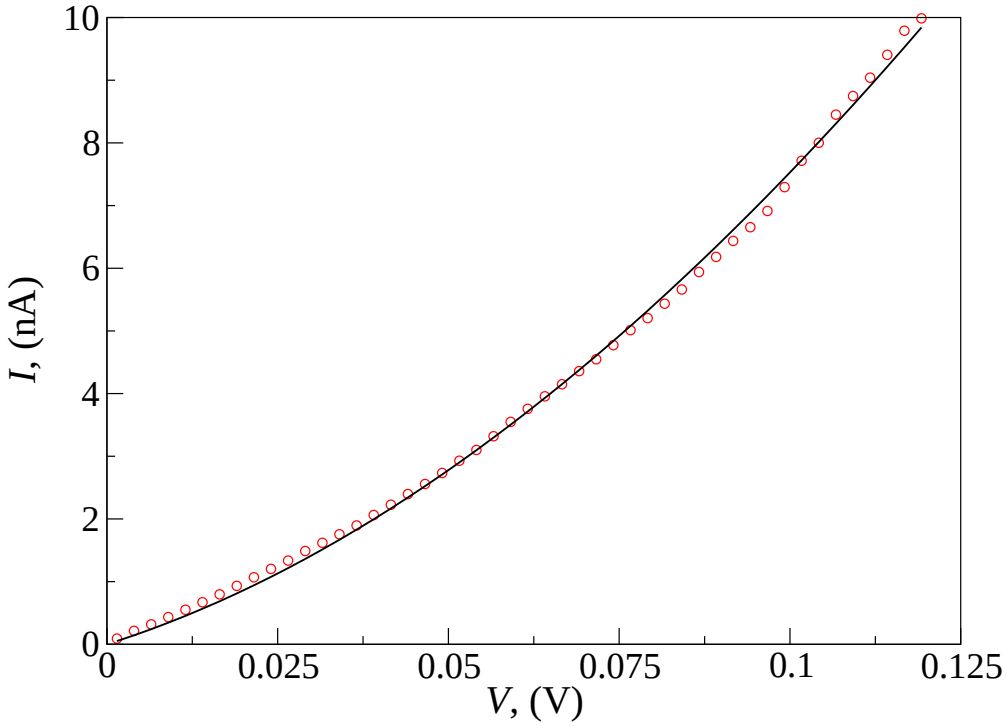

Figure 7.10: Variation of current (I) as a function of bias voltage (V) for the monolayer of anthraquinone polymer. The data represented by the open circles is fitted to equation 7.1 (solid line). The barrier height of the film obtained from the fit parameter was 1.95 eV.

of 1.95 eV and 0.09 m_e, respectively. Since the barrier height of the film was greater than the applied bias voltage, we infer that the electron transfer through the film is by direct tunneling mechanism. This was further confirmed by the logarithmic increase in the $\ln(I/V^2)$ as $1/V$ is increased.

The value of $\phi_\circ$ for the case of π-conjugated thiol molecules between two metal electrodes was in the range of 0.5 – 1.0 eV [5]. Studies on the purple membrane have reported the barrier height to be in between 1.5 – 2.2 eV [14]. The height of the potential barrier and its profile introduced by a thin film of insulator between two metal electrodes depend on many factors like the electronic configuration of the molecules in the film, its interaction with the neighboring molecules and coupling of the molecules with the electrode itself. Beebe *et al.* [5] have reported a linear relationship between the barrier height (obtained from the transition voltage) and the energy gap between the Fermi level of metal (E_f) and HOMO level of insulating molecule (E_{HOMO}). They have also reported that the barrier height was less than the $E_f - E_{HOMO}$ value. The lowering of the barrier can be attributed to the assumptions made during its calculation like the assumption of simple barrier shapes and neglecting the effect of image potential.

7.5 Conclusions

The electrical properties of LB films of two novel liquid crystalline polymers, one made up of electron rich triphenylene moiety and the other made up of electron deficient anthraquinone moiety, were studied. The monolayer film of the polymer formed at air-water interface was transferred onto gold coated silicon substrate by LB technique. Electrical measurements were carried out using CSAFM. The gold coated silicon substrate-film-conducting tip of CSAFM which forms a metal-film-metal junction showed non-linear $I - V$ characteristics. Our analysis of the $I - V$ data showed that the electron transfer is through direct tunneling mechanism. The barrier height ($\phi_\circ$) for metal-Trp-metal and metal-Aqp-metal junctions was about 2.48 eV and 1.95 eV, respectively. We also find that the effective mass of electron for

metal-Trp-metal junction was less than that of metal-Aqp-metal junction.

Bibliography

[1] K. Moth-Poulsen, and T. Bjornholm, *Nature Nanotech.* **4**, 1 (2009).

[2] A. Aviram, and M. A. Ratner, *Chem. Phys. Lett.* **29**, 277 (1974).

[3] Y. Selzer, L. Cai, M. A. Cabassi, Y. Yao, J. M. Tour, T. S. Mayer, and D. L. Allara, *Nano Lett.* **5**, 61 (2005).

[4] W. Wang, T. Lee, and M. A. Reed, *Phys. Rev. B* **68**, 035416 (2003).

[5] J. M. Beebe, B. Kim, J. W. Gadzuk, C. D. Frisbie, and J. G. Kushmerick, *Phys. Rev. Lett.* **97**, 026801 (2006).

[6] M. Galperin, M. A. Ratner, A. Nitzan, and A. Troisi, *Science* **319**, 1056 (2008).

[7] A. Nayak, and K. A. Suresh, *Phys. Rev. E* **78**, 021606 (2008).

[8] H. K. Bisoyi, and S. Kumar, *J. Mater. Chem.* **18** 3032 (2008).

[9] I. Seguy, P. Jolinat, P. Destruel, J. Farenc, R. Mamy, H. Bock, J. Ip, and P. Nguyen, *J. Appl. Phys.* **89**, 5442 (2001).

[10] P. Mishra, P. Karmakar, and D. Ghose, *Nucl. Instrum. Methods Phys. Res. B* **243**, 16 (2006).

[11] D. Xu, G. D. Watt, J. N. Harb, and R. C. Davis, *Nano Lett.* **5**, 571 (2005).

[12] J. G. Simmons, *J. Appl. Phys.* **34**, 1793 (1963).

[13] M. Lenzlinger and E. H. Snow, *J. Appl. Phys.* **40**, 278 (1969).

[14] I. Casuso, L. Fumagalli, J. Samitier, E. Padros, L. Reggiani, V. Akimov, and G. Gomila, *Phys. Rev. E* **76**, 041919 (2007).

Summary

This thesis describes our studies on the Langmuir monolayers and Langmuir-Blodgett (LB) films of azobenzene molecule and derivatives of some discotic molecules of novel structures. The monolayer film of H-shaped azobenzene dimer (12D1H) at air-water interface and its wetting properties on the hydrophilic and hydrophobic substrates were studied. We find that the bilayer film of 12D1H transferred onto a hydrophobic substrate dewetts by spinodal dewetting to form droplets. We have also described the kinetics of *trans* to *cis* isomerization of 12D1H on illumination of ultraviolet light. Our studies on the Langmuir monolayer of a dimer of triphenylene moiety (tp-dimer) showed that the collapse pressure of the monolayer increases with increase in strain rate and they are related by a power law. The nanoscale electrical conductivity studies of star shaped oligomer (AQD6), triphenylene polymer (Trp) and anthraquinone polymer (Aqp) films were studied using current sensing atomic force microscope (CSAFM). The LB film of AQD6 molecule, which has both electron deficient anthraquinone moiety and electron rich triphenylene moiety, showed a transition from direct tunneling to injection tunneling mechanism as the applied bias voltage is increased. Our studies on the Langmuir monolayers and LB films of Trp and Aqp molecules showed that the discotic moieties were in edge-on configuration. Though the Trp molecule is electron rich and Aqp molecule is electron deficient, our CSAFM studies on the metal-Trp-metal and metal-Aqp-metal junctions indicated that the charge transfer was through direct tunneling.